An Accurate On-Machine Surfaces Measurement Using FEA Method

Muerus Rodrigues

A Thesis
in
The Department
of
Mechanical, Industrial & Aerospace Engineering (MIAE)

Presented in Partial Fulfillment of the Requirements
for the Degree of
Master of Applied Science (Mechanical Engineering)
at Concordia University
Montreal, Quebec, Canada

August 2021

CONCORDIA UNIVERSITY

School of Graduate Studies

This is to certify that the thesis prepared

By: **Muerus Rodrigues**

Entitled: **An accurate on-machine surfaces measurement using FEA method**

and submitted in partial fulfillment of the requirements for the degree of

Master of Applied Science (Mechanical Engineering)

complies with the regulations of the University and meets the accepted standards with respect to originality and quality.

Signed by the final Examining Committee:

Dr. Youmin Zhang	Chair
Dr. Youmin Zhang	Examiner
Dr. Leon Wang	Examiner
Dr. Zezhong Chevy Chen	Thesis Supervisor

Approved by ______________________________

Dr. Sivakumar Narayanswamy, Graduate Program Director

____

Dr. Mourad Debbabi, Dean, Gina Cody School of Engineering and Computer Science

Date ______________________________

Abstract

An accurate on-machine surfaces measurement using FEA method

Muerus Rodrigues

Kinematic touch trigger probes are widely used in medium to large-scale industries for part setup and quality assurance due to their economical advantage over noncontact probes. These tools significantly reduce the lead times during part setup and inspection processes. However, the sensing distance error caused by the electro-mechanical switching mechanism substantially influences the measurement results and thus needs to be calibrated before utilizing the probe. In this thesis, an accurate on machine surface measurement process based on finite element method is implemented to predict the sensing distance of a kinematic touch trigger probe based on Renishaw's OMP40-2 probe, FEA simulation model is verified using the existing mathematical model and experimental data. A novel mathematical model is developed taking into consideration the sliding effects of the probe tip on the part surface. Three cases of surface measurement are considered, which are, vertical surface, inclined surface, and a curved surface, followed by FEA methods in finding the sensing distance and the spindle travel to compensate for the surface measurement error. A newly developed surface measurement model is verified using the experimental results. Two case studies are presented, inclined surface measurement results with sliding effects are compared with that of an existing model and two curved surfaces (Ellipsoidal and Convex) cases are studied. Finally, inclined surface and ellipsoidal surface results are compared to study the effects of surface curvature on the sensing distance.

Acknowledgements

I would like to greatly thank the following people, without whom I would not have been able to complete this research work, and without whom I would not have made it through my master's degree.

My supervisor Dr. Zezhong Chevy Chen, for his dedicated support and priceless guidance throughout my research work. Dr. Chen's deep understanding in this area of research and patience helped me conduct this valuable research. Thank you for giving me this golden opportunity to work under you.

I would like to express my special gratitude to Stephen Fang for acting as my mentor and his constant help and support throughout steered me through this research. I would also like to thank my fellow colleagues in my research lab for their support and ideas during this research.

Finally, my deep and sincere gratitude to my mom, dad and sister for their continuous support and love. Their selfless encouragement helped me keep going and complete my thesis. Thank you so much for being there for me always.

Table of Contents

List of Figures

List of Tables

Nomenclature

f	Spindle feed rate
L	Length of the stylus stem
$\mathbf{N}_0, \mathbf{N}_1, \mathbf{N}_k$	Surface normal at k^{th} subprocess
$\mathbf{C}_0, \mathbf{C}_1, \mathbf{C}_2, \mathbf{C}_k$	Probe tip center at k^{th} subprocess
$\mathbf{F}_{p0}, \mathbf{F}_{p1}, \mathbf{F}_{pk}$	Probing force at k^{th} subprocess
$\mathbf{S}_0, \mathbf{S}_1, \mathbf{S}_2, \mathbf{S}_k$	Spindle location at k^{th} subprocess
d_f	Displacement along initial feed direction
d_{s1}, d_{s2}, d_{sk}	Displacement of stylus perpendicular to the probe axis at k^{th} subprocess
d_{sd}	Sensing distance
$\boldsymbol{\beta}$	Polar angle
$\boldsymbol{\alpha}$	Azimuthal angle
$\mathbf{T}_0, \mathbf{T}_1, \mathbf{T}_k$	Contact point between probe tip and part surface at k^{th} subprocess
$\mathbf{V}_0, \mathbf{V}_1, \mathbf{V}_{k-1}, \mathbf{V}_k$	Unit vector along the direction of normal vector projected on the plane perpendicular to the probe axis at k^{th} subprocess
$\mathbf{N}_{kx}, \mathbf{N}_{ky}, \mathbf{N}_{kz}$	Components of k^{th} normal vector
$\boldsymbol{S}_1$	Part surface
$\boldsymbol{S}_2$	Probe sphere surface
$\mathbf{N}_{0(in)}$	Unit inward normal to the part surface
$\mathbf{P}_k$	Point lying vertically below $\mathbf{S}_k$ at a distance L

$\mathbf{T}_{kx}, \mathbf{T}_{ky}, \mathbf{T}_{kz}$	Components of contact point **T** at k^{th} subprocess
$\mathbf{C}_{kx}, \mathbf{C}_{ky}, \mathbf{C}_{kz}$	Components of probe tip center **C** at k^{th} subprocess
$\mathbf{S}_{kx}, \mathbf{S}_{ky}, \mathbf{S}_{kz}$	Components of spindle location **S** at k^{th} subprocess
$\boldsymbol{r}$	Radius of spherical probe tip
$\boldsymbol{L}$	Line passing through point $\mathbf{P}_k$ and parallel to $\mathbf{V}_{k-1}$
$\mathbf{d}$	Distance between points on two surfaces (part and probe sphere surface)
$\boldsymbol{n}_{1k(\text{in})}$	Inward normal vector to part surface at k^{th} subprocess
$\mathbf{N}_{1k(\text{in})}$	Unit inward normal vector to part surface at k^{th} subprocess
$\boldsymbol{n}_{1k(\text{out})}$	Outward normal vector to part surface at k^{th} subprocess
$\mathbf{N}_{1k(\text{out})}$	Unit outward normal vector to part surface at k^{th} subprocess
$\mathbf{v}_k$	Component of normal vector $\boldsymbol{n}_{1k(\text{out})}$ in the plane perpendicular to probe axis
$\boldsymbol{n}_{2k(\text{in})}$	Inward normal vector to probe surface at k^{th} subprocess
$\mathbf{S}_{\mathbf{t}}$	Position of spindle at the trigger instance
$\mathbf{T}\mathrm{p}$	Measured point on the surface

Chapter 1: Introduction

1.1 Background

According to ISO 9000:2015 section 3.6.2, quality is defined as “the degree to which a set of inherent characteristics of an object fulfills requirements”. In the manufacturing world, the goal of the Quality Control (QC) is to not only prevent irregularities in the part, but also to make sure that the manufactured parts are within the design tolerances and will function well [1].

Co-ordinate Measuring Machine (CMM) was first introduced at the international machine tool exhibition in Paris in 1959 by Ferranti, a British company. This traditional CMM uses a mechanical touch trigger probe to touch discrete points on the part. Although they provide exceptionally accurate and precise measurements of the part geometry, it requires comprehensive setup time including specially designed programs and training of the operators. Also, the data capture rate is slow, taking up to 10 minutes per 100 discrete points. Having the disadvantage of slow data collection and processing these traditional CMMs worked well for data sampling and not suitable for inspecting high to medium volume parts. Inspection on CMMs also increased the total manufacturing cost and lead time due to moving of the part to be inspected to and from machine tool and co-ordinate measuring machine [2].

On Machine Measurement (OMM) was introduced wherein the cutting tool on the machine spindle was replaced by the probes for inspection process, thereby eliminating the time required for moving the part and corresponding second fixture problem. OMM may improve the quality of the part or product, increase customer satisfaction and profitability if it is adequately accurate and cost of operating OMM is less than that of the defective parts. Today, with technological improvements, high quality machine tools can perform and retain precise tolerances to provide accurate measurements with good measurement practices.

The probe is an integral part of the measurement process both on co-ordinate measuring machines and machine tools. A probe is effectively a switch that is designed in a manner to trigger when it comes in contact with the workpiece surface by providing an accurate and repeatable co-ordinate data. Obtaining this measurement data and processing it throughout the entire manufacturing process can ensure parts produced are within desired tolerance limits. Probes are broadly classified into two main categories: contact and non-contact probes. Contact probes are categorized as hard probes, touch trigger probes and analog scanning probes. While, non-contact probes consists of laser and vision probes [3].

1.2 Kinematic Touch Trigger Probe

The touch trigger probe was first invented by Renishaw in the year 1973, making them the industry standard for offline part inspection. With the invention of the touch trigger probe, several machine tool users favoured using the probes since the mid 1970s. At those times, probes were used only on Co-ordinate Measuring Machines (CMMs). Today, however, touch trigger kinematic probes have become an integral part of machine tools for maximizing efficiency, quality, capability, and accuracy. These probes are used in a variety of industries including Aerospace, Automotive, Construction, Mining, Research, Machinery and more [4]. Figure 1.1 shows a physical OMP40-2 touch trigger probe designed and manufactured by Renishaw.

Figure 1.1: Renishaw OMP40-2 Touch Trigger Probe

The kinematic touch trigger probe design is based on the kinematic arrangement wherein, the tripod is spring loaded, and its each tripod rod sits on two supporting balls establishing six contact pairs thereby ensuring the stylus is held in unique position providing excellent repeatability. The mechanism is such that the probe stylus will deflect upon contacting with the workpiece while the preloaded spring ensures that the mechanism re-seats in its initial position whenever contact between probe and workpiece is removed [5]. Figure 1.2 shows the interior of typical touch trigger kinematic probes.

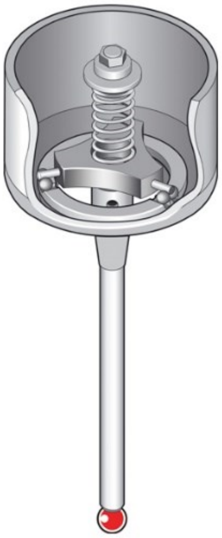

Figure 1.2: Interior of typical kinematic touch trigger probes

The contacting elements, i.e., tripod rods and the supporting balls are usually made of a very hard and highly conductive material such as tungsten carbide, to ensure that the elastic deformation occurring in the contact patch of the tripod rods and supporting balls is very small. The six contact pairs form an electrical circuit through which the current flows, any change in resistance through this circuit is then measured by inbuilt electronics and the probe triggers [5]. Figure 1.3 shows a Renishaw OMP40-2 touch trigger probe probing a workpiece on a CNC machine tool.

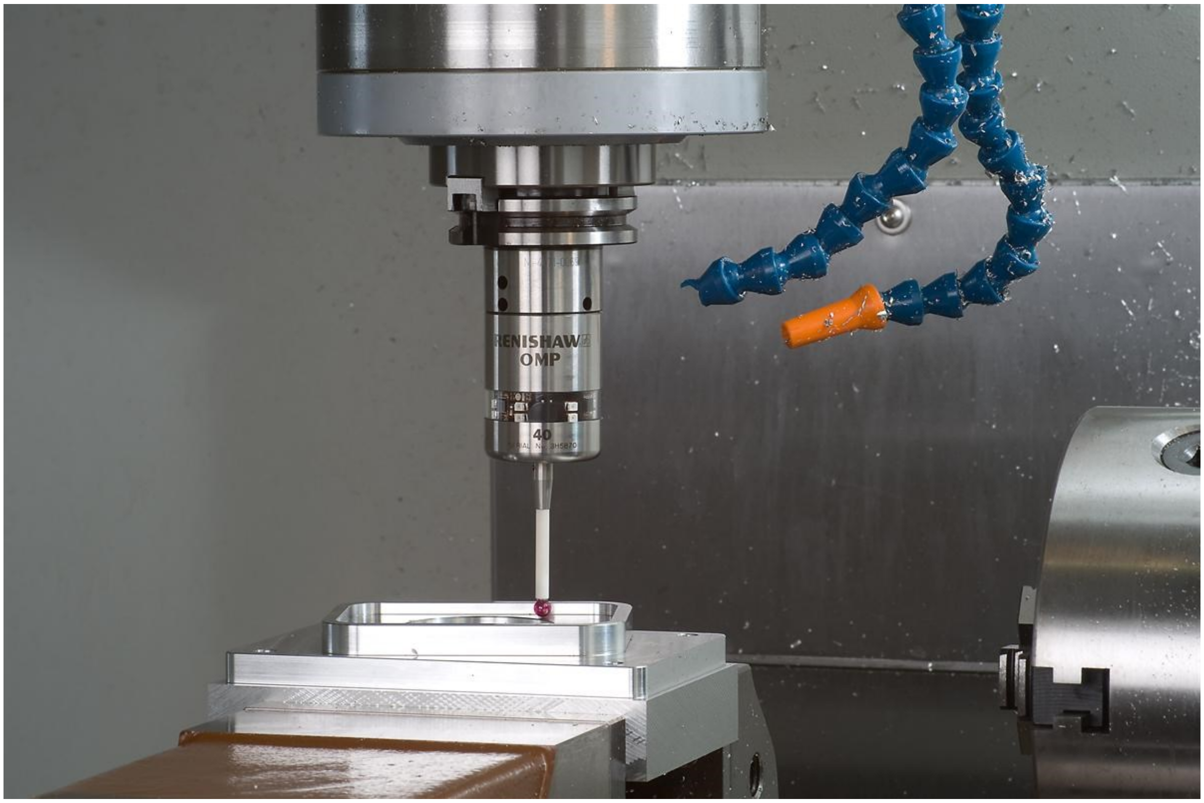

Figure 1.3: Renishaw OMP40-2 probing a workpiece on CNC machine tool [6]

1.3 Literature Review

Out of all the errors associated with the touch trigger probes such as sensing distance, hysteresis, and repeatability errors, sensing distance error is a highly repeatable and deterministic form of error. It is mainly caused because of bending deflection of the stylus stem and is influenced by the force deviations along different probe approach directions. This can lead to measurement error caused by the variations in the stylus stem bending prior to triggering of the probe. Thus, this error needs to be addressed and compensated for. Shen *et al.* [7] developed a sensing distance model for a vertically oriented touch trigger probe by first deriving trigger force model based on the principles of mechanics. To apply this mathematical model to predict the sensing distance, the threshold contact force parameter was obtained from the experimental probe calibration data and used to verify the model along different probe approach directions. The sensing distance along the probe approach direction is modelled as a bending deflection of a stylus stem by treating the stylus stem as a cantilever beam and the trigger force as a force acting at the free end of the cantilever beam. However, in a physical touch trigger kinematic probe, the tripod rods are not fixed, but they can separate under the applied probing force and thus it cannot be considered as a cantilever beam. The authors have not taken into consideration this mechanism for calculating the sensing distance.

Johnson *et al.* [8] described the factors, which influence the errors of touch trigger probes and split them into groups. The first group of factors consists of motion-related factors, like approach speed, probe acceleration, and approach distance. This is the group connected with the probe tip's impact with the measured surface. The second group consists of probing configuration factors. The probe errors depend on the stylus mass and rigidity, preload spring force, the probe orientation, and the probe stylus length. The third group of factors is the mode of operation. The next type of factor relates to the operating environment. Ambient variation such as thermal drift, a large variation in air temperature as well as ambient vibration may also result in touch trigger probe errors. The last group of factors, which may also affect the probe performance, are measured object factors. The probe pretravel may depend on form, surface texture and material young’s modulus of the measured object.

One of the factors influencing repeatability and sensing distance variation of a touch trigger probe is the preloaded spring force. This spring force can be adjusted using a screw mechanism.

Wozniak *et al.* [9] developed a new setup for testing the triggering force of the probes and was validated experimentally. They concluded by evaluation the quality of the results showed that the shape is in accordance with the theoretical models of the touch probes. Bohan *et al.* [10] studied the mechanics of the probe triggering mechanism under the practical conditions by using high resolution displacement sensor, high speed data acquisition and specially designed detection circuit. They validated experimental results with the theoretical results. They concluded that the triggering mechanism pivots around different axis as the probe approach direction changes and the sensing distance varied periodically following a 120 degrees cycle around 360 degrees.

Qian *et al.* analyzed major factors influencing the touch trigger probe measurements. They developed probe measurement error model using artificial neural network and presented the error compensation model with the help of 3 layered back propagation artificial neural network. They concluded that their model makes the on-machine measurement more precise, automatic, and efficient [11]. Achelker *et al.* [12] inspected 2D and 3D features of a component using a OMP60 touch trigger probe developed and manufactured by Renishaw on a CNC machine tool. The component was probed using a CNC part program and the obtained discrete points were transferred into the CAD system for generating curves and thereby surfaces which were then compared with the original CAD Model of the component being probed. The 2D features were validated using digital height gauge and 3D features using Coordinate Measuring Machine and compared with the obtained tool probe results. They concluded that the probing system can be employed in the machine tool replacing the costly CMMs for inspection.

Predicting the sensing distance and trigger force and compensating for this error has always been a major challenge faced by researchers in this area. However, the previous research involved oversimplification of the probe model. In addition, they failed to study the effects of sliding of the probe tip on the sensing distance.

1.4 Sensing Distance of Kinematic Touch Trigger Probe

Sensing distance of the kinematic touch trigger probe is an amount by which the stylus stem deflects from its initial position where it contacts the part surface until it reaches the position where the probe mechanism triggers. According to the mechanics of material, the sensing distance is always perpendicular to the probe axis irrespective of the probe approach directions [13]. On the contrary, the probe pretravel is the distance travelled by the spindle accompanied by the probe from its initial position to the point where it triggers.

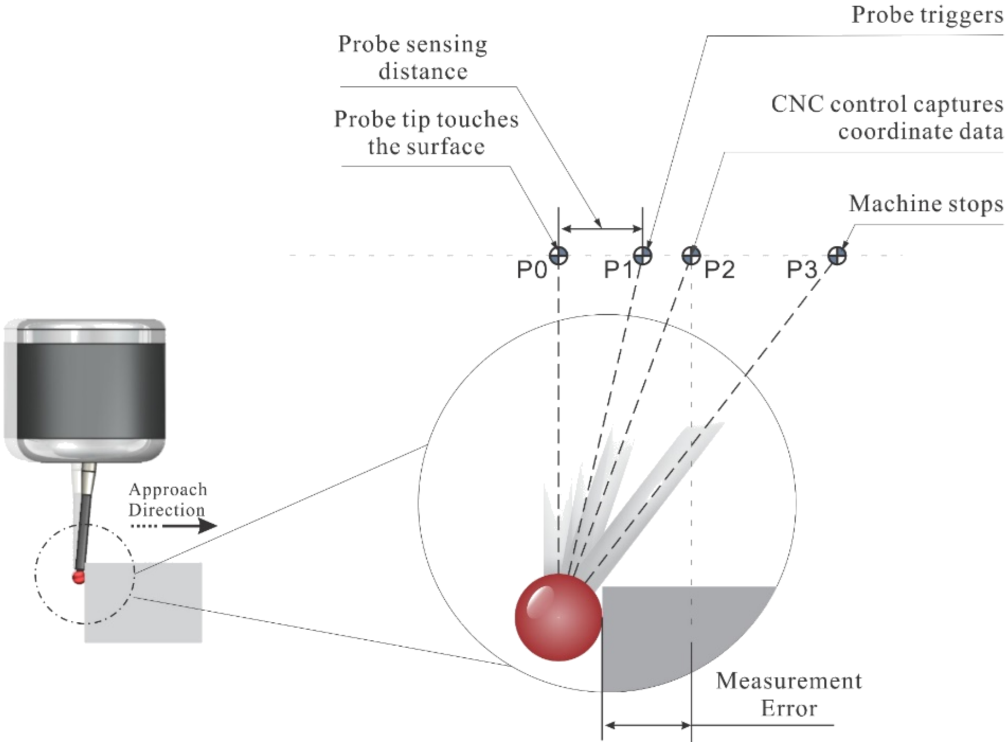

Figure 1.4: Sensing distance of a kinematic touch trigger probe [4]

1.5 Working Principle of a Kinematic Touch Trigger Probe

The probe initially in the free space with all its kinematics in contact is slowly moved towards the workpiece surface. When the stylus just touches the workpiece surface, there is no probing force acting on the stylus tip, the contact pairs remain in contact thereby not triggering the probe. The probe further drives into the contact with the part due to the machine's motion, probing force between the stylus and the part starts to build up. The contact moment generated by this probing force is balanced by the reactive moment due to the preloaded spring loaded on top of the tripod. Eventually, the increase in the probing force increases the contact moment which overcomes the reactive moment by the preloaded spring thereby lifting the tripod rod off the contact, breaking the electrical circuit in the probe, and thereby triggering the probe. This triggering signal then latches the machine position at that trigger instance and commands the machine tool to slow down and pull back from the surface. Once the probe backs off from the part surface, i.e., when it is in free space the tripod reseats into its repeatable rest position with the help of the preloaded spring. Based on the kinematic principle, the stages of trigger signal generation are shown below in Figure 1.5.

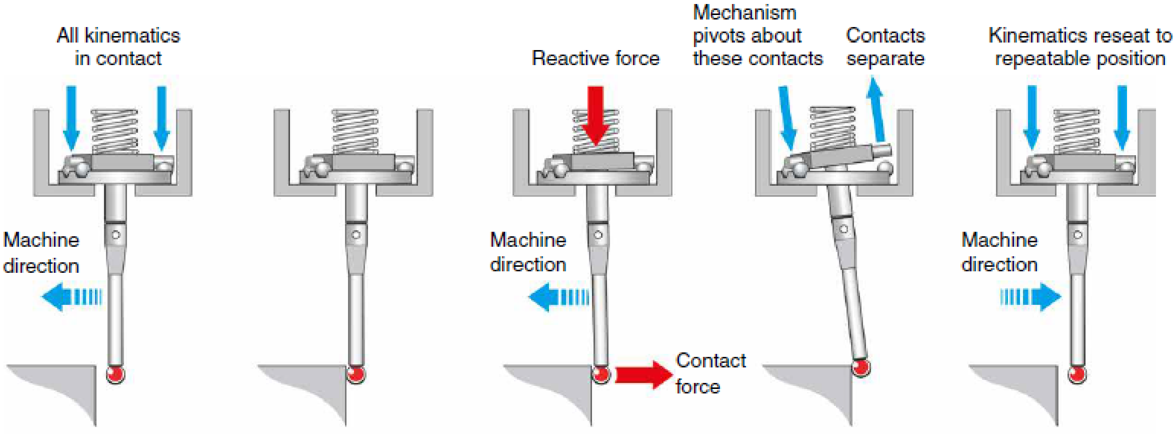

Figure 1.5: Working of a kinematic touch trigger probe [4]

1.6 Parameters Affecting Sensing Distance

The sensing distance of a touch trigger probe equipped on either a CMM or a Machine tool is affected by various probing parameters. Miguel *et al.* [14] performed tests on a kinematic touch trigger probe to measure its accuracy. Butler [15] investigated the nature of the probe errors, the parameters influencing the probe performance and proposed a method for probe performance verification. They both presented factors that affect the probe performance and its repeatability. Some of the parameters affecting the sensing distance of a probe are described below:

1. Preloaded Spring Force: Sensing distance error is higher when the preloaded spring force set is higher. This is because a high force is required to bend the stylus stem to trigger the probe. If the preloaded spring force is smaller, the probe will trigger early as compared to the previous case since a lower force will be required to bend the stylus stem. In a later case, the probe is prone to vibrations as the spring force is less to hold the tripod tight [14], [15].

2. Probe approach directions: The probe approach direction is given in terms of Azimuthal and Polar angles. Due to the three lobed structure of the kinematic touch trigger probes, the probing force required to trigger the probe along various directions varies significantly, and thus, these approach angles affect the sensing distance. According to Miguel *et al.* [14], the maximum sensing distance error is observed at the azimuthal angles 120 degrees apart. The sensing distance along these probe approach directions is obtained by measuring the standard reference sphere and then calibrated before the actual probing process.

3. Geometry of Stylus Stem: The length and the cross-sectional area of the stylus stem affect the sensing distance. The higher length of the stem with a smaller cross-sectional area will cause the stem to bend more prior to triggering as it has lower stiffness. While the stem

with a smaller length and the larger cross-sectional area will tend to deflect less due to high stiffness.

Other parameters include, contact conditions between probe and workpiece, material properties of the stylus stem, contact workpiece material, speed of approach and form of stylus tip [15].

1.7 Problem Definition

Sensing distance is a major contributor to the measurement uncertainty in kinematic touch trigger probes. Although this error is dependent on various probe and measurement parameters, for a particular set of parameters it is a form of systematic error and thus can be compensated for. Due to the economical benefits of the touch trigger probes, they are widely used in most industries, and thus it is vital to increase the measurement accuracy of the kinematic probes.

The general research problem is to predict the sensing distance of a kinematic touch trigger probe based on Renishaw's OMP40 -2 touch probe while taking into consideration the sliding effects without simplifying the probe model.

1.8 Research Objectives

In order to increase the measurement accuracy, it is essential to accurately predict the sensing distance which can then be compensated. The objectives of this research are concluded with the following aspects:

To compute the sensing distance of the kinematic touch trigger probes using the finite element method in order to avoid the simplification of the probe model,

To compute the sensing distance of the kinematic probes taking into consideration the sliding effects of the probe tip on the part surface, To compensate for the probe travel during the surface measurement process in case of inclined and curved surfaces.

1.9 Thesis Outline

This thesis consists of 5 chapters. Chapter 1 introduces the kinematic touch trigger probe, literature review and drawbacks of previous research, problem definition, and the research objectives. Chapter 2 is regarding the finite element modeling of a kinematic touch trigger probe. The FEA simulation model is verified using experimental results and an existing mathematical model. The new surface measurement algorithm and the implementation of the FEA model in predicting the sensing distance are presented in Chapter 3. Chapter 4 discusses the sensing distance results for vertical and inclined surfaces. In addition, two case studies are presented considering the sliding effects. A sensitivity study is then carried out by varying probe parameters. Finally, Chapter 5 concludes the work on this research and proposes potential future work in this area.

Chapter 2: Finite Element Modeling of Touch Trigger Probe

2.1 Introduction to Finite Element Method

Finite Element Method (FEM) converts a continuous body consisting of infinite degrees of freedom into a discrete domain containing finite number of degrees of freedom. The first step in FEM includes identifying the Partial Differential Equations (PDEs) that are associated with the given physical problem. These PDEs which are a strong form are then converted into integral forms known as weak form [16]. The next step is to discretize the weak form which can be solved numerically by converting integration into summation. The main goal of discretization is to convert the weak form into matrix equations which can then be solved using matrix algebra [16]. Figure 2.1 shows a flowchart for a generalized FEA model of a kinematic touch trigger probe.

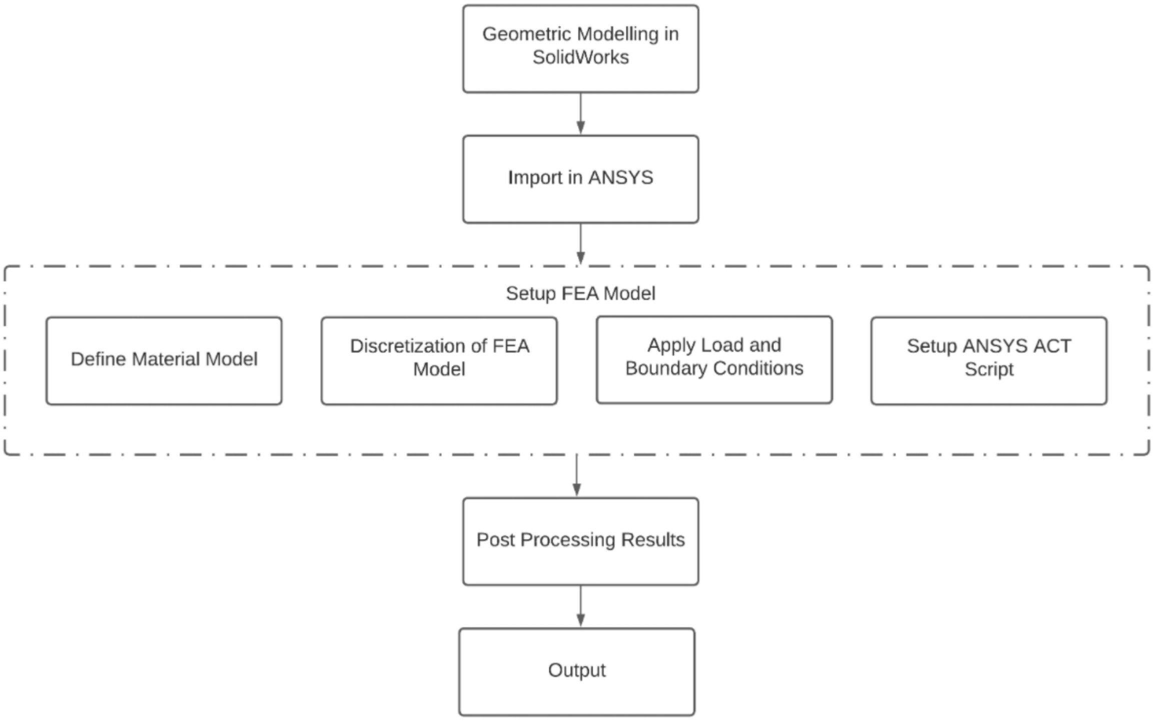

Figure 2.1: Flowchart of a probe FEA simulation model

2.2 Geometric Modeling

The geometric model of the kinematic touch trigger probe for this research is based on the OMP40-2 probe manufactured by Renishaw. The dimensions of the interior of the probe were obtained by dismantling OMP40 - 2 probe as shown in Figure 2.2. Probe geometry was modeled and assembled in Solidworks and imported in Ansys Mechanical Workbench.

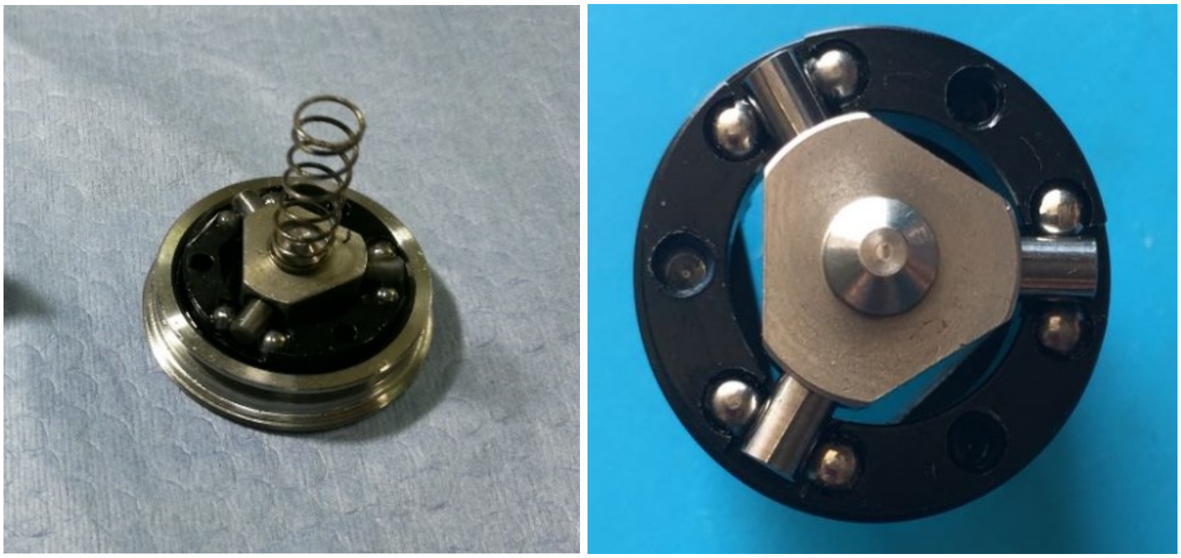

Figure 2.2: Interior of a OMP40 – 2 probe

The tripod having three rods is placed on six supporting balls consisting of three pairs fixed on a basement plate and 120 degrees apart to align with tripod rods. Tripod is held in its position by the preloaded spring placed on top as shown in Figure 2.2. A standard 50 mm length and 4.5 mm diameter stylus with a 6 mm ruby ball is fixed to the tripod as shown in Figure 2.3. The complete assembled probe model based on Renishaw’s OMP40-2 touch trigger probe is shown in Figure 2.3.

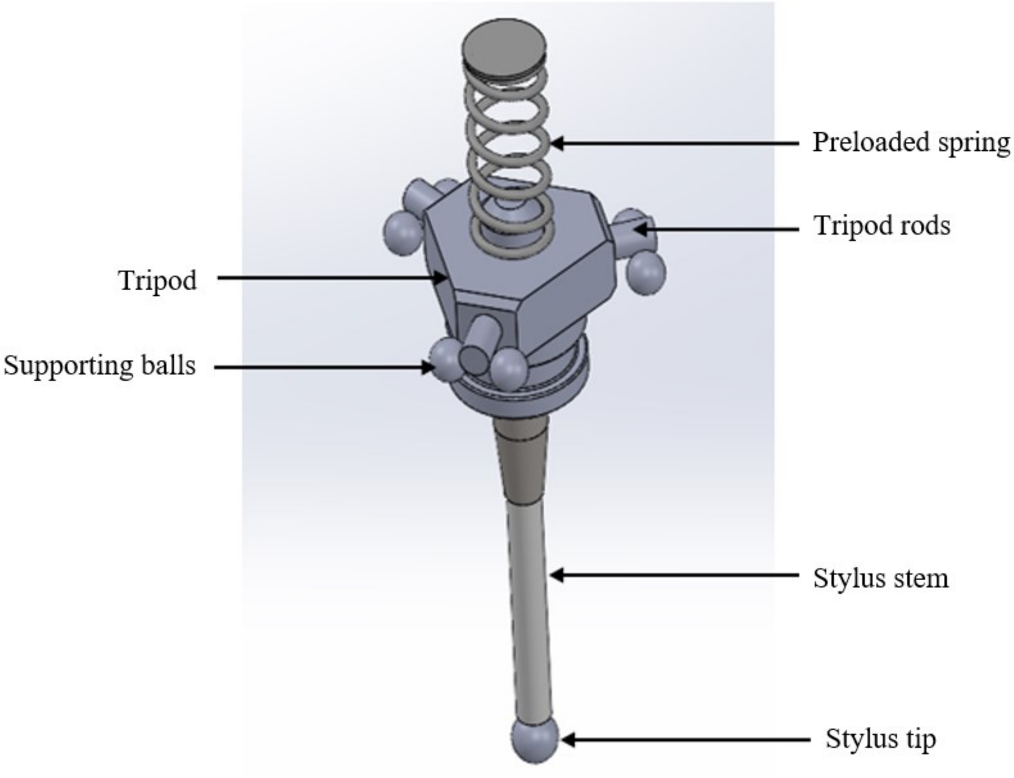

Figure 2.3: Probe CAD model based on Renishaw OMP40-2

2.3 Material Modeling

The contacting elements of the probe i.e., the tripod rod and the supporting balls are made of tungsten carbide having low electrical resistivity which forms an electric circuit and ensures that the elastic deformation occurring between these six contact pairs is very small [5]. The standard probe stylus with stainless steel head and ceramics body was modeled as shown in Figure 2.4. Also, for this research, the stylus tip made of ruby is considered. Since there are no large deformations and the material does not undergo plastic deformation, our probe model is linear in terms of material model. Hence, the linear elastic material model is considered.

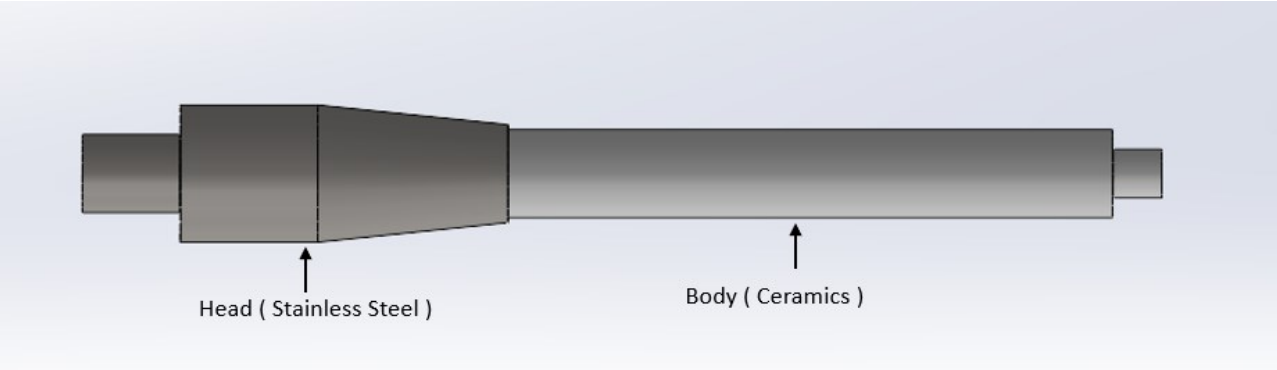

Figure 2.4: 50 mm probe stylus stem

Table 2.1: Material of probe components

Part	Material
Tripod	Tungsten carbide
Supporting balls	Tungsten carbide
Preloaded spring	ASTM steel material
Stylus stem	Stainless steel, Ceramics
Stylus tip	Ruby

2.4 Contact Modeling

The touch trigger probe model consists of six contact pairs (tripod rod and supporting balls) which are held together in their place with the help of preloaded spring force. The friction between these six contact pairs is neglected and thus modeled as frictionless contacts. In this type of contact, the bodies in contact can separate depending on the load applied and is therefore considered as a nonlinear type of contact as the area of contact changes due to separation. Since the coefficient of friction is zero, there is a relative free sliding between two bodies [17]. In physical phenomenon, these six contacts are smooth and are in contact with each other initially due to preloaded spring force. Since Finite Element Method involves discretization of the continuous body, this may lead to a small initial gap in the contact region which may produce inaccurate results. Another reason is due to slop in the CAD geometry while importing in ANSYS, which may result in a small gap. Thus, proper care must be taken so that this initial gap is closed prior to solving the finite element model. To solve the latter problem, an adjustment is done in the contact region by setting the interface treatment to adjust to touch [18]. The resolution for the earlier problem, i.e., in the case of discretization is discussed in Section 2.5.

Frictionless contact problem in finite element method is considered as boundary non-linearity. Contact boundary and contact stress or pressure are unknown prior to the solution even though the contact candidates are specified. The solver can identify gaps in the contact if any, only after discretizing the model. The finite element algorithm searches for any nodes on the contact side that penetrates the target side and applies the contact force on those nodes to satisfy the contact condition as shown in Figure 2.5 (a) and (b).

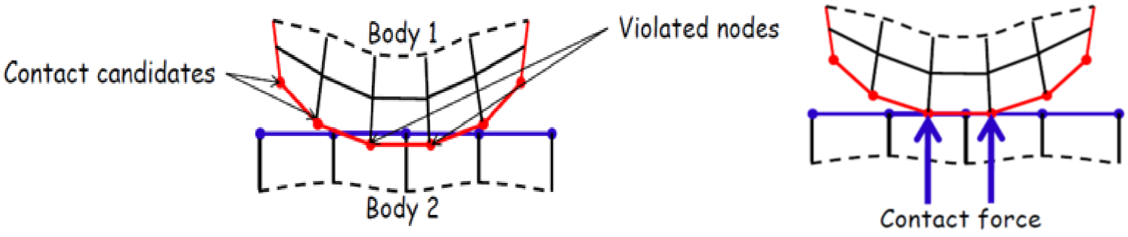

(a) (b)

Figure 2.5: (a) Node violation in contact generation, (b) Contact force applied at violating nodes [19]

According to ANSYS contact technology guide [19], the two surfaces in contact are designated as contact and target surfaces, respectively. Care must be taken to properly define these surfaces, or it may lead to inaccurate results. The following guidelines must be followed to designate the contact surfaces, (1) Contact surface elements cannot penetrate the target surface, however, the target surface elements can penetrate the contact surface as shown in Figure 2.6, (2) Out of two surfaces, the one with fine mesh should be the contact surface and the one with coarse mesh should be the target surface, (3) A stiffer body should be the target surface, while a softer body should be the contact surface. Keeping this in mind, since both of the bodies are made of the same material i.e., Tungsten carbide, and they also have contact match condition applied i.e., both surfaces have the same mesh density, either surface can be designated as contact or target surface. Proper establishment of the contact can be verified only after discretizing the model.

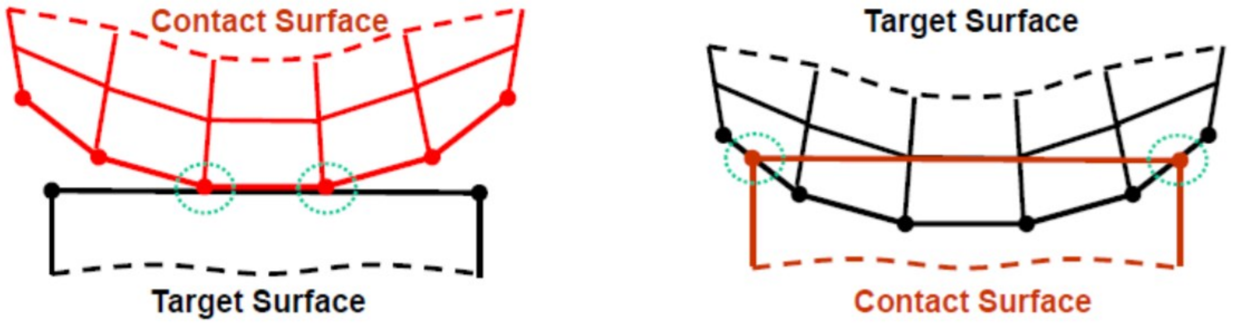

Figure 2.6: Effect of contact and target side on contact formulation [19]

2.5 Discretization

The automatic global meshing in ANSYS is not very beneficial usually when the model consists of contacts and in case of highly curved surfaces such as cylinders (tripod rod) and spheres (supporting balls). Automatic meshing in the contact region can result in rough mesh failing to capture the geometry of the contact surfaces thereby introducing a small gap in the contact region. Since the physical probe does not have a gap between the tripod rod and supporting balls this may invalidate our FEA model. To overcome this problem, an adaptive fine meshing technique in the contact region is employed. Tripod rod and supporting balls forming six contact pairs are meshed with solid tetrahedral elements and a contact match is implemented for each of the six contact pairs as shown in Figure 2.7. This is done to ensure that the target elements can easily detect the nodes on the contact side, thus establishing closed initial contact.

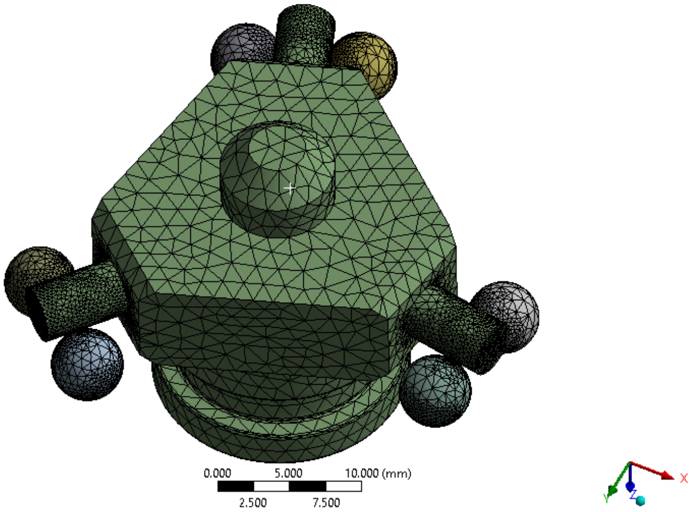

Figure 2.7: Mesh refinement at contacts

Figure 2.8 shows the initial geometric gap and penetration to be zero. This ensures that the contact between the tripod rod and the supporting ball is established prior to the solving stage.

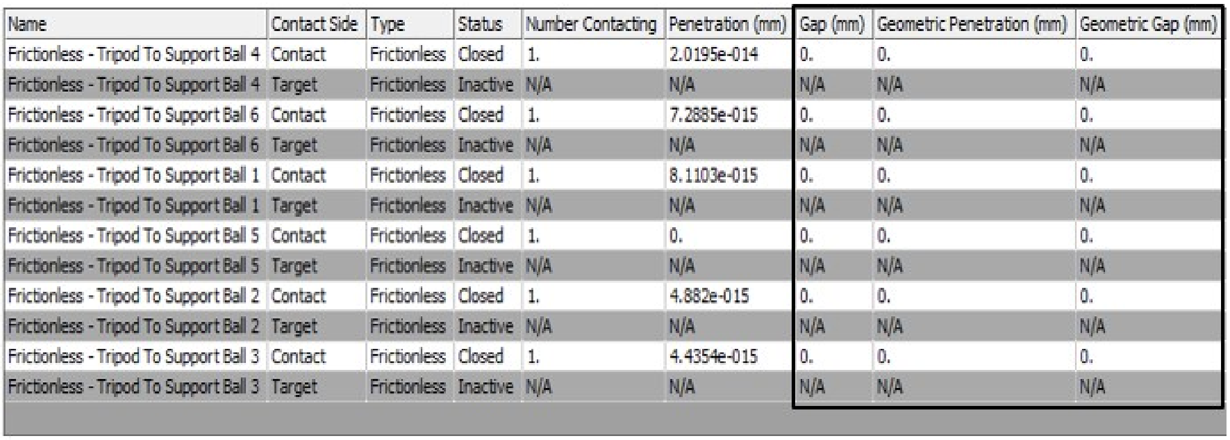

Name	Contact Side	Type	Status	Number Contacting	Penetration (mm)	Gap (mm)	Geometric Penetration (mm)	Geometric Gap (mm)
Frictionless - Tripod To Support Ball 4	Contact	Frictionless	Closed	1.	2.0195e-014	0.	0.	0.
Frictionless - Tripod To Support Ball 4	Target	Frictionless	Inactive	N/A	N/A	N/A	N/A	N/A
Frictionless - Tripod To Support Ball 6	Contact	Frictionless	Closed	1.	7.2885e-015	0.	0.	0.
Frictionless - Tripod To Support Ball 6	Target	Frictionless	Inactive	N/A	N/A	N/A	N/A	N/A
Frictionless - Tripod To Support Ball 1	Contact	Frictionless	Closed	1.	8.1103e-015	0.	0.	0.
Frictionless - Tripod To Support Ball 1	Target	Frictionless	Inactive	N/A	N/A	N/A	N/A	N/A
Frictionless - Tripod To Support Ball 5	Contact	Frictionless	Closed	1.	0.	0.	0.	0.
Frictionless - Tripod To Support Ball 5	Target	Frictionless	Inactive	N/A	N/A	N/A	N/A	N/A
Frictionless - Tripod To Support Ball 2	Contact	Frictionless	Closed	1.	4.882e-015	0.	0.	0.
Frictionless - Tripod To Support Ball 2	Target	Frictionless	Inactive	N/A	N/A	N/A	N/A	N/A
Frictionless - Tripod To Support Ball 3	Contact	Frictionless	Closed	1.	4.4354e-015	0.	0.	0.
Frictionless - Tripod To Support Ball 3	Target	Frictionless	Inactive	N/A	N/A	N/A	N/A	N/A

Figure 2.8: Initial geometric penetration and gap between contact pairs

The stylus stem as shown in Figure 2.9 is meshed using quadratic hexahedral mesh as it has superior performance over other 3D elements and is recommended for modeling structures where the bending behaviour is dominant in the structure [20].

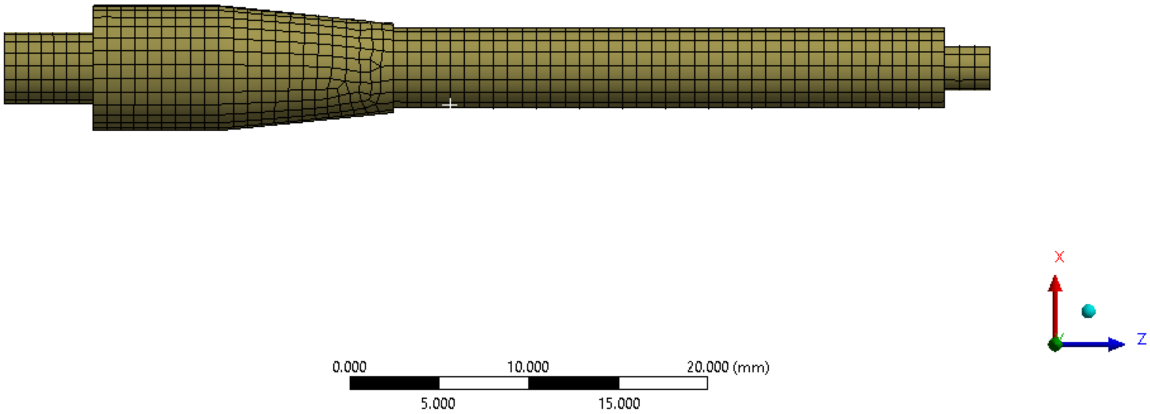

Figure 2.9: Quadratic hexahedral meshing of stylus stem

2.6 Boundary Conditions

In static structural analysis, the rigid body motion of the model must be restricted by specifying appropriate boundary conditions. Single point constraints are imposed on certain degrees of freedom that represent the physical conditions to ground the model [20]. The supporting balls made of tungsten carbide are placed on the basement plate as shown in Figure 2.10. They are placed in pairs and oriented 120 degrees apart along the probe axis. These supporting balls cannot be moved from their position. Since these six pairs of supporting balls are fixed, the geometric model of the basement is replaced by a fixed support boundary condition which restricts 3 translational and 3 rotational degrees of freedom.

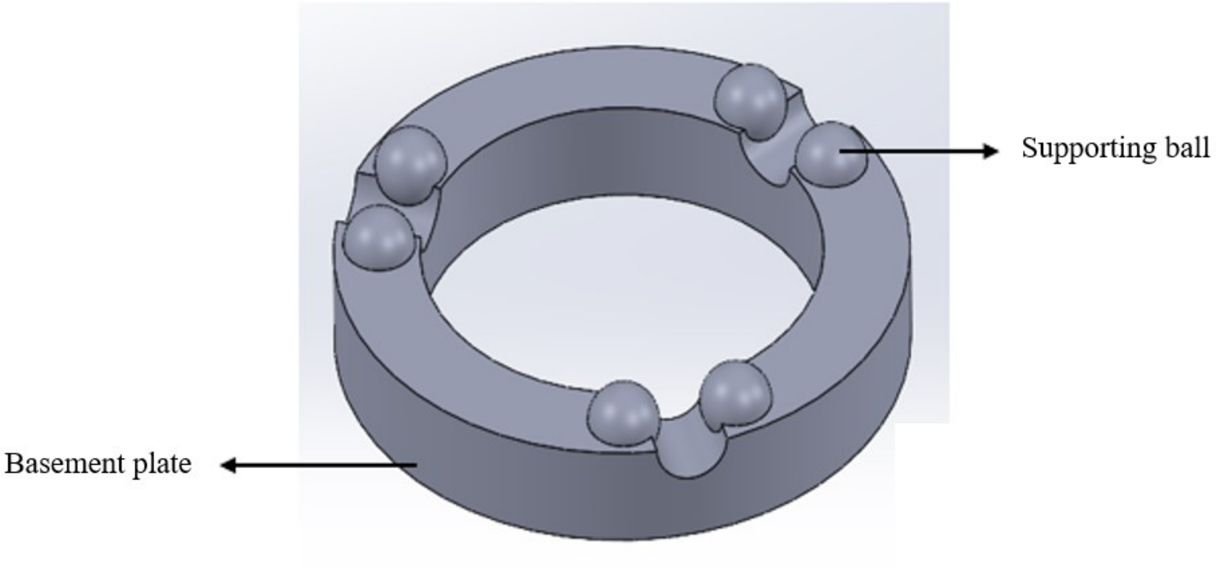

Figure 2.10: Six supporting balls fixed on the basement plate

The spring is preloaded using the adjustable locknut mechanism, thereby making the top end of the spring to be fixed as shown in Figure 2.11(b).

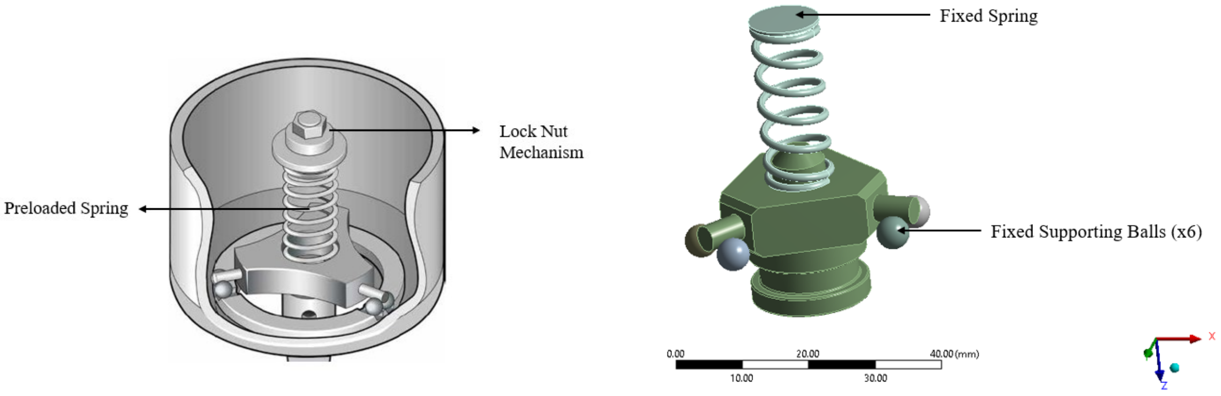

(a) (b)

Figure 2.11: (a) Lock nut mechanism in physical probe; (b) Fixed spring boundary condition

2.7 Load Conditions

The preloaded spring force is applied on the top of the tripod along the probe axis. In a physical probe, this preloaded force can be adjusted using a locknut mechanism. For the purpose of this research, the factory default of 5.91 N spring force is applied as shown in Figure 2.12. Since this force is pre-applied prior to applying the probing force, the load condition must simulate this phenomenon by having constant force from the beginning of the simulation time step.

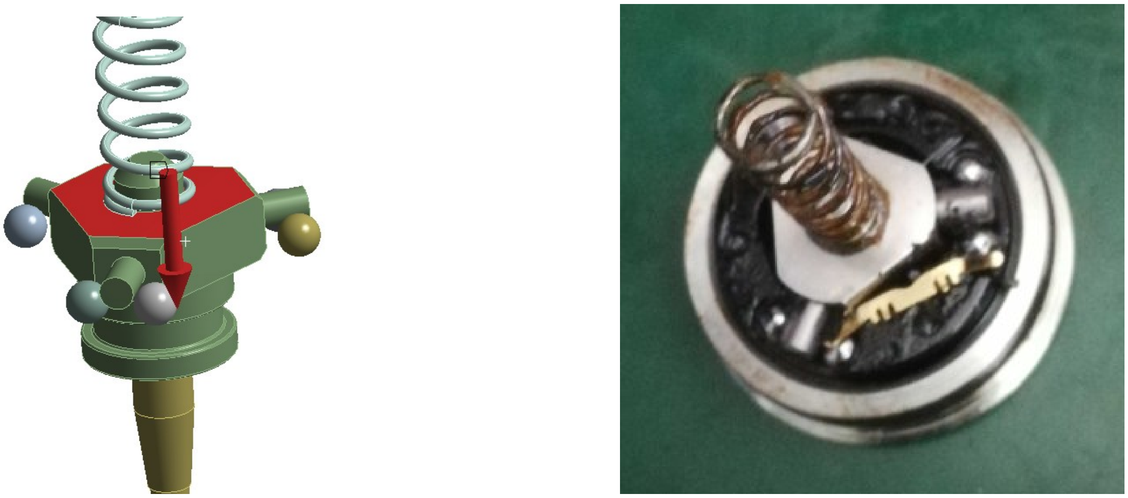

Figure 2.12: Preloaded spring force

When the probe meets the workpiece surface, the contact force called as probing force between the stylus tip and the workpiece starts to build up. The direction of this force depends on the workpiece surface being measured and is assumed to be in the normal direction at the point of contact. For a typical vertical surface workpiece, the direction of the probing force is perpendicular to the probe axis as shown in Figure 2.13.

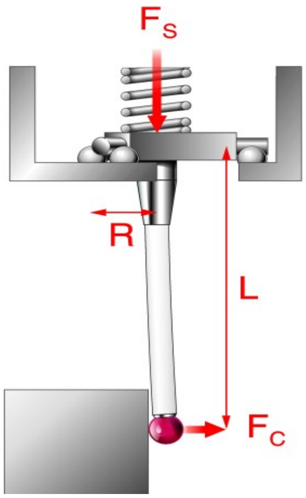

Figure 2.13: Probing force Fc

The probing force is applied at the center node of the stylus tip and is defined by the coordinate system located at the center of the stylus tip. The direction of the applied probing force can then be varied depending on the probe approach directions by transforming this coordinate system. This helps the probing force to be applied along a single axis i.e., in this case, x-axis, instead of applying the resolved components of the force to the node.

(a)

(b)

Figure 2.14: (a) Probe coordinate system, (b) Transformed probe coordinate system

The direction of the applied probing force to the probe tip depends on the approach directions. Various probe approach directions are studied in this research work in the case of vertical, inclined, and curved surface measurement. The representation of approach angles is shown in Figure 2.15. where, **θ** is the polar angle while **ϕ** is an azimuthal angle**.**

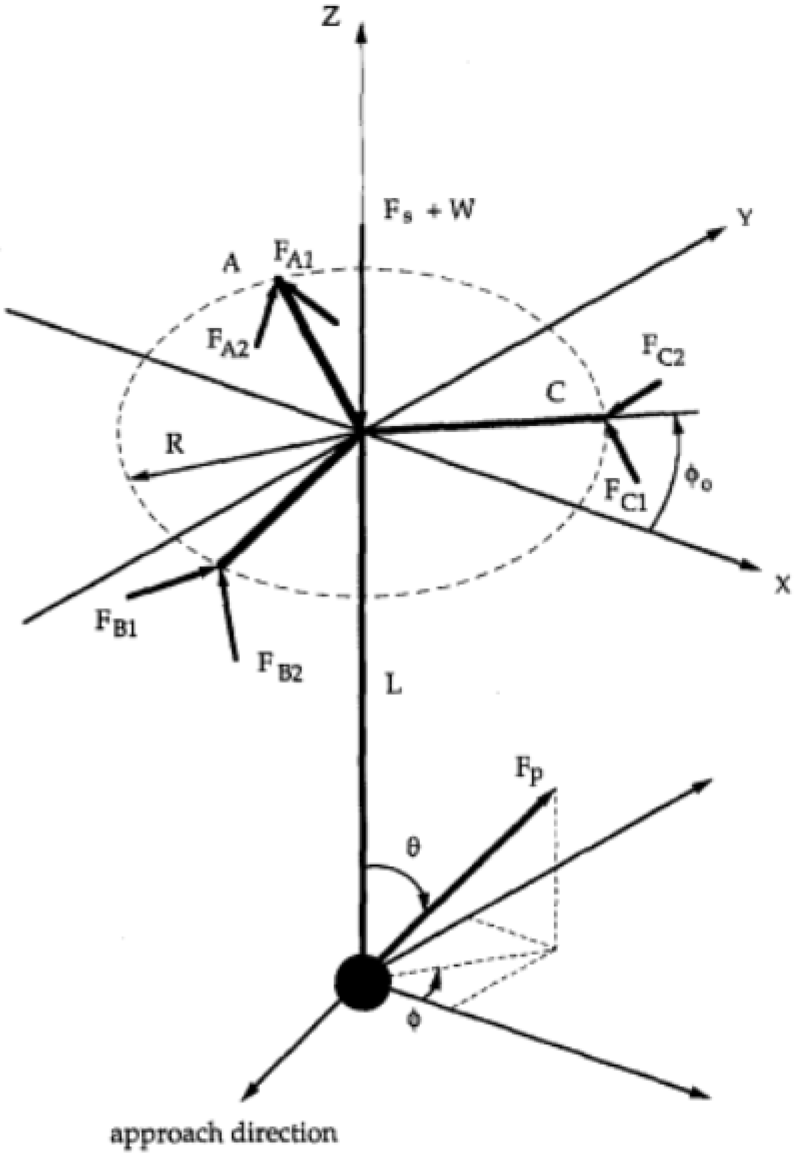

Figure 2.15: Free body diagram of vertically oriented probe showing approach directions [21]

2.8 Solver Settings in ANSYS Workbench

For a static structural analysis in an ANSYS workbench, two solver options are available. 1) Direct solver – sparse direct solver is used, 2) Iterative – preconditioned conjugate gradient solver is used [22]. Direct solvers are preferred for the problems that are computationally less expensive since this method involves inverting the stiffness matrix [K] and multiplying with load matrix {x}. Meanwhile, Iterative solvers begin with an initial solution and then iterate until a criterion is achieved usually a tolerance value. This solver is suitable for problems which are computationally more expensive such as nonlinear static analysis. For the latter case, FEA Model must be well constrained or the solver may run into convergence issues [23]. Since this research accompanies a nonlinear FEA Model, an iterative solver is recommended.

2.9 Verification of FEA Simulation Model

2.9.1 Trigger Force Verification

In order to verify this simulation model, we compare the simulation results of the proposed method with that of the existing mathematical pre-travel model [7] and the experimental results [9]. For the experimental results, the authors have developed a new setup for testing the triggering force of the kinematic probes and presented the characteristics of the triggering force of Renishaw's OMP40-2. The authors experimented under the quasi-static case where the probe approach speed of the probe was set to 0.05 mm/s. Since this method is based on the static case, these experimental results can be directly compared without significant deviation. Triggering force is independent of the stylus material and thus the experimental results presented by the authors, existing mathematical model, and this approach can be compared to verify the FEA simulation model.

Table 2.2: Triggering Force comparison between experimental, existing method and proposed simulation model results at 90-degree polar angle

	Experimental Results (N)	**Existing Model (N)**	**FEA Model (N)**
Minimum	0.664	0.965	0.75
Maximum	1.294	1.49	1.22

For the quasi-static case, the minimum triggering force in xy plane is 0.664 N, whereas the maximum triggering force is 1.294 N. Compared to that of the existing model, the results are over-estimated by the model. This is due to the over-simplification of the probe model. The stylus stem is considered as a uniform cross-section rather than using the geometric model of the standard stems. In addition, the existing model assumes the probe model to be a cantilever beam and thus completely ignores the fact that the tripod rods lift in order to trigger the probe. Although, the displacement of this lift is very small and can be ignored, its effect on the sensing distance cannot be ignored. On the other hand, the FEA simulation results are close to that of the experimental results. Some deviation may occur due to the measurement speed and other errors during the experiments.

2.9.2 Sensing Distance Verification

In order to verify the sensing distance, the experimental data needs to be carefully chosen. CNC machine tool itself is a source of error including vibrations, spindle position errors, and kinematic errors. In addition, the touch trigger probes installed on the machine tools usually utilize wireless communication in the radio or Infrared (IR) band. These means of communication cause a delay in trigger signal transmission when the probe triggers and sends a signal to the CNC Machine controller to latch the spindle position. Additionally, the signal filtering is on in order to avoid any false triggering of the probe. This adds to the overall delay in the signal transmission. Since the research assumes that the measurement speed is very slow and thus considered as a static case, direct comparison of the simulation results and that of experimental data is not possible. To overcome this problem, the experimental data must be chosen such that the measurement speed must be slow and the overall delay caused by a wireless communication interface at the time of experiments must be readily available. Thus, the results can be compensated for the sensing distance caused by this delay and compared with that of the simulation model.

Jankowski *et al.* [24] developed a method for testing the delay time of the triggering signal by the wireless communication system. Experiments were conducted on the CNC machine tool with Renishaw OMP40-2 probe equipped with a 100 mm stylus stem. The measurement speed was 50 mm/min (0.83mm/s) and the delay was equal to 14.5 ms.

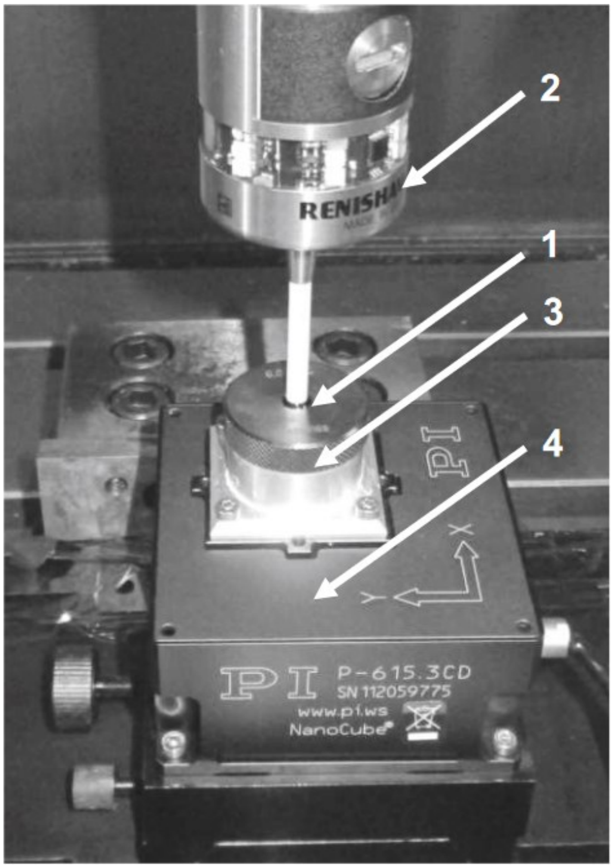

Figure 2.16: Part setup for probe testing [25]

The results of the measured triggering radius (mr_i) were recorded instead of the sensing distance (r_i). To directly compare the results, the values of sensing distance can be obtained using the formula,

$$mr_i = r_i + (r_G + r_{ST}) \tag{2.1}$$

where,

r_G = Radius of the measured gauge,

r_{ST} = Radius of the probe tip.

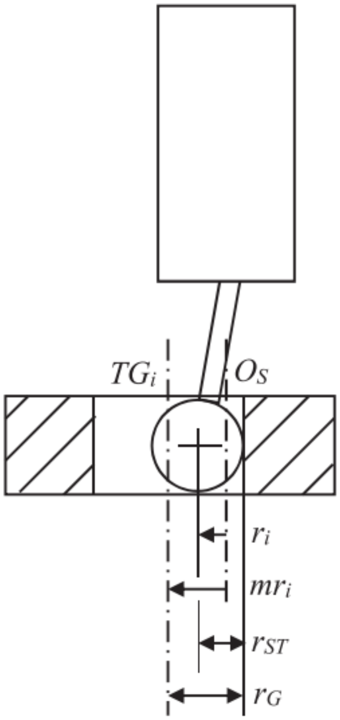

Figure 2.17: The sensing distance (r_i) and measured triggering radius (mr_i) [25]

Table 2.3: Sensing distance comparison between experimental, existing method and proposed simulation model results at 90-degree Polar angle

	Experimental Results (μm)	**Existing Model (μm)**	**FEA Model (μm)**
Minimum	15.875	19.36	16.11
Maximum	28.865	33.79	28.456

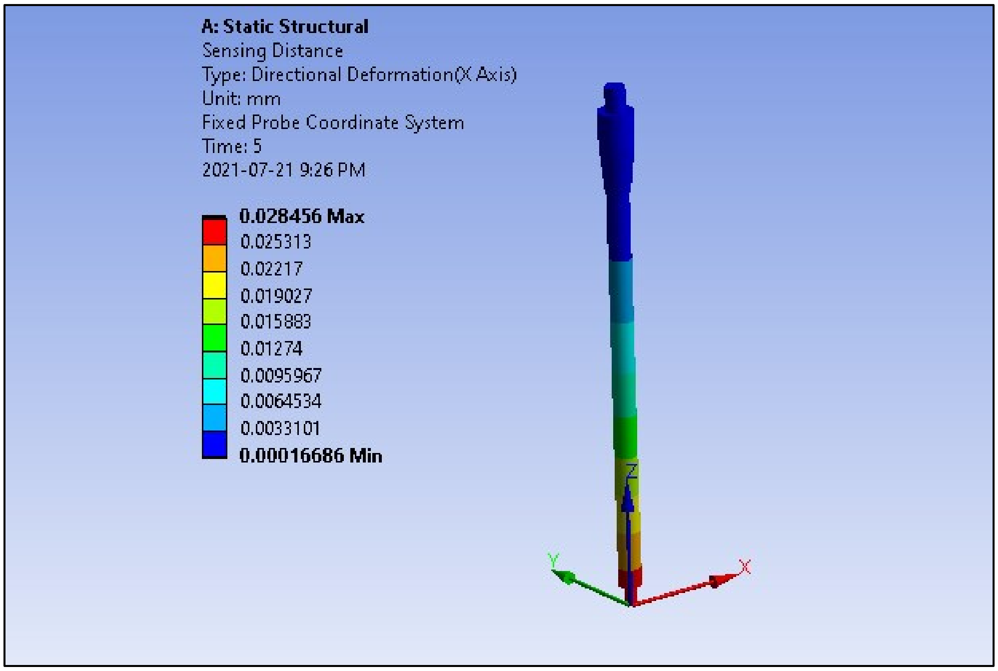

Figure 2.18: Sensing distance in high force direction from FEA simulation model (azimuthal angle = 60 degrees)

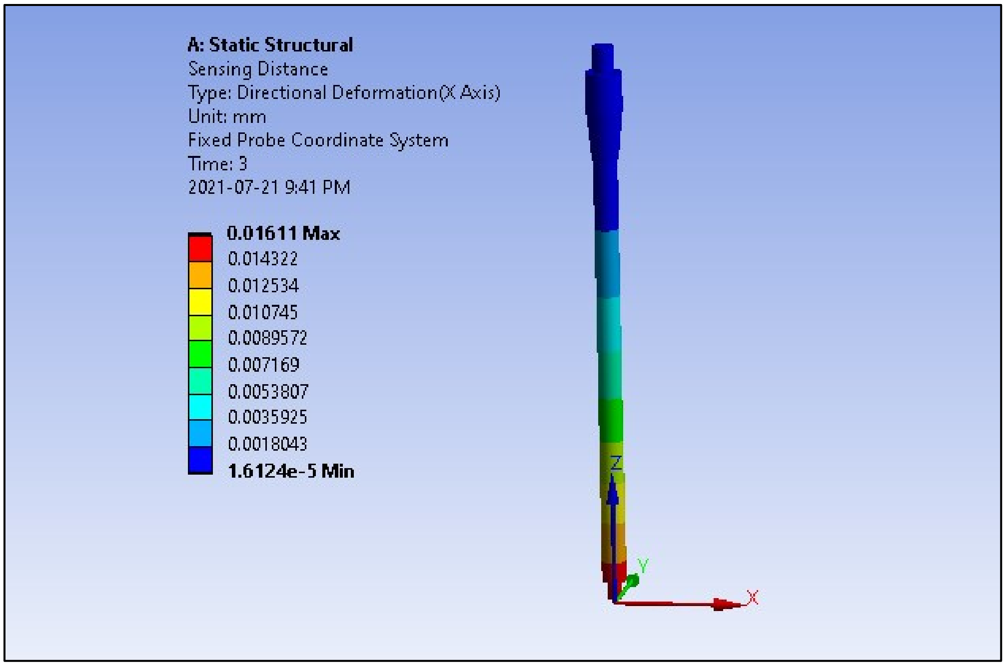

Figure 2.19: Sensing distance in low force direction from FEA simulation model (azimuthal angle = 0 degrees)

The compensated experimental, FEA simulation, and existing mathematical model results were then compared. The existing model overestimated the results due to the oversimplification and assumptions made by the authors. It can be concluded that the FEA simulation model is reliable and can be used to find the sensing distance taking into consideration the sliding effects of the probe tip on the part surface.

Chapter 3: Novel Algorithm for Surface Measurement

3.1 Introduction

As observed in the previous chapter, the sensing distance model results [7] are over-estimated when compared to the experimental results as a result of over-simplification of the probe model and neglecting the sliding effect between the probe tip and the part surface. Thus, there is a need for a new method that can provide more accurate results by not simplifying the probe geometry and considering the sliding effects.

In this chapter, a new mathematical model for the surface measurement in the case of the vertical surface, inclined surface, and curved surface accompanied by the FEA methods in determining the sensing distance are discussed. Finally, the compensation of the surface measurement error is discussed in brief.

3.2 Mathematical Modeling of Sensing Distance for Vertical Surface

Sensing distance modeling in case of vertical surface measurement is discussed in this section. The illustration of the vertical flat surface is as shown in Figure 3.1.

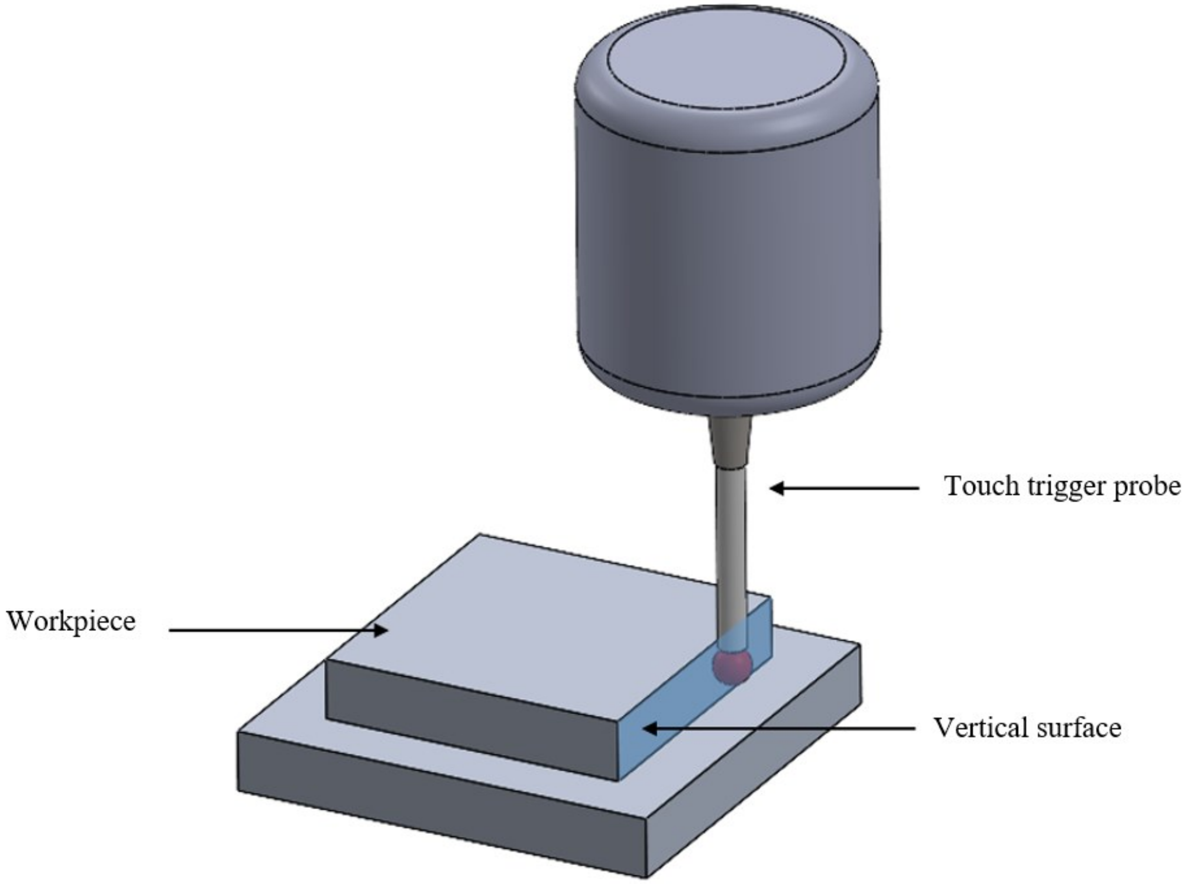

Figure 3.1: Vertical surface measurement illustration

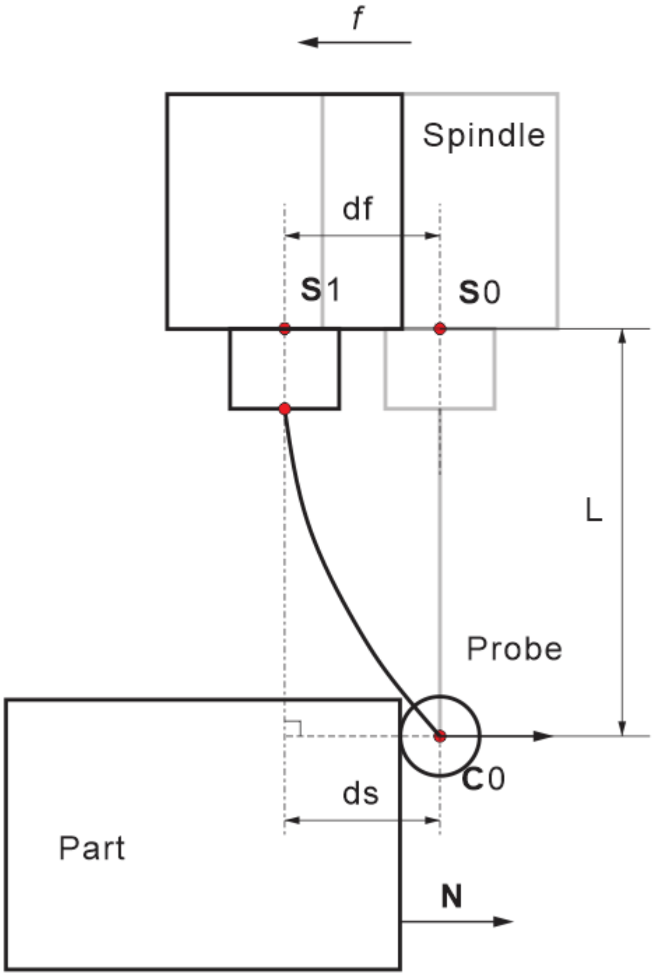

Figure 3.2: Vertical surface probing process

As demonstrated in Figure 3.2, the probe is installed on the spindle of the machine tool and is fed towards the part surface at a small feed rate f. The length of the probe stylus is L. The direction of the feed is opposite to the surface normal **N**. When the probe tip touches the part surface initially, its center is located at $\mathbf{C}_0$ and the center of the spindle is at $\mathbf{S}_0$. The probe does not trigger at this stage and thus the spindle will drive the probe to move forward along the original feed direction. However, under this situation, the probe tip is obstructed by the part surface. Since the probing feed rate is very small, the probe stylus can be considered to be under the static load condition and it deflects by the effect of the probing force $\mathbf{F}_p$. At the instance, when the spindle reaches $\mathbf{S}_1$, the distance between the initial and current spindle positions $\mathbf{S}_0$ and $\mathbf{S}_1$ is given by $\mathrm{d_f}$, which is along the original feed direction. The distance between the center of the probe tip $\mathbf{C}_0$ and the probe axis when the spindle center reaches $\mathbf{S}_1$ is $\mathrm{d_s}$.

The distance $\mathrm{d_s}$ is perpendicular to the probe axis. According to the material of mechanics, $\mathrm{d_s}$ is also the amount of deflection of the probe stylus at this instant, since the deflection of the probe stylus along the axial direction of the probe is negligible i.e., less than thou that of in the radial direction. If the probe is triggered at this instance, the current $\mathrm{d_s}$ is called the sensing distance. In other words, sensing distance,

$$\mathrm{d_{sd}} = \max\left(\mathrm{d_s}\right) \tag{3.1}$$

The probe tip is in contact with the flat surface. So, the force $\mathbf{F}_\mathrm{p}$ is perpendicular to the part surface and along the surface outward normal **N.** In this case, it can be noted that $\mathrm{d_s}$, $\mathrm{d_f}$, $\mathbf{F}_\mathrm{p}$ and f are parallel to the same direction **N.**

3.2.1 FEA Modeling of Sensing Distance for Vertical Surface

To model and predict the sensing distance $\mathrm{d_{sd}}$, Finite Element Modeling technique is implemented. In this model, we input a small amount of $\mathrm{d_s}$ perpendicular to the probe axis. The six contact reaction forces between the tripod rods and supporting balls are monitored. If one or more of the reaction forces reaches zero first, the probe is said to be triggered. Else, we continue with the iterative process by increasing the amount of $\mathrm{d_s}$. The process is stopped when the probe is triggered. The distance $\mathrm{d_s}$ at the triggered instance is the sensing distance $\mathrm{d_{sd}}$. Usually, the smallest unit of a CNC machine is 1 μm. Thus, it is logical to set the initial displacement $\mathrm{d_s}$ to be 1 μm and increment it by 1 μm if necessary. The FEA process flowchart for the flat surface measurement is shown in Figure 3.3.

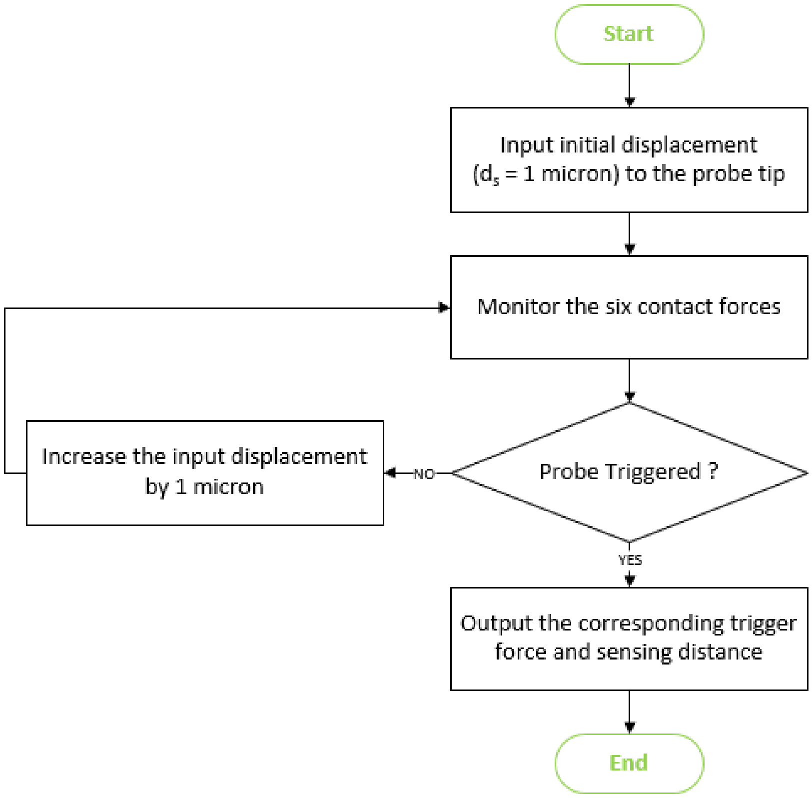

Figure 3.3: Flowchart of vertical surface FEA process

3.2.2 Vertical Surface Measurement – Simulation Process

In the case of vertical flat surface measurement, the displacement d_S is applied at the node located at the center of the probe tip. The direction of this nodal displacement is defined by the nodal coordinate system as shown in Figure 3.4. Nodal orientation object is applied pointing to the nodal coordinate system so that the approach directions given by azimuthal and polar angles can be defined using this coordinate system. The simulation was performed for azimuthal angles from 0 to 350 degrees with an interval of 10 degrees, while the polar angle was held constant at 90 degrees indicating a vertical surface. The simulation process was automated using the ANSYS ACT script utilizing a golden section search algorithm to speed up the simulation process.

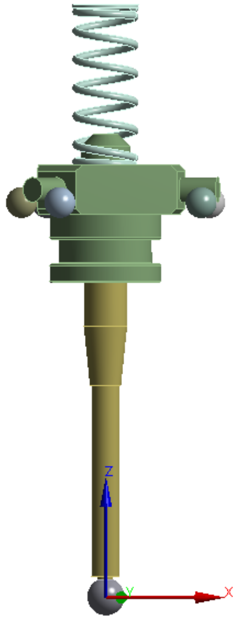

Figure 3.4: Nodal coordinate system in FEA model

Probing parameters used in the vertical surface measurement are shown in the Table 3.1.

Table 3.1: Vertical surface measurement parameters

Parameter	**Value**
Preloaded spring force	5.91 N
Stylus stem length	50 mm
Stylus stem diameter	4.5 mm
Support angle	27.266 degrees
Tripod radius	16.34 mm
Polar angle	90 degrees
Azimuthal angle	0 – 350 degrees
Stylus stem material	Ceramics, Stainless steel

3.3 Mathematical Modeling of Sensing Distance for Inclined Surface

Sensing distance modeling in case of inclined surface measurement is discussed in this section. The inclined surface to be measured is as shown in Figure 3.5.

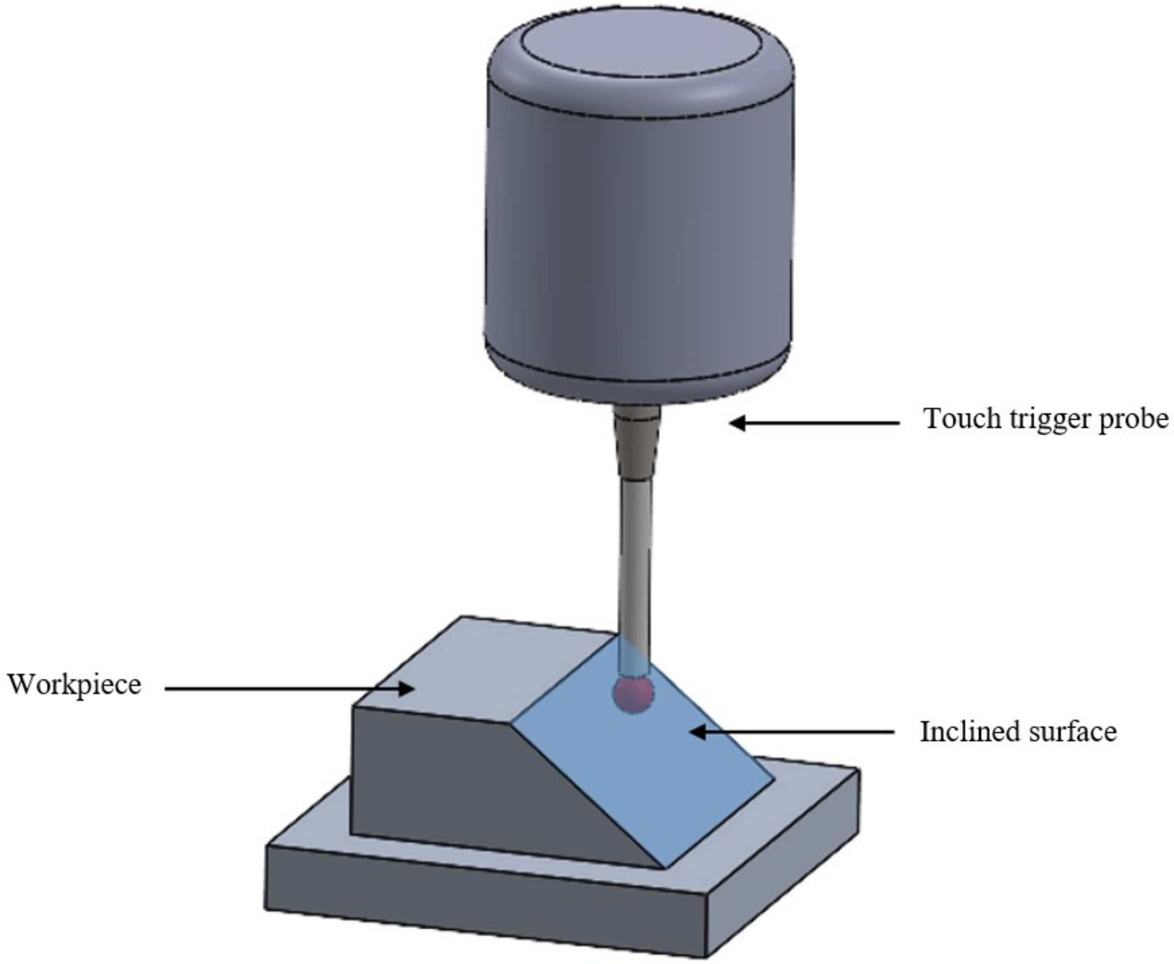

Figure 3.5: Inclined surface measurement illustration

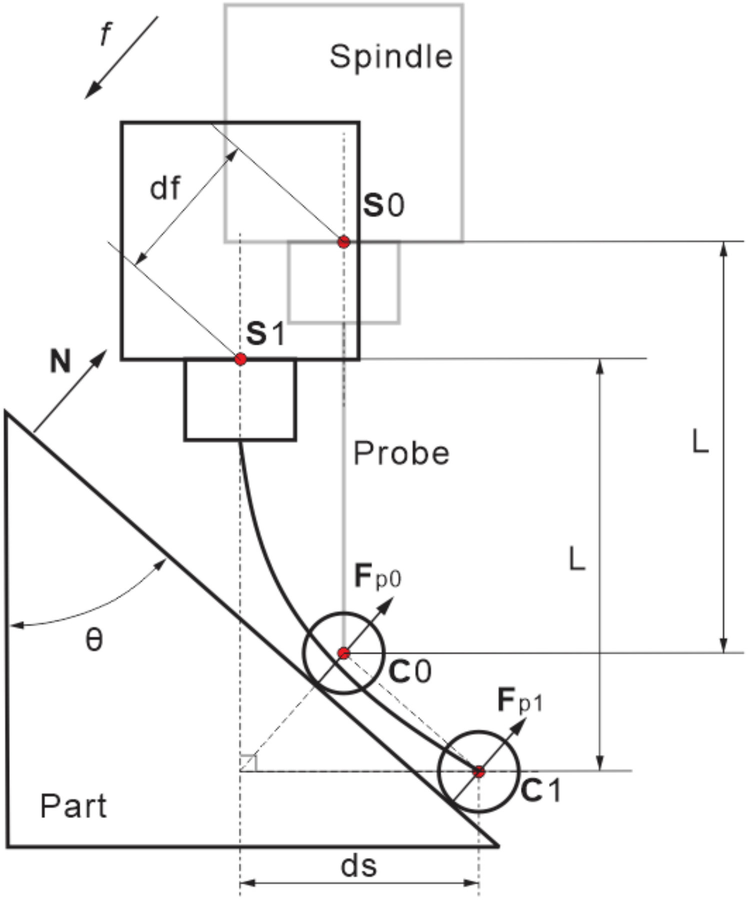

Figure 3.6: Inclined surface probing process

As illustrated in Figure 3.6, the probe is installed on the spindle of the machine tool. The spindle drives the probe towards the inclined surface at a very small feed rate f. The direction of feed is opposite to that of the part surface outward normal **N.** The length of the probe stylus is L. When the probe touches the part surface initially, its center is located at $\mathbf{C}_0$ and the center of the spindle is at $\mathbf{S}_0$. At this instant, the probe will not trigger and thus the spindle will continue to drive the probe along the original feed direction. The probe stylus is deflected by the effect of the probing force $\mathbf{F}_p$, which is perpendicular to the part surface. When the spindle reaches $\mathbf{S}_1$, the distance between the initial and current spindle positions $\mathbf{S}_0$ and $\mathbf{S}_1$ is d_f, which is along the original feed direction.

According to mechanics of material, the stylus of the probe will deflect along its radial direction i.e., perpendicular to the probe axis. Thus, in this case, unlike probing of the vertical surface, the probe tip will not be in its initial position at $\mathbf{C}_0$ when the spindle reaches $\mathbf{S}_1$. Instead, it will tend to slide on the inclined surface and reach point $\mathbf{C}_1$. The distance between $\mathbf{S}_1$ and $\mathbf{C}_1$ along the axial direction at this instance remains to be the length of the probe stylus L. The distance between the probe tip center $\mathbf{C}_1$ and the probe axis when the spindle reaches $\mathbf{S}_1$ is $\mathrm{d_s}$. However, note that $\mathrm{d_s}$ and $\mathrm{d_f}$ are not along the same direction as they were in the previous case.

The relation between $\mathrm{d_s}$ and $\mathrm{d_f}$ can be defined geometrically with the following equation:

$$\mathrm{d_s} = \frac{\mathrm{d_f}}{\cos\theta} \tag{3.2}$$

where, θ in degrees is the angle of the inclined surface relative to the vertical surface. It can be noticed that for the same distance travelled by the probe, the probe stylus deflects more in case of the inclined surface probing in comparison to vertical flat surface probing.

3.3.1 FEA Modeling of Sensing Distance for Inclined Surface

To model and predict the sensing distance $\mathrm{d_{sd}}$, FEA modeling technique is implemented. Similar to that of vertical surface probing, this case involves an iterative process. We input a small probing force $\mathbf{F}_\mathrm{p}$ at the probe tip along the direction given by azimuthal and polar angles and to obtain the corresponding stylus deflection amount $\mathrm{d_s}$. The six reaction forces at the tripod and supporting balls interface are monitored. If one or more of the reaction forces reach zero first, the probe is said to be triggered. If the probe does not trigger under this applied probing force $\mathbf{F}_\mathrm{p}$, we increase $\mathbf{F}_\mathrm{p}$ by a small amount and obtain the corresponding stylus deflection $\mathrm{d_s}$. This process is repeated iteratively until the probe is triggered. The maximum $\mathbf{F}_\mathrm{p}$ and $\mathrm{d_s}$ are then captured as the triggering force and the sensing distance $\mathrm{d_{sd}}$.

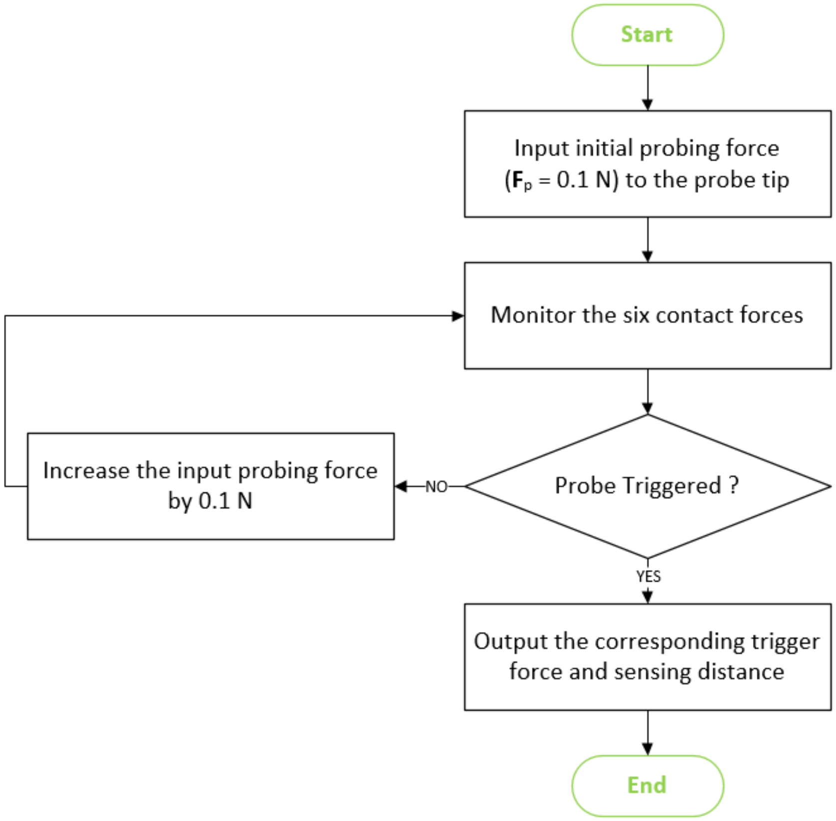

Figure 3.7: Flowchart of inclined surface FEA process

3.3.2 Inclined Surface Measurement - Simulation Process

The simulation process in the case of the inclined surface is slightly similar to that of the vertical surface. Instead of applying the displacement d_s in the earlier case, we apply a probing force $\mathbf{F}_p$ at the node located at the center of the probe tip. The direction of this nodal force is defined by the nodal coordinate system as shown in Figure 3.8. Specifically, the nodal force is applied along the x-axis of this coordinate system. To apply the force in required polar and azimuthal angles, the coordinate system can be transformed accordingly thus eliminating the process of resolving the probing force into its components as shown in Figure 3.9. Nodal orientation object is applied pointing to the nodal coordinate system, so that the approach directions given by azimuthal and polar angles can be defined using this coordinate system. The simulation was performed for azimuthal angles from 0 to 350 degrees with an interval of 10 degrees, while the polar angle was varied from 10 to 80 degrees with an interval of 10 degrees. The simulation process was automated using the ANSYS ACT script utilizing the golden section search algorithm.

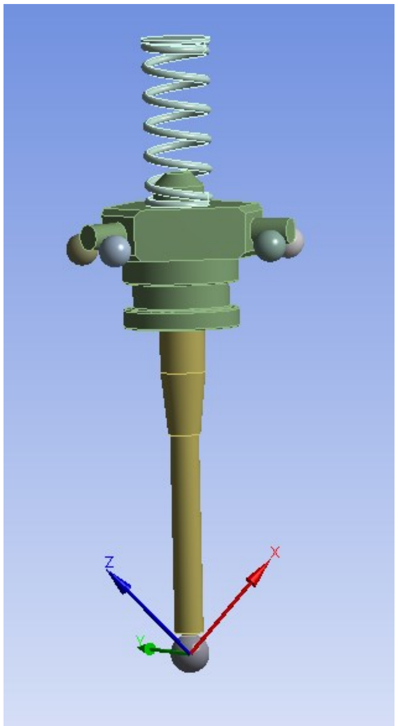

Figure 3.8: Transformed nodal coordinate system

In Figure 3.9, azimuthal angle can be set in Rotate Z configuration, while the polar angle can be set in Rotate Y configuration.

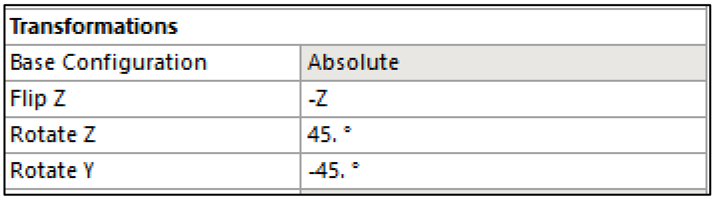

Transformations	
Base Configuration	Absolute
Flip Z	-Z
Rotate Z	45. °
Rotate Y	-45. °

Figure 3.9: Transformation of nodal coordinate system

Probing parameters used in the inclined surface measurement are shown in Table 3.2.

Table 3.2: Inclined surface measurement parameters

Parameter	**Value**
Preloaded spring force	5.91 N
Stylus stem length	50 mm
Stylus stem diameter	4.5 mm
Support angle	27.266 degrees
Tripod radius	16.34 mm
Polar angle	10 – 80 degrees
Azimuthal angle	0 – 350 degrees
Stylus stem material	Ceramics, Stainless steel

3.4 Mathematical Modeling of Sensing Distance for Curved Surfaces

Sensing distance modeling in case of curved surface measurement is discussed in this section.

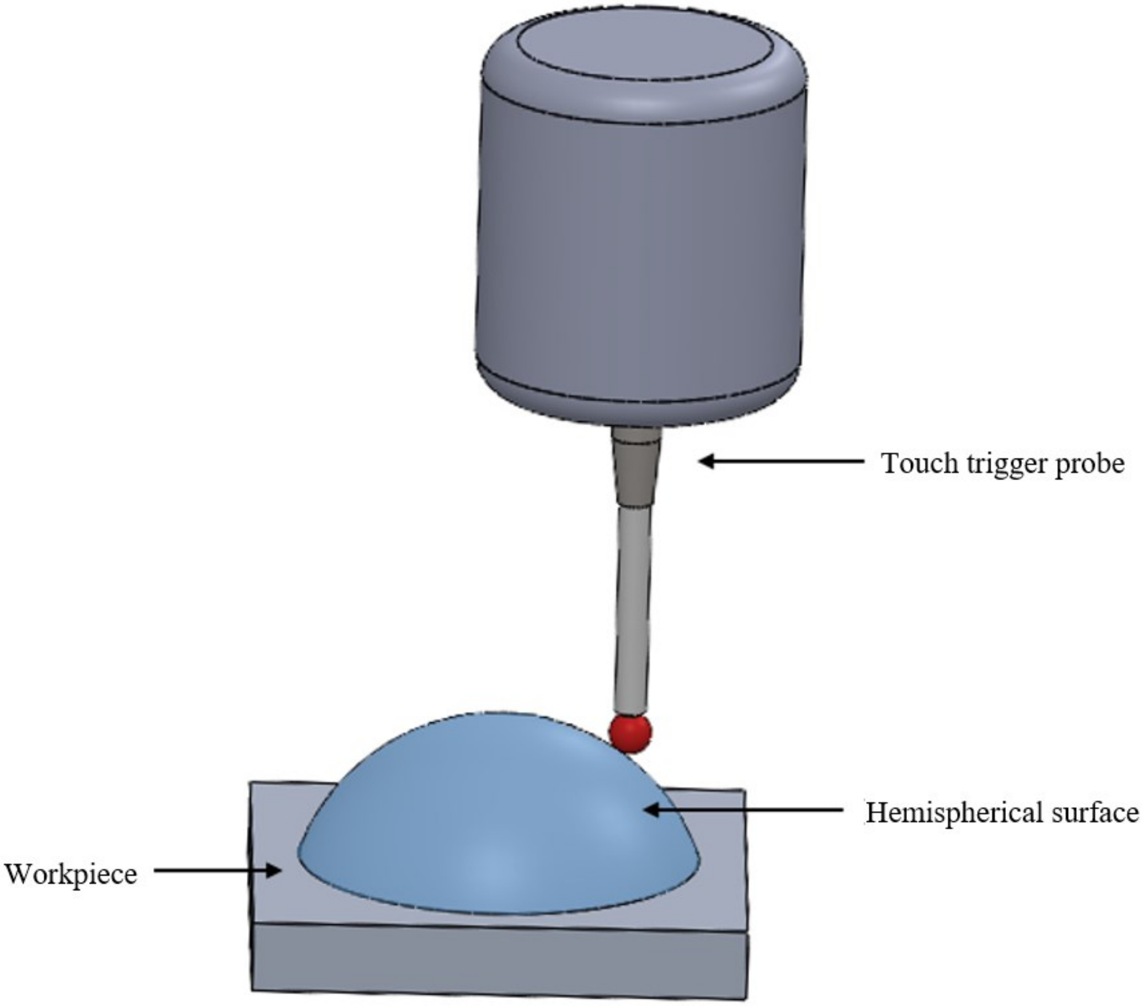

Figure 3.10: Curved surface probing illustration

The probing process of a curved surface is illustrated in Figure 3.11. The probe is installed on the probe spindle. The spindle drives the probe towards the part surface at a very small feed rate f along the direction opposite to the surface unit normal vector $\mathbf{N}_0$ or along the inward unit normal vector $\mathbf{N}_{\mathbf{0(in)}}$. The initial point of contact $\mathbf{T}_0$ between the probe tip and the surface being measured is known prior. The length of the probe stylus is L. Initially when the probe touches the part surface, the center of the probe tip is located at $\mathbf{C}_0$ and the spindle center is at $\mathbf{S}_0$. However, the probe does not trigger at this point and thus the spindle will keep driving the probe to move forward along the original feeding direction. The probe stylus is deflected by the effect of probing force $\mathbf{F}_{p0}$, which is directed along the surface unit normal vector $\mathbf{N}_0$.

Similar to the case of probing inclined surface, the probe stylus deflection direction is always along the probe stylus radial direction which is different from that of feeding direction. Curved surfaces usually have different surface normal vectors at different points throughout the surface. The direction of the force exerted on the probe tip is always along the surface normal at a point. Thus, as the probe slides from one point to another, the surface normal varies and thus the direction of probing force will vary. As a result, the direction of probe stylus deflection will vary accordingly. To model this intricate phenomenon, the following assumption is made: For a G1 continuous curved surface, the direction of the surface normal remains constant in a small region on the surface. Using this assumption, the probing process is considered as a pattern of several sub processes. Thus, in each of the subprocess, the probing process of the curved surface is simplified as the case of an inclined surface, where the surface normal remains constant.

In the first subprocess, the center of the spindle moves from $\mathbf{S}_0$ to $\mathbf{S}_1$ and the distance between two spindle positions $\mathbf{S}_0$ and $\mathbf{S}_1$ is d_f, which is directed along the original feed direction. The probe slides from point $\mathbf{C}_0$ to $\mathbf{C}_1$. The distance between the current spindle center $\mathbf{S}_1$ and current probe tip center $\mathbf{C}_1$ along the axial direction remains to be the length of the stylus L. The distance between the probe center $\mathbf{C}_1$ and the probe axis when the spindle reaches $\mathbf{S}_1$ is d_{s1}.This d_{s1} is directed along the $\mathbf{V}_0$, which is in the direction of the projection of $\mathbf{F}_{p0}$ on a plane perpendicular to the probe stylus axis, according to the mechanics of material.

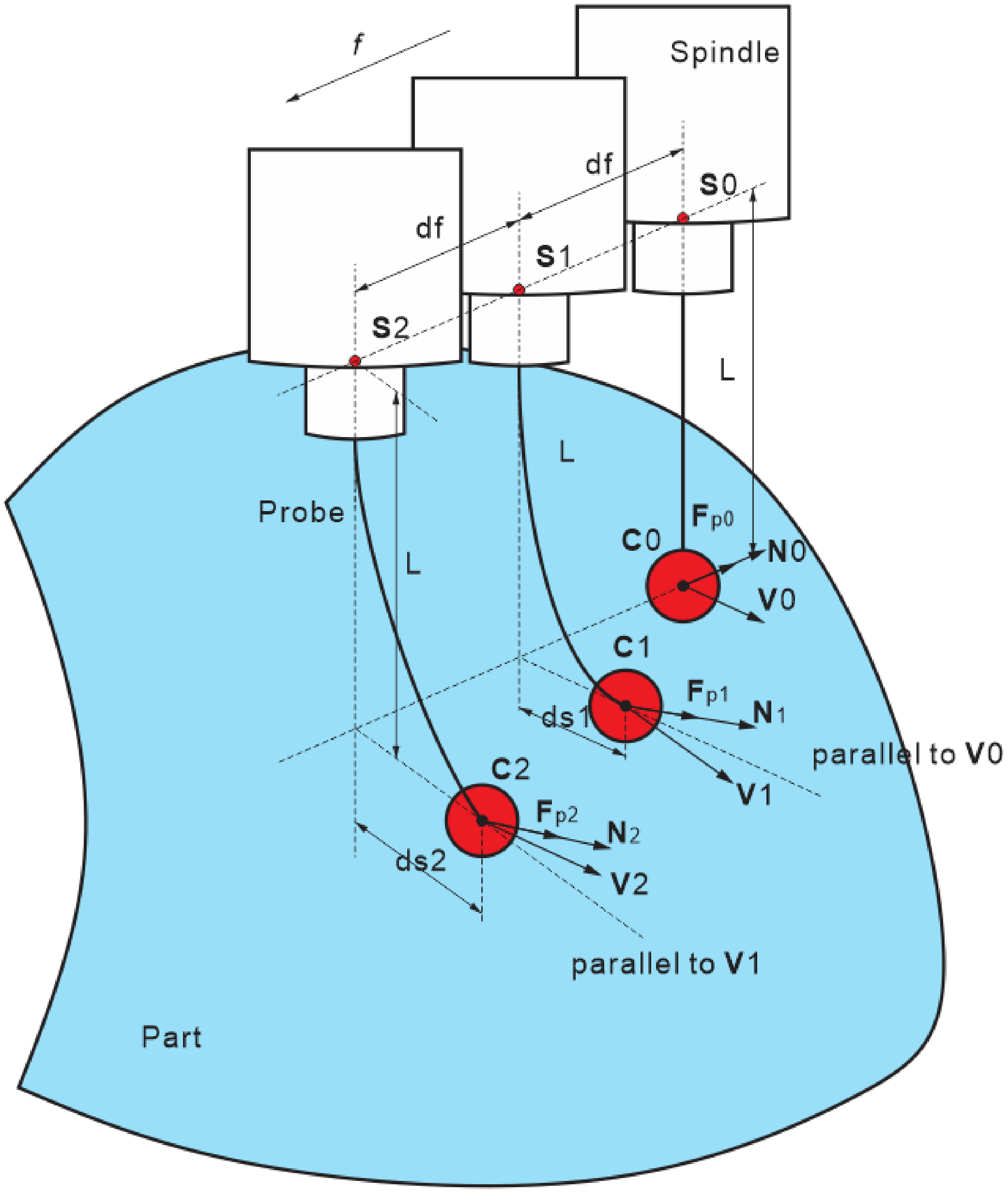

Figure 3.11: Curved surface probing process

The second subprocess begins with the spindle located at $\mathbf{S}_1$ and the probe tip located at $\mathbf{C}_1$. Assuming that the probe has not triggered in the first subprocess, the spindle will continue to move along the original feed direction, opposite to the surface unit normal vector $\mathbf{N}_0$. The probe stylus deflects under the probing force $\mathbf{F}_{p1}$. When the spindle location reaches $\mathbf{S}_2$, the probe tip center is at $\mathbf{C}_2$. The distance between $\mathbf{S}_2$ and $\mathbf{C}_2$ along the axial direction of the probe remains to be of length

L. The distance between the probe center $\mathbf{C}_2$ and the probe axis when the spindle is at $\mathbf{S}_2$ is $\mathrm{d}_{\mathrm{s}2}$. This $\mathrm{d}_{\mathrm{s}2}$ is directed along $\mathbf{V}_1$, which is the direction of projection of $\mathbf{F}_{\mathrm{p}1}$ on a plane perpendicular to the probe axis, according to the mechanics of material. These subprocesses will continue until the probe is triggered and the final deflection of the probe stylus obtained is the sensing distance d_{sd}.

Due to the varying probing force direction across different subprocesses, to model and predict the sensing distance d_{sd}, FEA modeling technique is utilized as a basis to verify if the probe is triggered, given an input deflection amount d_{s} and the direction of the probing force $\mathbf{F}_{\mathrm{p}k}$. The following section describes the solution of the model.

For any sub process, the azimuthal angle ($\boldsymbol{\alpha}$) and polar angle ($\boldsymbol{\beta}$) of the probing force direction can be obtained by

$$\boldsymbol{\alpha} = \tan^{-1}\left(\frac{\mathbf{N}_{k\mathbf{y}}}{\mathbf{N}_{k\mathbf{x}}}\right), \tag{3.3}$$

$$\boldsymbol{\beta} = \cos^{-1}(\mathbf{N}_{k\mathbf{z}}) \tag{3.4}$$

where, $\mathbf{N}_{k\mathbf{x}}$, $\mathbf{N}_{k\mathbf{y}}$ and $\mathbf{N}_{k\mathbf{z}}$ are the three components of the surface normal vector $\mathbf{N}_{k}$. Figure 3.12 describes the relationship between the contact point of the probe tip $\mathbf{T}_k$ with the part surface, the center point of the probe tip $\mathbf{C}_k$, the stylus deflection amount $\mathrm{d}_{\mathrm{s}k}$ and the distance travelled by the spindle along the feed direction d_{f}.

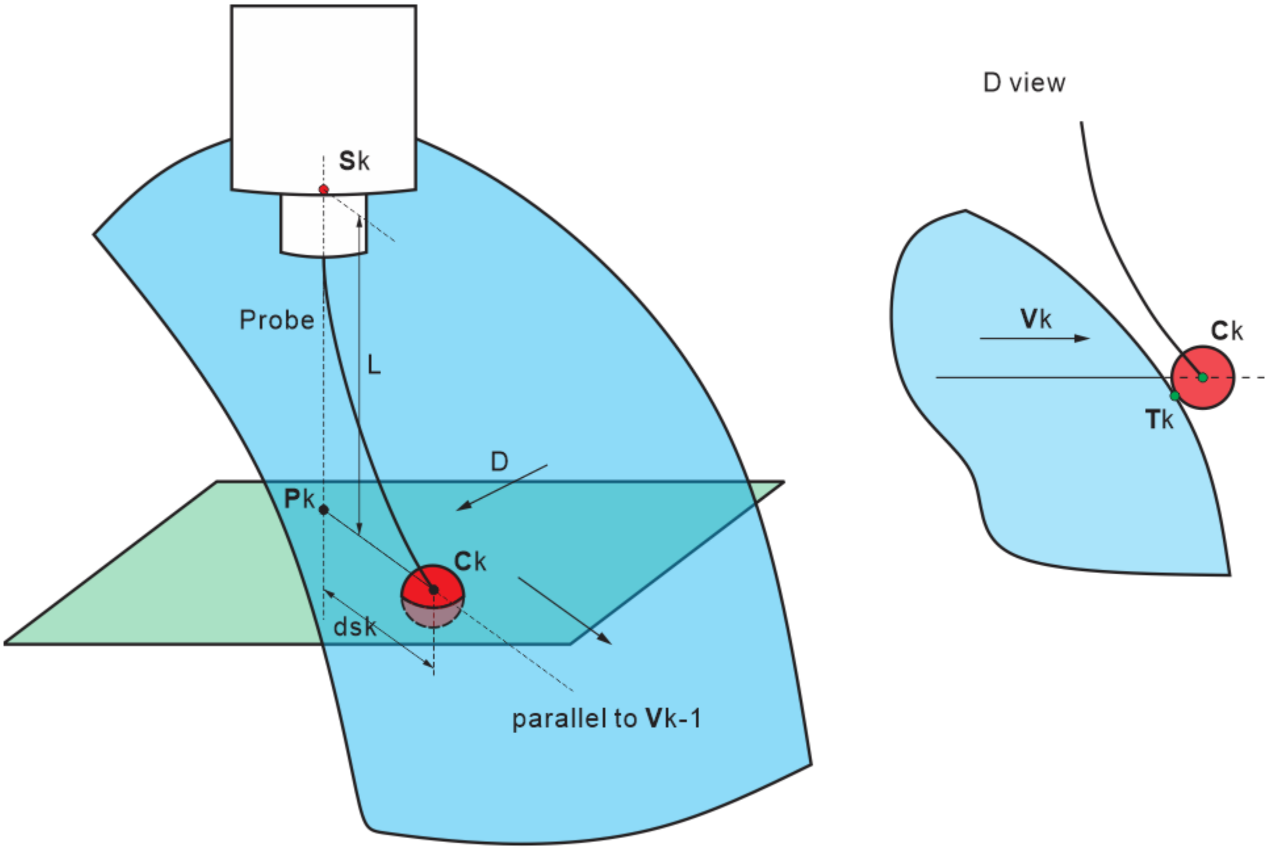

Figure 3.12: Geometrical relationships at any sub process

The center of the spindle $\mathbf{S}_k$ can be located in any sub process k as,

$$\mathbf{S}_{\boldsymbol{k}} = \mathbf{S}_{\mathbf{0}} + k \cdot \mathrm{d_f} \cdot \mathbf{N}_{\mathbf{0}(\boldsymbol{in})}, \qquad k \in [1,2,3,\ldots] \tag{3.5}$$

The point $\mathbf{P}_k$ lies vertically below the spindle center and can be obtained by

$$\mathbf{P}_{\boldsymbol{k}} = \mathbf{S}_{\boldsymbol{k}} - \mathrm{L} \cdot \begin{bmatrix} 0 \\ 0 \\ 1 \end{bmatrix} \tag{3.6}$$

A plane can be constructed such that it passes through point $\mathbf{P}_k$ and is perpendicular to the probe axis, as shown in the Figure 3.12. On this plane, a ray can be drawn, starting from the point $\mathbf{P}_k$, and directed along the vector $\mathbf{V}_{k\text{-}1}$. $\mathbf{V}_{k\text{-}1}$ is a vector that determines the direction of probe stylus deflection. The probe tip center $\mathbf{C}_k$ lies on this ray. It can be determined using the constraint optimization that the sphere is tangent to the part surface. The point of contact, also called as tangency point of the probe tip and the part surface is $\mathbf{T}_k$. The deflection is then calculated as,

$$d_{sk} = |\mathbf{C}_k - \mathbf{P}_k| \tag{3.7}$$

Now, in order to find the direction of the probing force for the next sub process, the surface normal vector for the current sub process is calculated as

$$\mathbf{N}_k(\mathbf{T}_{k\mathrm{x}}, \mathbf{T}_{ky}, \mathbf{T}_{k\mathrm{z}}) = \begin{bmatrix} -\dfrac{\partial f(x,y)}{\partial x} \\ -\dfrac{\partial f(x,y)}{\partial y} \\ 1 \end{bmatrix} \tag{3.8}$$

where, $z - f(x,y) = 0$ is the function of the curved surface, $\mathbf{T}_{kx}, \mathbf{T}_{ky}, \mathbf{T}_{k\mathrm{z}}$ are the coordinates of the tangency point between the probe tip and the part surface $\mathbf{T}_k$. The vector $\mathbf{V}_k$ is the component of normal vector in xy plane, and it determines the direction of stylus deflection for the next sub process, it can be calculated as,

$$\mathbf{V}_k = \begin{bmatrix} -\dfrac{\partial f(x,y)}{\partial x} \\ -\dfrac{\partial f(x,y)}{\partial y} \\ 0 \end{bmatrix} \tag{3.9}$$

Let $\boldsymbol{S}_1(u_1, v_1)$ be the generic curved part surface given by the parametric equation,

$$\boldsymbol{S}_1(u_1, v_1) = \begin{bmatrix} x(u_1, v_1) \\ y(u_1, v_1) \\ z(u_1, v_1) \end{bmatrix} \tag{3.10}$$

where, u_1, v_1 are the parameters of surface $\boldsymbol{S}_1$. Also, the probe tip sphere surface $\boldsymbol{S}_2$ with radius $\boldsymbol{r}$ and center $\mathbf{C}_k$ ($\mathbf{C}_{k\mathrm{x}}$, $\mathbf{C}_{ky}$, $\mathbf{C}_{kz}$) can be parametrically represented by the equation,

$$\boldsymbol{S_2}(u_2, v_2) = \begin{bmatrix} \mathbf{C}_{k\mathrm{x}} + \boldsymbol{r} \cdot \cos u_2 \cdot \sin v_2 \\ \mathbf{C}_{k\mathrm{y}} + \boldsymbol{r} \cdot \sin u_2 \cdot \sin v_2 \\ \mathbf{C}_{k\mathrm{z}} + \boldsymbol{r} \cdot \cos v_2 \end{bmatrix}, \tag{3.11}$$

$$0 \leq u_2 \leq 2\pi,$$

$$0 \leq v_2 \leq \pi.$$

where, u_2, v_2 are the parameters of the spherical probe tip surface $\boldsymbol{S_2}$. The center of the probe tip $\mathbf{C}_k$ lies on the line $\boldsymbol{L}(t)$ passing through point $\mathbf{P}_k$ and parallel to the vector $\mathbf{V}_{k\text{-}1}$ that describes the direction of the deflection of the stylus stem. This line can be parametrically defined as,

$$\boldsymbol{L}(t) = \begin{bmatrix} \mathbf{S}_{k\mathrm{x}} + \mathbf{V}_{(k-1)\mathrm{x}} \cdot t \\ \mathbf{S}_{k\mathrm{y}} + \mathbf{V}_{(k-1)\mathrm{y}} \cdot t \\ (\mathbf{S}_{k\mathrm{z}} - \mathrm{L}) + \mathbf{V}_{(k-1)\mathrm{z}} \cdot t \end{bmatrix} \tag{3.12}$$

where, $\mathbf{S}_{k\mathrm{x}}, \mathbf{S}_{k\mathrm{y}}, (\mathbf{S}_{k\mathrm{z}} - \mathrm{L})$ are the components of point $\mathbf{P}_k$ and $\mathbf{V}_{(k-1)\mathrm{x}}, \mathbf{V}_{(k-1)\mathrm{y}}, \mathbf{V}_{(k-1)\mathrm{z}}$ are the components of the vector $\mathbf{V}_{k\text{-}1}$ and t is the parameter of the line $\boldsymbol{L}(t)$. Since, the vector $\mathbf{V}_{k\text{-}1}$ lies along the plane perpendicular to the probe axis, the z component is equal to zero. Thus, the above equation can be rewritten as,

$$\boldsymbol{L}(t) = \begin{bmatrix} \mathbf{S}_{k\mathrm{x}} + \mathbf{V}_{(k-1)\mathrm{x}} \cdot t \\ \mathbf{S}_{k\mathrm{y}} + \mathbf{V}_{(k-1)\mathrm{y}} \cdot t \\ (\mathbf{S}_{k\mathrm{z}} - \mathrm{L}) \end{bmatrix} \tag{3.13}$$

The center of the probe surface $\mathbf{C}_k$ lies on this line $\boldsymbol{L}$, thus we have,

$$\mathbf{C}_{k\mathrm{x}} = \mathbf{S}_{k\mathrm{x}} + \mathbf{V}_{(k-1)\mathrm{x}} \cdot t \tag{3.14}$$

$$\mathbf{C}_{k\mathrm{y}} = \mathbf{S}_{k\mathrm{y}} + \mathbf{V}_{(k-1)\mathrm{y}} \cdot t \tag{3.15}$$

$$\mathbf{C}_{k\mathrm{z}} = (\mathbf{S}_{k\mathrm{z}} - \mathrm{L}) \tag{3.16}$$

Substituting it in Equation 3.11, we get,

$$\boldsymbol{S_2}(u_2, v_2, t) = \begin{bmatrix} \mathbf{S}_{k\mathrm{x}} + \mathbf{V}_{(k-1)\mathrm{x}} \cdot t + \boldsymbol{r} \cdot \cos u_2 \cdot \sin v_2 \\ \mathbf{S}_{k\mathrm{y}} + \mathbf{V}_{(k-1)\mathrm{y}} \cdot t + \boldsymbol{r} \cdot \sin u_2 \cdot \sin v_2 \\ (\mathbf{S}_{k\mathrm{z}} - \mathrm{L}) + \boldsymbol{r} \cdot \cos v_2 \end{bmatrix} \tag{3.17}$$

The distance between the points lying on these two surfaces can be computed using the distance formula,

$$\boldsymbol{d} = \sqrt{\begin{matrix} (x(u_1, v_1) - \boldsymbol{r} \cdot \cos u_2 \cdot \sin v_2)^2 + \\ (y(u_1, v_1) - \boldsymbol{r} \cdot \sin u_2 \cdot \sin v_2)^2 + \\ (z(u_1, v_1) - \boldsymbol{r} \cdot \cos v_2)^2 \end{matrix}} \tag{3.18}$$

Now, since the two surfaces are tangent to each other, the distance between theses points at the tangency point is zero. Thus, the optimization problem involves minimizing the distance $\boldsymbol{d}$.

$$\boldsymbol{S_1}(u_1, v_1) - \boldsymbol{S_2}(u_2, v_2, t) = 0 \tag{3.19}$$

Substituting the Equations 3.10 and 3.17 in Equation 3.19 we get,

$$x(u_1, v_1) - \mathbf{S}_{k\mathrm{x}} + \mathbf{V}_{(k-1)\mathrm{x}} \cdot t + \boldsymbol{r} \cdot \cos u_2 \cdot \sin v_2 = 0 \tag{3.20}$$

$$y(u_1, v_1) - \mathbf{S}_{k\mathrm{y}} + \mathbf{V}_{(k-1)\mathrm{y}} \cdot t + \boldsymbol{r} \cdot \sin u_2 \cdot \sin v_2 = 0 \tag{3.21}$$

$$z(u_1, v_1) - (\mathbf{S}_{k\mathrm{z}} - \mathrm{L}) + \boldsymbol{r} \cdot \cos v_2 = 0 \tag{3.22}$$

The inward normal vector $\boldsymbol{n}_{1k(in)}$ to a part surface at any point $\boldsymbol{S_1}(u_1, v_1)$ can be obtained by cross product of its partial derivative by each parameter as,

$$\boldsymbol{n}_{1k(\mathrm{in})} = \frac{\partial \boldsymbol{S_1}(u_1, v_1)}{\partial u_1} \times \frac{\partial \boldsymbol{S_1}(u_1, v_1)}{\partial v_1} \tag{3.23}$$

u_1 and v_1 are the parameters of Surface $\boldsymbol{S_1}$. The corresponding inward unit normal vector $\mathbf{N}_{1k(in)}$ can be obtained as,

$$\mathbf{N}_{1k(\mathrm{in})} = \frac{\boldsymbol{n}_{1k(\mathrm{in})}}{\left\| \boldsymbol{n}_{1k(\mathrm{in})} \right\|} \tag{3.24}$$

where, $\left\| \boldsymbol{n}_{1k(\mathrm{in})} \right\|$ is the magnitude of the vector $\boldsymbol{n}_{1k(\mathrm{in})}$.

Similarly, the outward normal vector $\boldsymbol{n}_{1k(\text{out})}$ to a surface $\boldsymbol{S}_{\mathbf{1}}(u_1, v_1)$ and its unit vector $\mathbf{N}_{1k(\text{out})}$ can be obtained as,

$$\boldsymbol{n}_{1k(\text{out})} = \frac{\partial \boldsymbol{S}_{\mathbf{1}}(u_1, v_1)}{\partial v_1} \times \frac{\partial \boldsymbol{S}_{\mathbf{1}}(u_1, v_1)}{\partial u_1} \tag{3.25}$$

$$\mathbf{N}_{1k(\text{out})} = \frac{\boldsymbol{n}_{1k(\text{out})}}{\left\|\boldsymbol{n}_{1k(\text{out})}\right\|} \tag{3.26}$$

Now, the vector $\mathbf{v}_{\text{k}}$ can be obtained using the $\boldsymbol{n}_{1k(out)}$ as follows,

$$\mathbf{v}_{\text{k}} = \boldsymbol{n}_{1k(\text{out})} - \begin{bmatrix} 0 \\ 0 \\ 1 \end{bmatrix} \cdot \boldsymbol{n}_{1k(\text{out})} \tag{3.27}$$

Also, the unit vector of $\mathbf{v}_k$, $\mathbf{V}_k$ can be obtained as,

$$\mathbf{V}_k = \frac{\mathbf{v}_k}{\|\mathbf{v}_k\|} \tag{3.28}$$

Similarly, the inward normal vector $\boldsymbol{n}_{2k(\text{in})}$ to a probe sphere surface at any point $\boldsymbol{S}_{\mathbf{2}}(u_2, v_2)$ can be obtained by the cross product of its partial derivative by each parameter as,

$$\boldsymbol{n}_{2k(\text{in})} = \frac{\partial \boldsymbol{S}_{\mathbf{2}}(u_2, v_2)}{\partial u_2} \times \frac{\partial \boldsymbol{S}_{\mathbf{2}}(u_2, v_2)}{\partial v_2} \tag{3.29}$$

The normal vectors $\boldsymbol{n}_{1k(\text{out})}$ and $\boldsymbol{n}_{2k(\text{in})}$ of both the surfaces $\boldsymbol{S}_{\mathbf{1}}$ and $\boldsymbol{S}_{\mathbf{2}}$ at the common tangency point are proportionate as shown in Figure 3.13, thus we have the equation,

$$\boldsymbol{n}_{1k(\text{out})}(u_1, v_1) - \lambda \cdot \boldsymbol{n}_{2k(\text{in})}(u_2, v_2, t) = 0 \tag{3.30}$$

where,

λ is a lagrange multiplier,

$\boldsymbol{n}_{1k(\text{out})}$ is an outward normal vector to surface $\boldsymbol{S}_{\mathbf{1}}(u_1, v_1)$ at any subprocess *k*,

$\boldsymbol{n}_{2k(\mathrm{in})}$ is an inward normal vector to surface $\boldsymbol{S_2}(u_2, v_2)$ at any subprocess *k*.

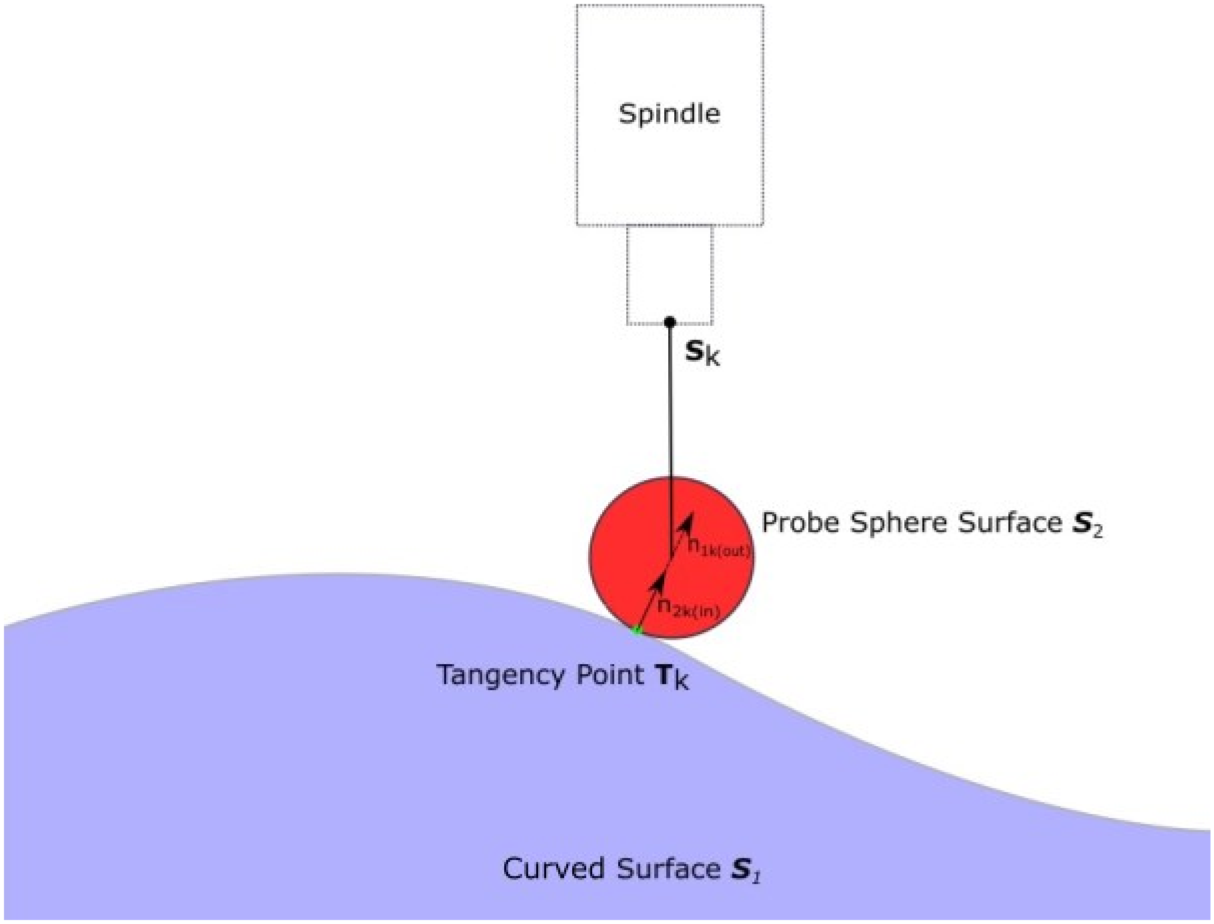

Figure 3.13: Proportionate normal vectors at tangency point

The outward normal vector $\boldsymbol{n}_{1k(\mathrm{out})}$ for surface $\boldsymbol{S}_1(u_1, v_1)$ is computed as,

$$\boldsymbol{n}_{1k(\mathrm{out})}(u_1, v_1) = \begin{bmatrix} -\dfrac{\partial \boldsymbol{y}(u_1, v_1) \cdot \partial \boldsymbol{z}(u_1, v_1)}{\partial v_1 \partial u_1} \\ \dfrac{\partial \boldsymbol{x}(u_1, v_1) \cdot \partial \boldsymbol{z}(u_1, v_1)}{\partial v_1 \partial u_1} \\ -\dfrac{\partial \boldsymbol{y}(u_1, v_1) \cdot \partial \boldsymbol{x}(u_1, v_1)}{\partial v_1 \partial u_1} \end{bmatrix} \tag{3.31}$$

The inward normal vector $\boldsymbol{n}_{2k(\mathrm{in})}$ for surface $\boldsymbol{S}_2(u_2, v_2)$ is computed as,

$$\mathbf{n}_{2k(\text{in})}(u_2, v_2, t) = \begin{bmatrix} -r^2 \cdot \cos u_2 \cdot \sin^2 v_2 \\ -r^2 \cdot \sin u_2 \cdot \sin^2 v_2 \\ -r^2 \cdot \sin v_2 \cdot \cos v_2 \end{bmatrix} \tag{3.32}$$

Substituting $\boldsymbol{n}_{1k(\text{out})}$ and $\boldsymbol{n}_{2k(\text{in})}$ in Equation 3.30 we get,

$$-\frac{\partial \boldsymbol{y}(u_1, v_1) \cdot \partial \boldsymbol{z}(u_1, v_1)}{\partial u_1 \partial v_1} + \lambda \cdot r^2 \cdot \cos u_2 \cdot \sin^2 v_2 = 0 \tag{3.33}$$

$$\frac{\partial \boldsymbol{x}(u_1, v_1) \cdot \partial \boldsymbol{z}(u_1, v_1)}{\partial u_1 \partial v_1} + \lambda \cdot r^2 \cdot \sin u_2 \cdot \sin^2 v_2 = 0 \tag{3.34}$$

$$-\frac{\partial \boldsymbol{y}(u_1, v_1) \cdot \partial \boldsymbol{x}(u_1, v_1)}{\partial u_1 \partial v_1} + \lambda \cdot r^2 \cdot \sin v_2 \cdot \cos v_2 = 0 \tag{3.35}$$

Equations 3.20, 3.21, 3.22 and 3.33, 3.34, 3.35 can be simultaneously solved by using MATLAB to obtain the unknowns $u_1, v_1, u_2, v_2, \lambda, t$. These calculated unknown parameters can then be used to determine the location of the probe tip sphere $\mathbf{C}_k$, the contact point between the probe tip and the part surface $\mathbf{T}_k$ and d_{sk} for each of the subprocesses.

3.4.1 FEA Modeling of Sensing Distance for Curved Surface

To check if the probe is triggered within any subprocess, FEA modeling technique is implemented. First, we construct a force/deflection table using the FEA Model. Specifically, we input a small amount of force to the probe tip along the direction given by the probe approach angles, azimuthal angle $\boldsymbol{\alpha}$, and polar angle $\boldsymbol{\beta}$. If at this point the probe does not trigger, we record the current probing force $\mathbf{F}_\mathrm{p}$ and stylus deflection values. We continue until either the probing force is large enough to trigger the probe or the resultant stylus deflection ds from the FEA model is larger than the one obtained using Equation 3.7. If the probe has triggered in the current subprocess, the resultant stylus deflection ds from the FEA model is considered as the sensing distance d_{sd}. If the probe does not trigger at this subprocess, we continue to the next iteration, where the probing force is directed along the surface normal vector $\mathbf{N}_{k+1}$ and the stylus deflection amount is ds_{k+1}.

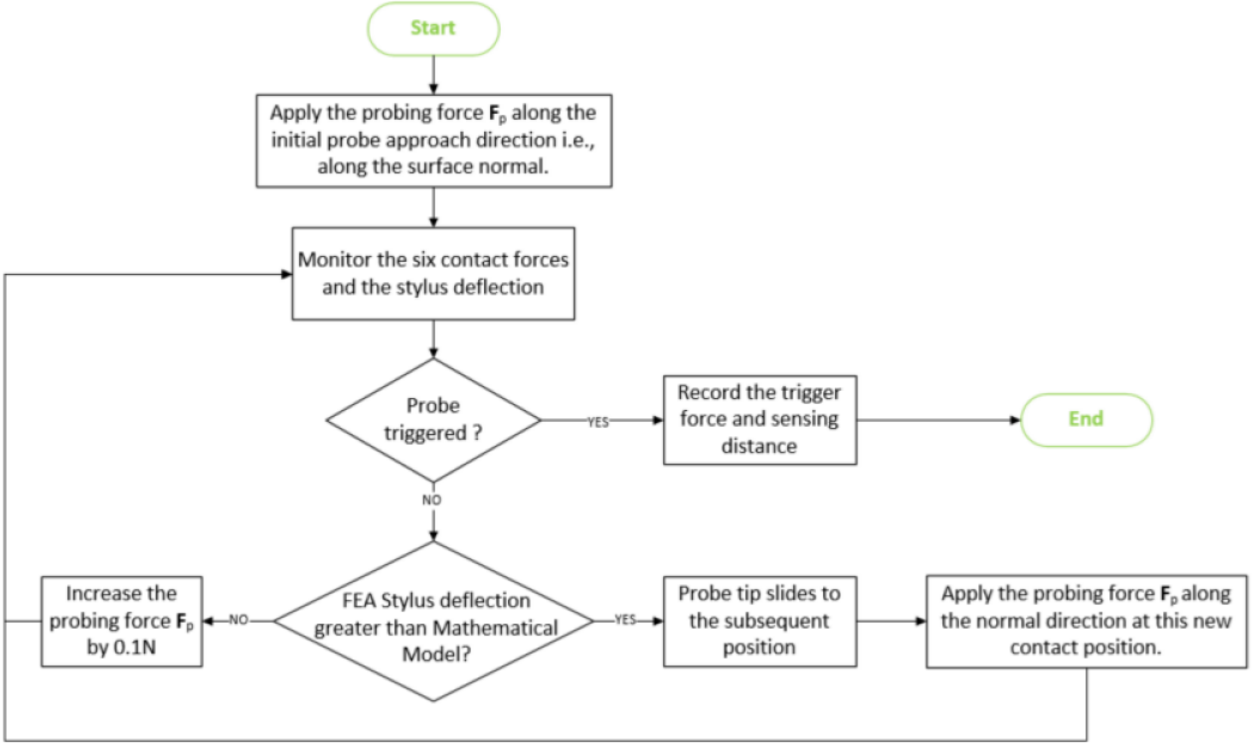

Figure 3.14: Flowchart of curved surface FEA process

3.5 Compensation of Surface Measurement Error

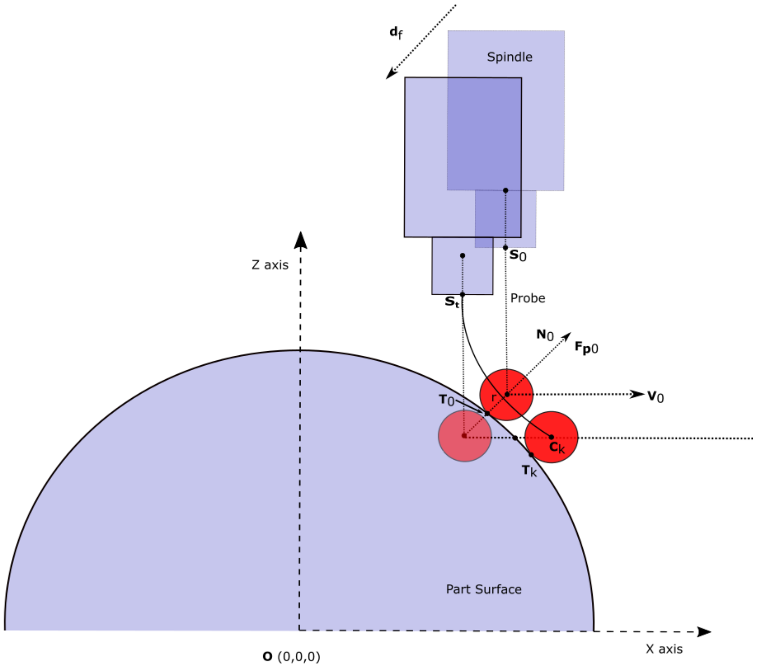

Figure 3.15: Illustration of spindle location ($\mathbf{S}_t$) at triggered instance

As illustrated in Figure 3.15, the probe which is installed on the machine spindle initially touches the part surface, the location of the spindle is $\mathbf{S_0}$. At this stage, the probe is not triggered and continues to feed into the part surface in the direction along the inward surface normal. The probe will continue until it triggers. At this instance, the electronic circuit situated in the probe body will send out a trigger signal to the CNC machine tool to halt the spindle feeding process and back off. Assuming the location of the spindle at the trigger instance as $\mathbf{S_t}$, the coordinate of this position is latched by the CNC machine tool control. Thus, this travel of the spindle from the initial location $\mathbf{S_0}$ to the triggered instance position $\mathbf{S_t}$ along the normal direction of the part surface at a measured point is the error associated with the surface measurement. Also, considering $\boldsymbol{r}$ as the radius of the probe tip sphere, it needs to be compensated as well. Thus, the error can be compensated as,

$$\mathbf{T}_0 = \mathbf{S_t} + (\boldsymbol{r} - k \cdot \mathrm{d_f}) \cdot \mathbf{N}_{\mathbf{0}(\boldsymbol{in})} \tag{3.36}$$

where,

k = Number of subprocess at the trigger instance,

$\mathrm{d_f}$ = Feed amount along initial surface normal in mm,

$\boldsymbol{r}$ = Radius of the probe tip sphere in mm,

$\mathbf{T}_0$ = Target point on the part surface to be measured,

$\mathbf{N}_{\mathbf{0}(\boldsymbol{in})}$ = Unit inward surface normal to part surface at point $\mathbf{T}_0$,

$\mathbf{S_t}$ = Position of spindle at probe triggered instance.

Chapter 4: Results and Discussions

4.1 Introduction

This chapter discusses the results of the surface measurements in the case of the vertical surface, inclined surface, and curved surface. In order to speed up the FEA simulation, a golden section search algorithm is implemented for vertical and inclined surface measurement, which is discussed in brief. Next, the proposed mathematical model for curved surface measurement considering the sliding effects and without simplifying the probe geometry is verified against the experimental results. In addition to that, vertical surface measurement results are examined. Furthermore, two case studies are discussed as follows,

1. Inclined surface measurement results are compared with the existing mathematical model,
2. Ellipsoidal and Inclined surface, the two forms of surfaces are studied to estimate the sliding effects of these two surfaces with varying surface curvatures. Sliding of the probe in case of the convex surface is discussed.

4.2 Golden Section Search Algorithm

Golden section search algorithm is used to find the minimum (or maximum) of a function. It is assumed that the function has a minimum (or maximum) lying between two points, which can be then searched for iteratively [26]. The implementation of this method in ANSYS script is discussed below.

4.2.1 Implementation of Golden Section Search Algorithm

Step 1: Choose a lower bound and an upper bound value. In this case, the lower bound will be 0 N while the upper bound will be 5 N. Upper bound is chosen such that, the trigger force must not exceed the upper bound value as shown in Figure 4.1.

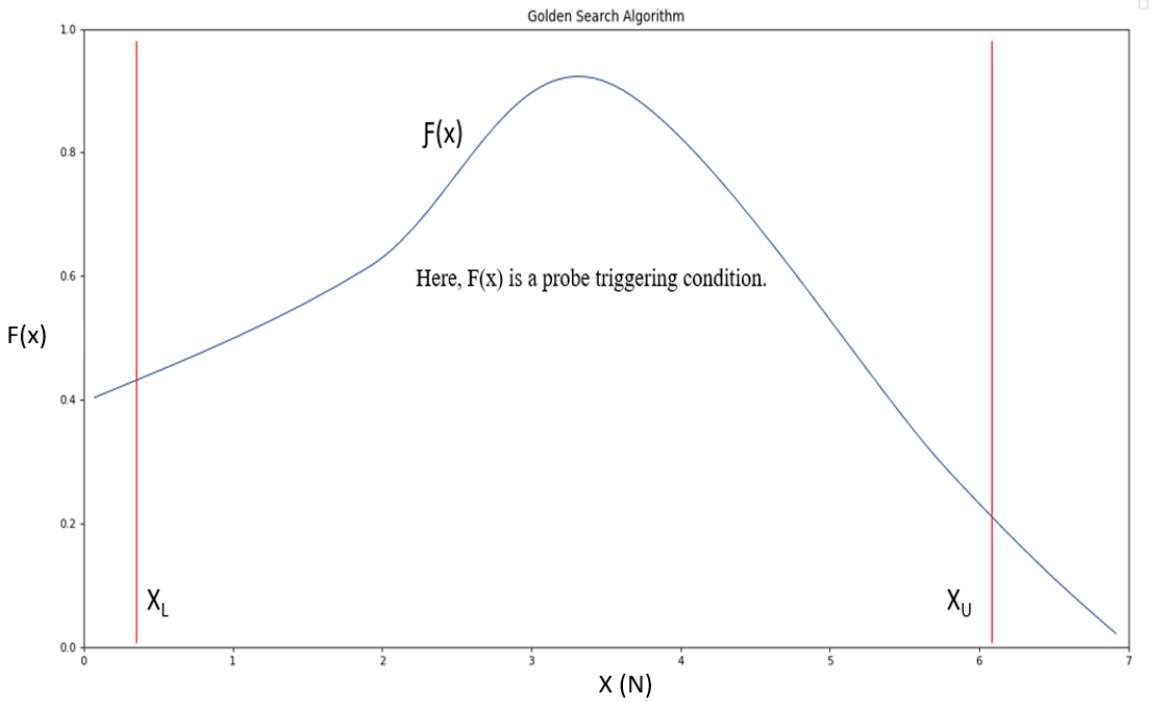

Figure 4.1: Setting upper (X_U) and lower (X_L) bounds

Step 2: Calculate the Golden ratio R which is equal to $\frac{\sqrt{5}-1}{2}$ and is approximately equal to 0.6180.

Calculate the distance d, given by $d = R\ (X_U - X_L)$

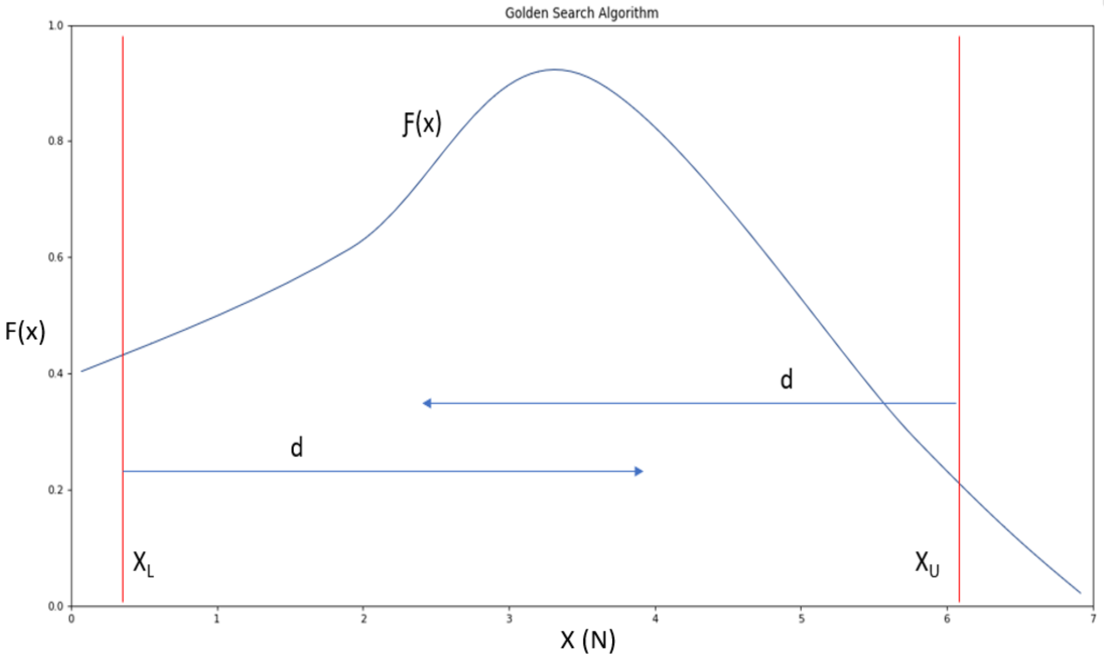

Figure 4.2: Adding ‘d’ to lower bound and subtracting ‘d’ from upper bound

Step 3: Calculate the special intermediate points X_1 and X_2, given by $X_1 = X_U - d$, $X_2 = X_L + d$. Now, find the function at these two special points. Figure 4.3 shows intermediate points X_1 and X_2.

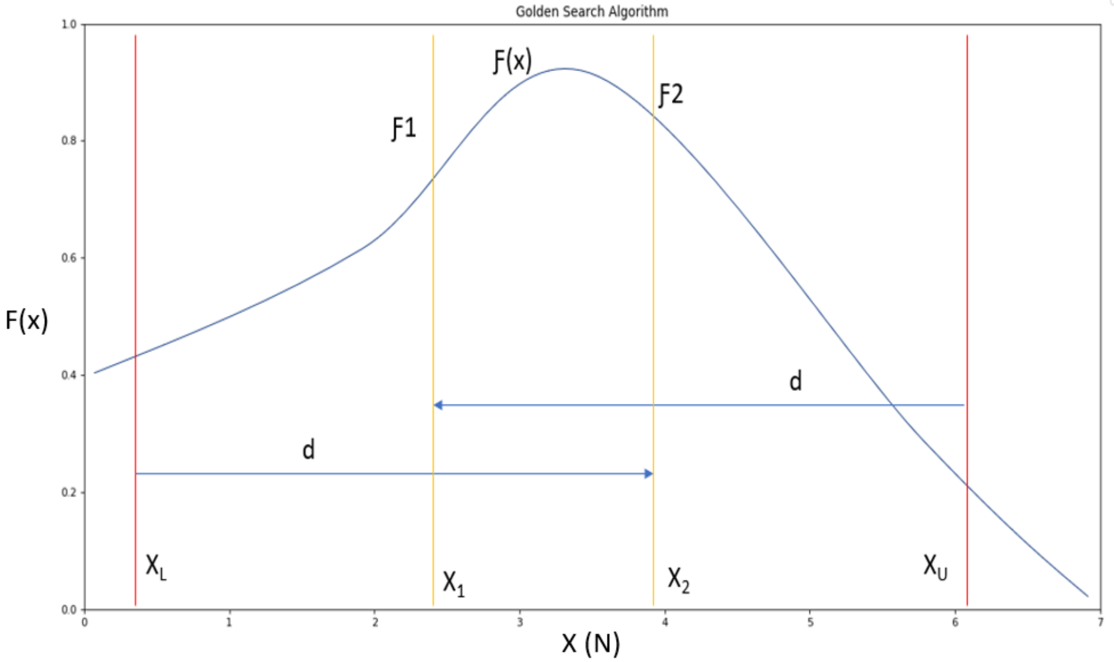

Figure 4.3: Intermediate points X_1 and X_2

Once the function is evaluated at these intermediate points, there is a possibility of four cases. i.e., the next iterations will depend on either one of these four cases, which are as follows,

Case 1: *Probe triggers at point* X_1

Search area will be reduced to that shown in the Figure 4.4. Where, the lower bound will remain the same, while the upper bound will be equal to X_1.

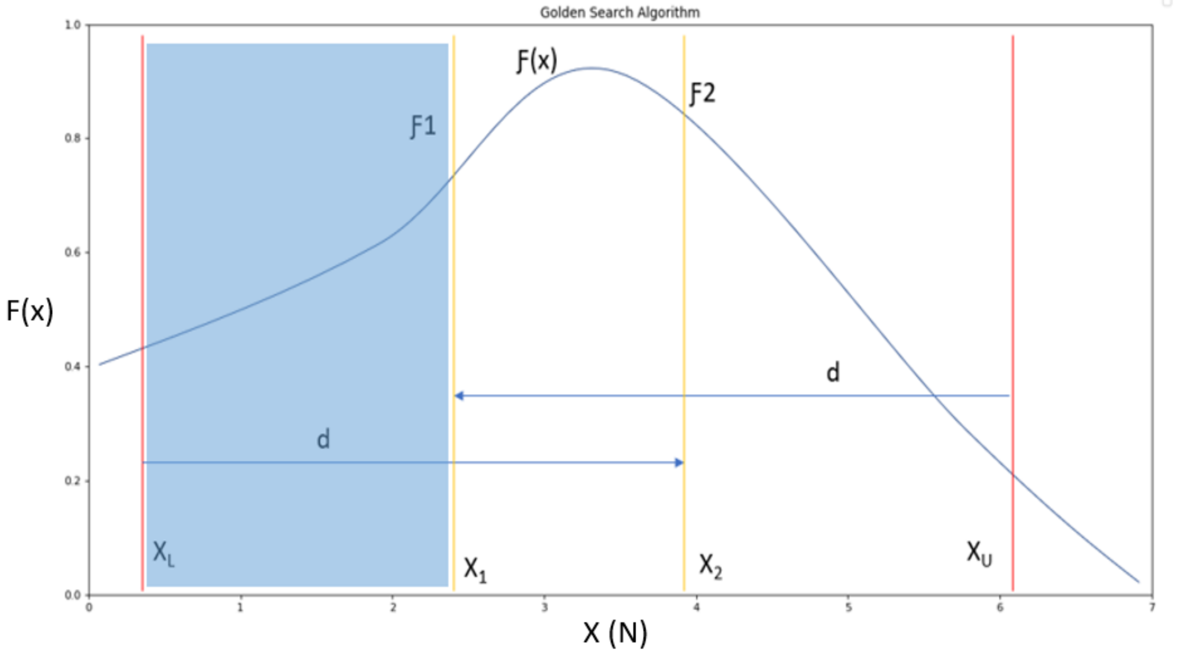

Figure 4.4: Search area reduced between upper bound and X_1

Case 2: *Probe triggers at point* X_2

Search area will be reduced to that shown in the Figure 4.5. Where, the upper bound will remain the same, while the lower bound will be equal to X_2.

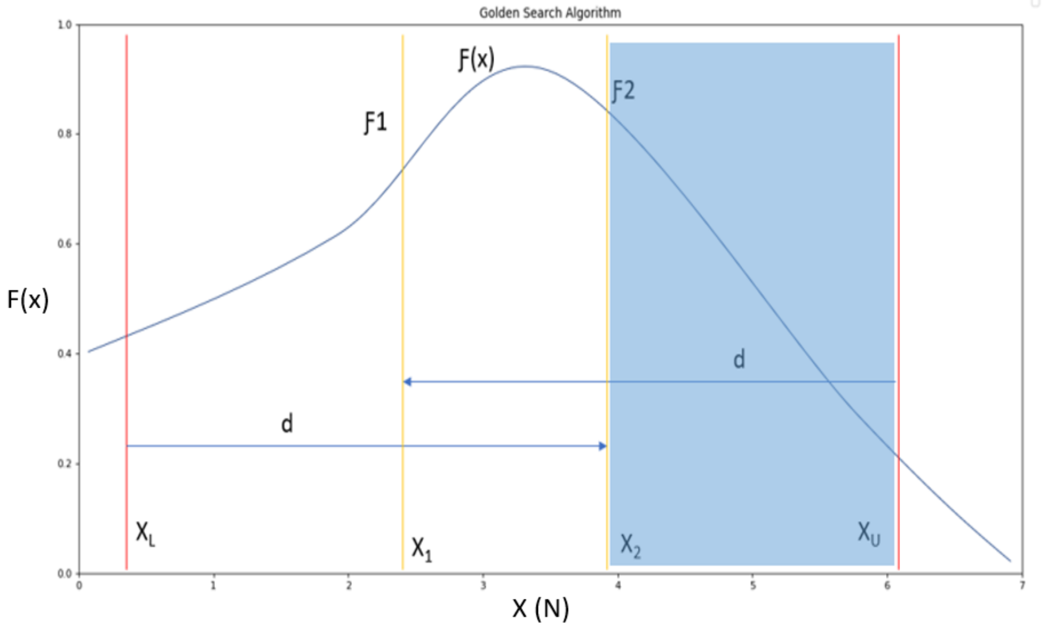

Figure 4.5:Search area reduced between X_2 and upper bound

Case 3: *Probe triggers at point X_2 but not at point X_1*

Search area will be reduced to that shown in the Figure 4.6. Where, the upper bound will be equal to X_2, while the lower bound will be equal to X_1.

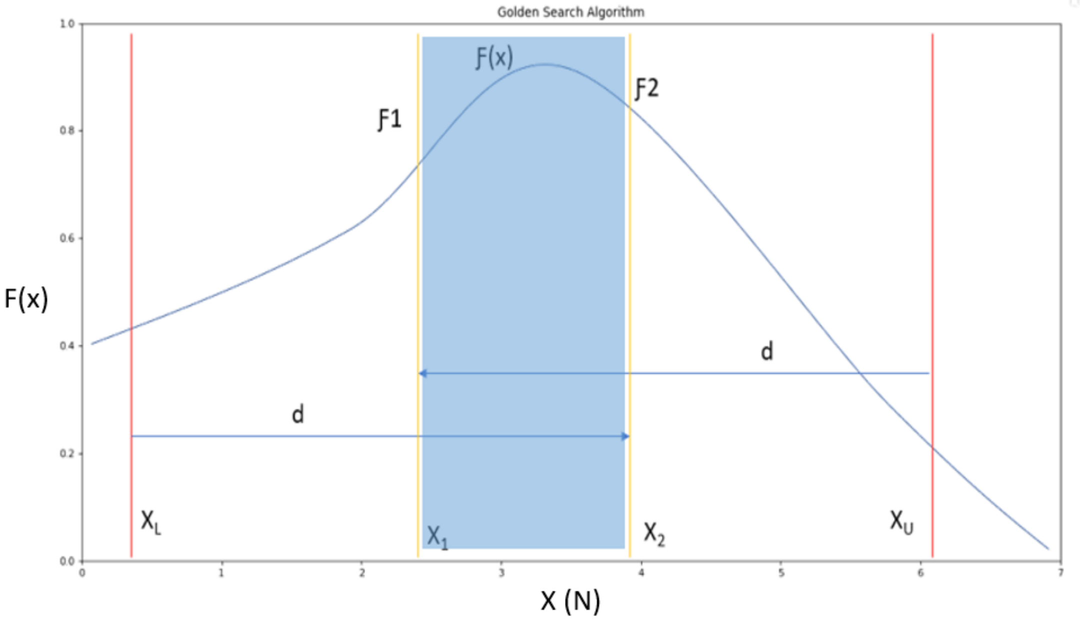

Figure 4.6: Search area reduced between X_1 and X_2

Case 4: *Probe triggers at point* X_1 *but not at point* X_2

This case is not possible due to the reason that the probe triggered at lower force value i.e., point X_1 must be in triggered state at point X_2.

4.3 Vertical Surface Simulation Results

Simulation results were obtained for a range of azimuthal angles from 0 to 350 degrees with a step of 10 degrees. The displacement was applied for each azimuthal angle utilizing the ANSYS script until the triggering condition of the probe was achieved. The displacement and corresponding probing force were observed. Figure 4.7 (a) illustrates the trigger force plot across the azimuthal angle range. As the touch trigger probe is based on a three-lobed design, the trigger forces and sensing distance should be symmetrical about 120 degrees. It was observed that there is a small deviation between the results, which is due to the discretization error of the FEA model. However, it can be noted that this deviation is less than 1 micron. It was also observed that the triggering force values were at the highest at angles 60, 180, and 300 degrees indicating the high force directions, while they were at the lowest at angles 0, 120, and 240 degrees indicating the low force directions.

Table 4.1: Sensing distance comparison between proposed method and existing method for vertical surface measurement

Azimuthal Angle (degrees)	**Trigger Force (N)**		**Sensing distance (mm)**		**Error (mm)**
	Proposed Method	**Existing Method**	**Proposed Method**	**Existing Method**	
0	0.75	0.96	0.0034	0.0047	0.0013
10	0.74	0.95	0.0034	0.0048	0.0014
20	0.76	0.97	0.0035	0.0049	0.0014
30	0.80	1.02	0.0037	0.0051	0.0014

40	0.88	1.10	0.0041	0.0055	0.0014
50	1.01	1.25	0.0046	0.0063	0.0017
60	1.22	1.50	0.0056	0.0075	0.0019

Due to the symmetric structure of the kinematic probes, there is only a necessity to compare the results of azimuthal angles ranging from 0 to 60 degrees as shown in Table 4.1. The sensing distance in the case of the existing method is larger than the proposed method, this is due to the fact that the existing method oversimplifies the probe model by considering uniform cross-section with single material of the stylus stem rather than the standard existing ones with varying cross-sections and made of composite materials. This leads to a reduction in the moment of inertia thereby increasing the bending of the stylus stem and subsequently increasing the sensing distance. The error between these values is more than 1 micron and thus cannot be neglected. Hence, the proposed method is accurate than the existing mathematical model in finding the sensing distance.

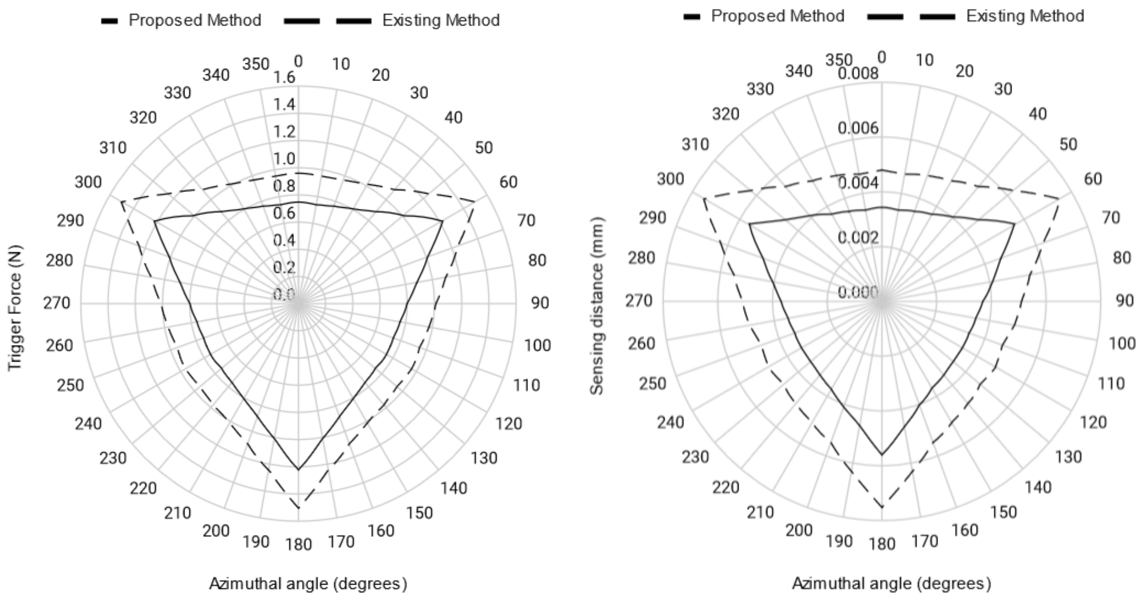

Figure 4.7: Trigger force and sensing distance plot for vertical surface

4.4 Case Study I: Inclined Surface Proposed and Existing Method Results

Simulation results were obtained for a range of azimuthal angles from 0 to 350 degrees with a step of 10 degrees for each polar angle from 10 to 80 degrees with an interval of 10 degrees. The probing force was applied for each azimuthal angle utilizing the ANSYS script until the triggering condition of the probe was reached. The triggering force and corresponding sensing distance was observed. As the touch trigger probe is based on a three lobed design, the trigger forces and sensing distance should be symmetrical about 120 degrees. It was observed that there is a small deviation between the results, which is due to the discretization error of the FEA model. However, it can be noted that this deviation is less than a micron. It was also observed that the triggering force values were highest at angles 60, 180 and 300 degrees indicating the high force directions, while they were lowest at angles 0, 120 and 240 degrees indicating the low force directions, which follows a similar trend as in the case of flat vertical surface.

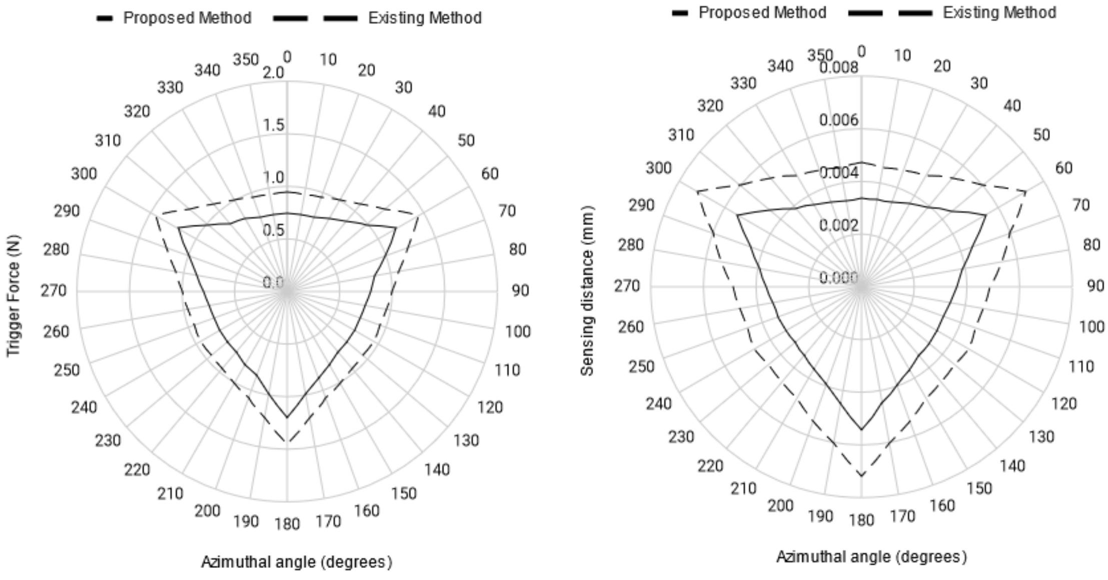

Figure 4.8: Trigger force and Sensing distance plot for 80-degree polar angle

Table 4.2: Sensing distance comparison between proposed and existing method for 80º Polar angle

Polar Angle (degrees)	Azimuthal Angle (degrees)	Trigger Force (N)		Sensing distance (mm)		Error (mm)
		Proposed Method	Existing Method	Proposed Method	Existing Method	
80	0	0.74	0.95	0.0033	0.0047	0.0014
	10	0.74	0.94	0.0033	0.0046	0.0013
	20	0.75	0.96	0.0034	0.0047	0.0013
	30	0.80	1.00	0.0036	0.0049	0.0013
	40	0.87	1.09	0.0039	0.0054	0.0015
	50	0.99	1.22	0.0045	0.0060	0.0015
	60	1.2	1.45	0.0054	0.0072	0.0018

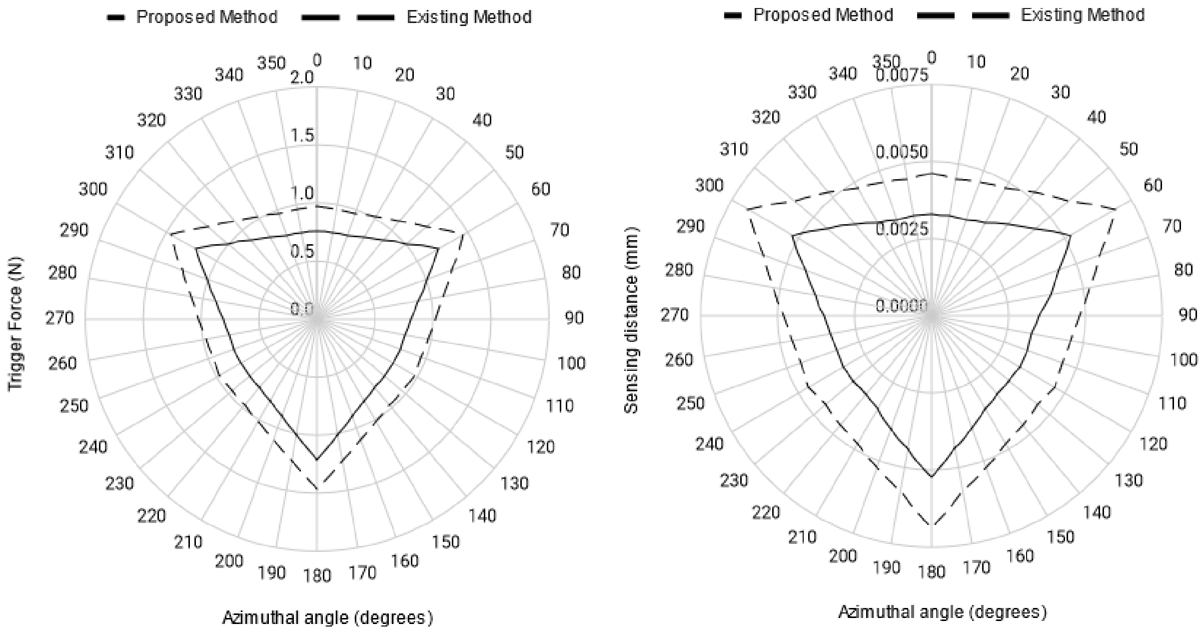

Figure 4.9: Trigger force and Sensing distance plot for 70-degree polar angle

Table 4.3: Sensing distance comparison between proposed and existing method for 70º Polar angle

Polar Angle (degrees)	**Azimuthal Angle (degrees)**	**Trigger Force (N)**		**Sensing distance (mm)**		**Error (mm)**
		Proposed Method	**Existing Method**	**Proposed Method**	**Existing Method**	
70	0	0.76	0.97	0.0033	0.0046	0.0013
	10	0.76	0.96	0.0033	0.0045	0.0012
	20	0.77	0.97	0.0033	0.0046	0.0013
	30	0.81	1.02	0.0035	0.0048	0.0013
	40	0.89	1.10	0.0039	0.0052	0.0013
	50	1.01	1.24	0.0044	0.0058	0.0014
	60	1.21	1.46	0.0052	0.0069	0.0017

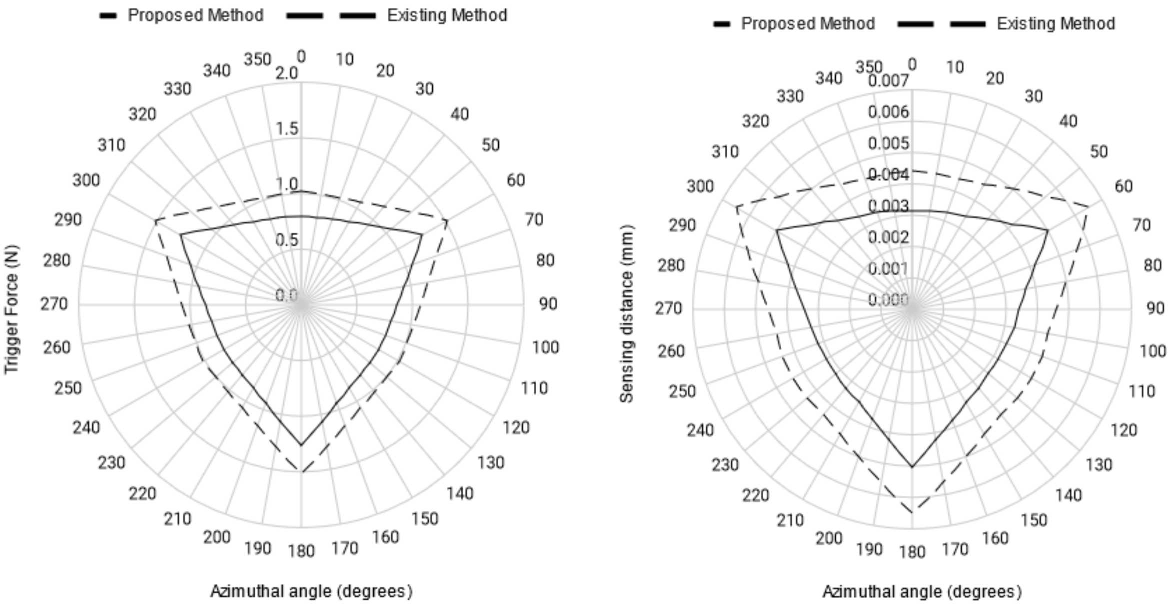

Figure 4.10: Trigger force and Sensing distance plot for 60-degree polar angle

Table 4.4: Sensing distance comparison between proposed and existing method for 60º Polar angle

Polar Angle (degrees)	Azimuthal Angle (degrees)	Trigger Force (N)		Sensing distance (mm)		Error (mm)
		Proposed Method	Existing Method	Proposed Method	Existing Method	
60	0	0.8	1.02	0.0031	0.0044	0.0013
	10	0.8	1.01	0.0032	0.0044	0.0012
	20	0.82	1.02	0.0033	0.0044	0.0011
	30	0.86	1.07	0.0034	0.0046	0.0012
	40	0.94	1.15	0.0037	0.0050	0.0013
	50	1.06	1.29	0.0042	0.0056	0.0014
	60	1.26	1.51	0.0050	0.0065	0.0015

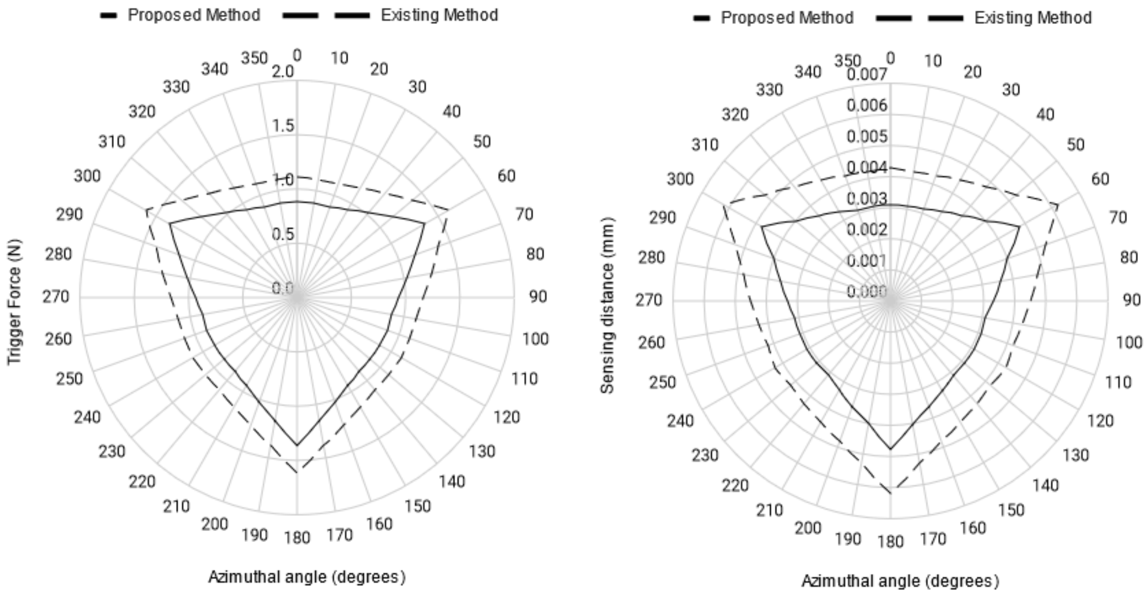

Figure 4.11: Trigger force and Sensing distance plot for 50-degree polar angle

Table 4.5: Sensing distance comparison between proposed and existing method for 50º Polar angle

Polar Angle (degrees)	Azimuthal Angle (degrees)	Trigger Force (N)		Sensing distance (mm)		Error (mm)
		Proposed Method	**Existing Method**	**Proposed Method**	**Existing Method**	
50	0	0.88	1.11	0.0031	0.0043	0.0012
	10	0.88	1.09	0.0031	0.0042	0.0011
	20	0.89	1.11	0.0031	0.0043	0.0012
	30	0.94	1.16	0.0033	0.0045	0.0012
	40	1.02	1.25	0.0036	0.0048	0.0012
	50	1.15	1.39	0.0040	0.0053	0.0013
	60	1.36	1.61	0.0048	0.0062	0.0014

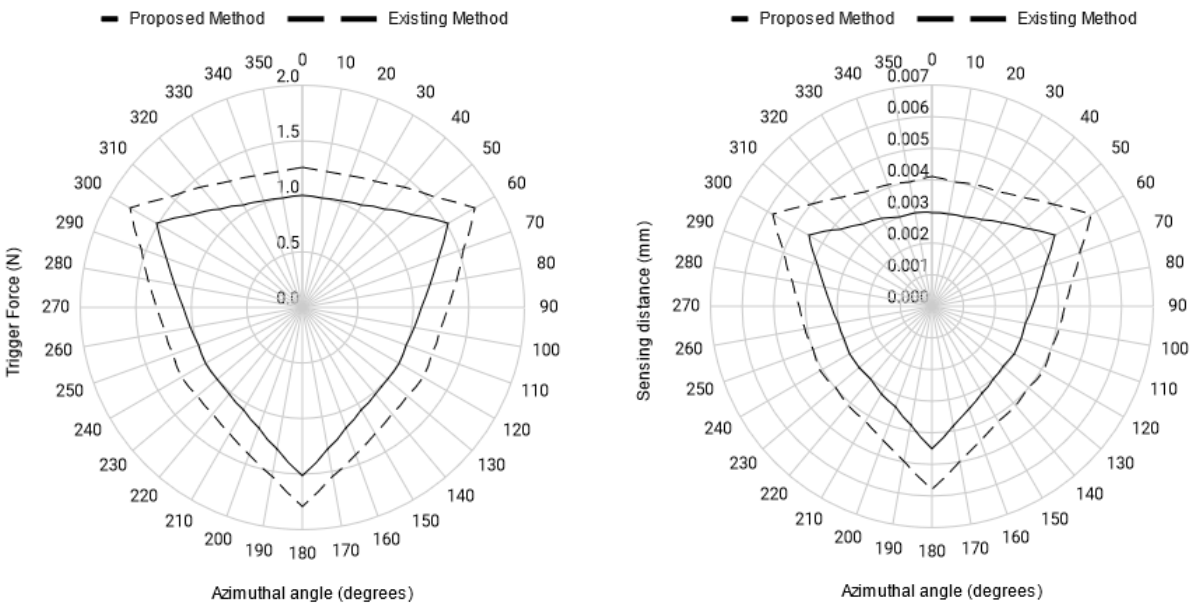

Figure 4.12: Trigger force and Sensing distance plot for 40-degree polar angle

Table 4.6: Sensing distance comparison between proposed and existing method for 40º Polar angle

Polar Angle (degrees)	Azimuthal Angle (degrees)	Trigger Force (N)		Sensing distance (mm)		Error (mm)
		Proposed Method	**Existing Method**	**Proposed Method**	**Existing Method**	
	0	1.01	1.26	0.0030	0.0041	0.0011
	10	1.00	1.24	0.0030	0.004	0.0010
	20	1.02	1.26	0.0030	0.0041	0.0011
40	30	1.07	1.31	0.0032	0.0042	0.0010
	40	1.16	1.41	0.0034	0.0045	0.0011
	50	1.30	1.44	0.0038	0.0050	0.0012
	60	1.52	1.79	0.0045	0.0058	0.0013

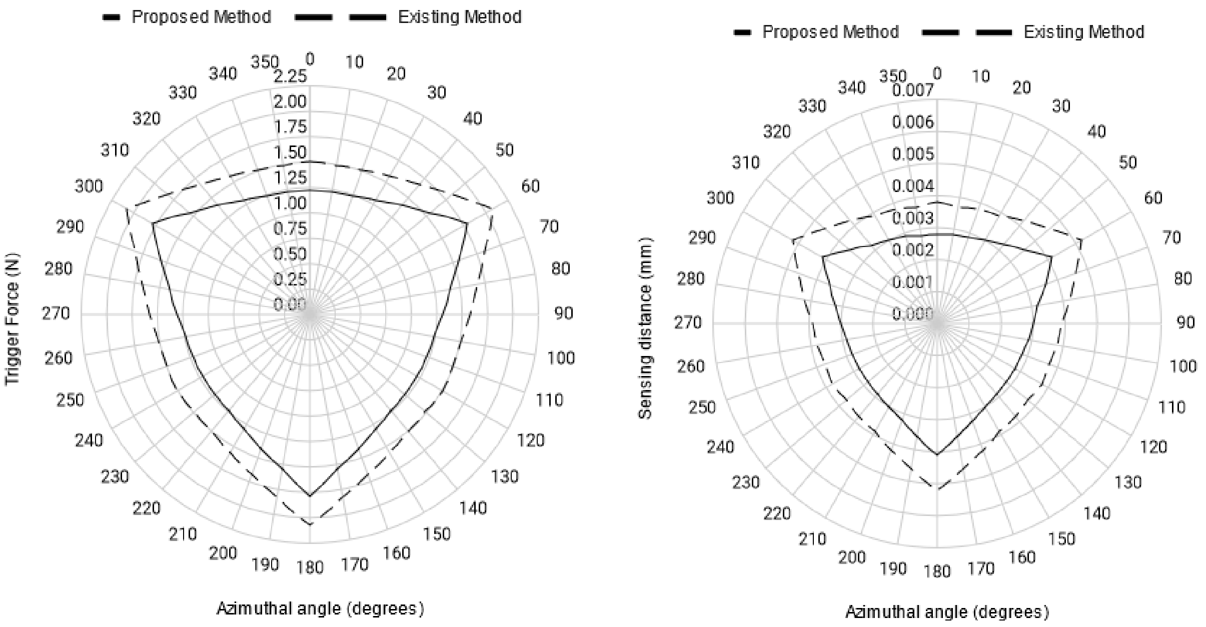

Figure 4.13: Trigger force and Sensing distance plot for 30-degree polar angle

Table 4.7: Sensing distance comparison between proposed and existing method for 30º Polar angle

Polar Angle (degrees)	Azimuthal Angle (degrees)	Trigger Force (N)		Sensing distance (mm)		Error (mm)
		Proposed Method	Existing Method	Proposed Method	Existing Method	
30	0	1.22	1.51	0.0028	0.0038	0.001
	10	1.22	1.49	0.0028	0.0037	0.0009
	20	1.24	1.51	0.0029	0.0038	0.0009
	30	1.30	1.56	0.0030	0.0039	0.0009
	40	1.40	1.67	0.0032	0.0042	0.001
	50	1.55	1.83	0.0036	0.0046	0.001
	60	1.79	2.08	0.0041	0.0052	0.0011

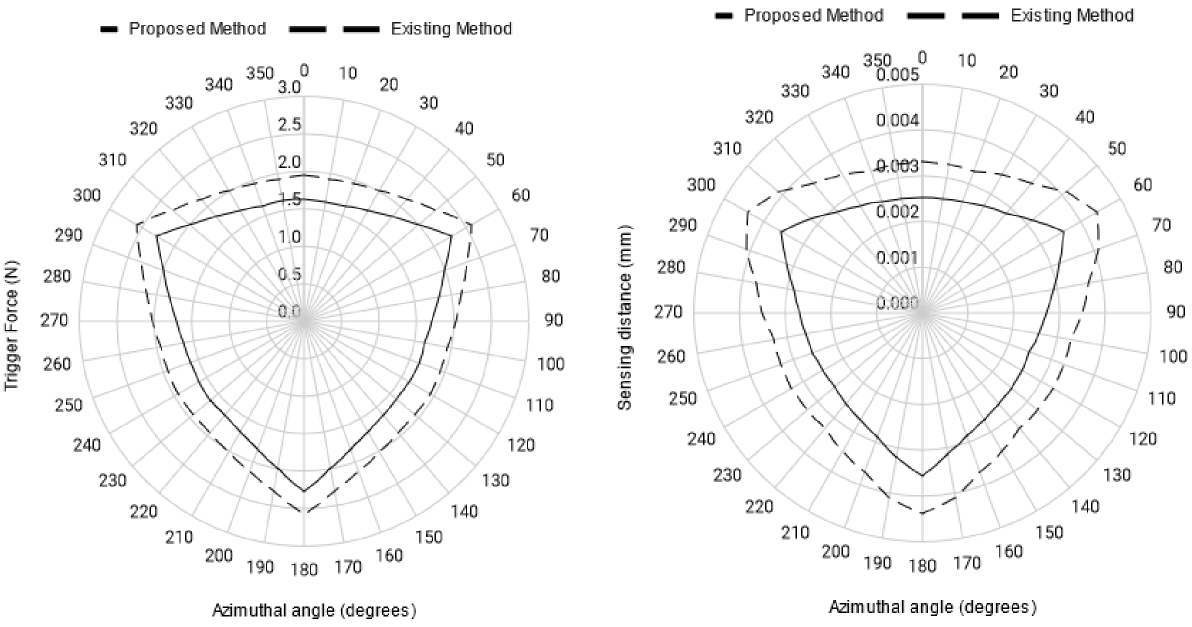

Figure 4.14: Trigger force and Sensing distance plot for 20-degree polar angle

Table 4.8: Sensing distance comparison between proposed and existing method for 20º Polar angle

Polar Angle (degrees)	Azimuthal Angle (degrees)	Trigger Force (N)		Sensing distance (mm)		Error (mm)
		Proposed Method	Existing Method	Proposed Method	Existing Method	
20	0	1.62	1.95	0.0025	0.0033	0.0008
	10	1.61	1.93	0.0025	0.0033	0.0008
	20	1.64	1.95	0.0026	0.0033	0.0007
	30	1.70	2.02	0.0027	0.0035	0.0008
	40	1.82	2.12	0.0029	0.0037	0.0008
	50	2.00	2.31	0.0032	0.0041	0.0009
	60	2.27	2.58	0.0036	0.0044	0.0008

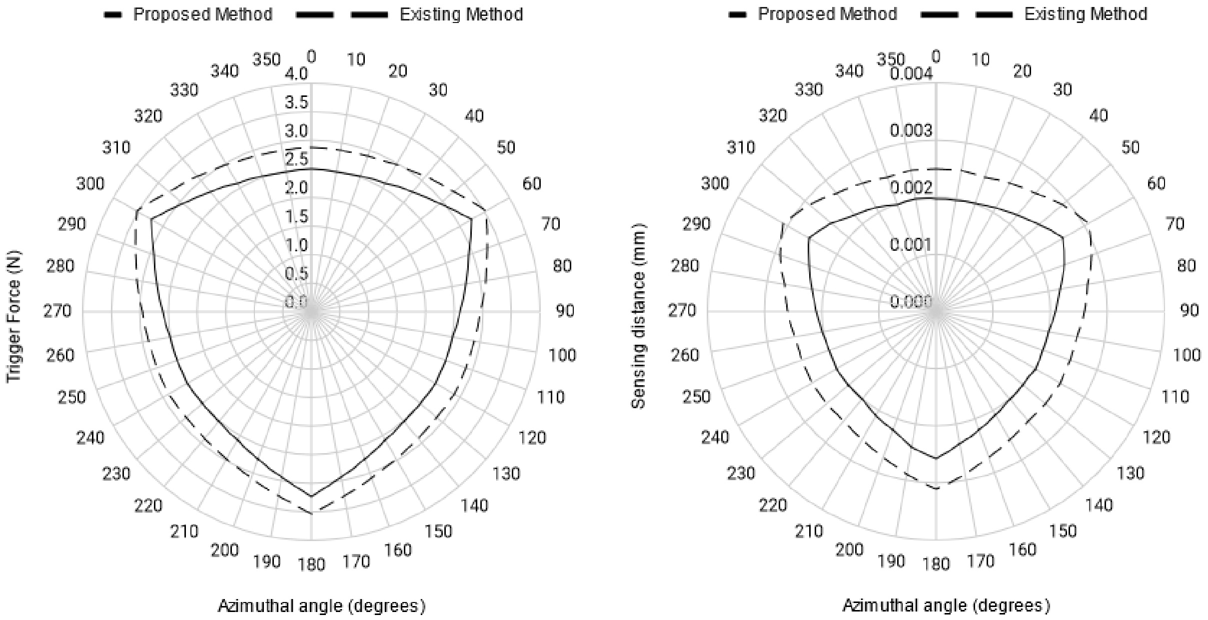

Figure 4.15: Trigger force and Sensing distance plot for 10-degree polar angle

Table 4.9: Sensing distance comparison between proposed and existing method for 10º Polar angle

Polar Angle (degrees)	**Azimuthal Angle (degrees)**	**Trigger Force (N)**		**Sensing distance (mm)**		**Error (mm)**
		Proposed Method	**Existing Method**	**Proposed Method**	**Existing Method**	
10	0	2.50	2.89	0.0020	0.0025	0.0005
	10	2.49	2.87	0.0020	0.0025	0.0005
	20	2.52	2.89	0.0020	0.0025	0.0005
	30	2.60	2.96	0.0021	0.0026	0.0005
	40	2.74	3.09	0.0022	0.0027	0.0005
	50	2.94	3.27	0.0024	0.0029	0.0005
	60	3.23	3.54	0.0026	0.0032	0.0006

As seen from the above results comparison between the proposed method and existing method for inclined surface measurement, it is noted that the error is greater than 1 micron and thus it is not feasible to implement the existing method in determining the sensing distance. The authors have completely disregarded the displacement along the probe axis and have assumed the bending as the prominent source of the sensing distance error. Also, as discussed in chapter 2, the authors have assumed the probe model as a cantilever beam. Figure 4.16 shows the comparison between the sensing distance results from the FEA simulation model and the existing method for each azimuthal angle from 0 to 350 degrees and for each polar angle from 10-80 degrees. It can be observed that the sensing distance reduces as the polar angle reduces. It is maximum at around 80 degrees polar angle and minimum at 10 degrees polar angle. The error associated between these two methods is less, but greater than 1 micron and is significant enough in the measurement process.

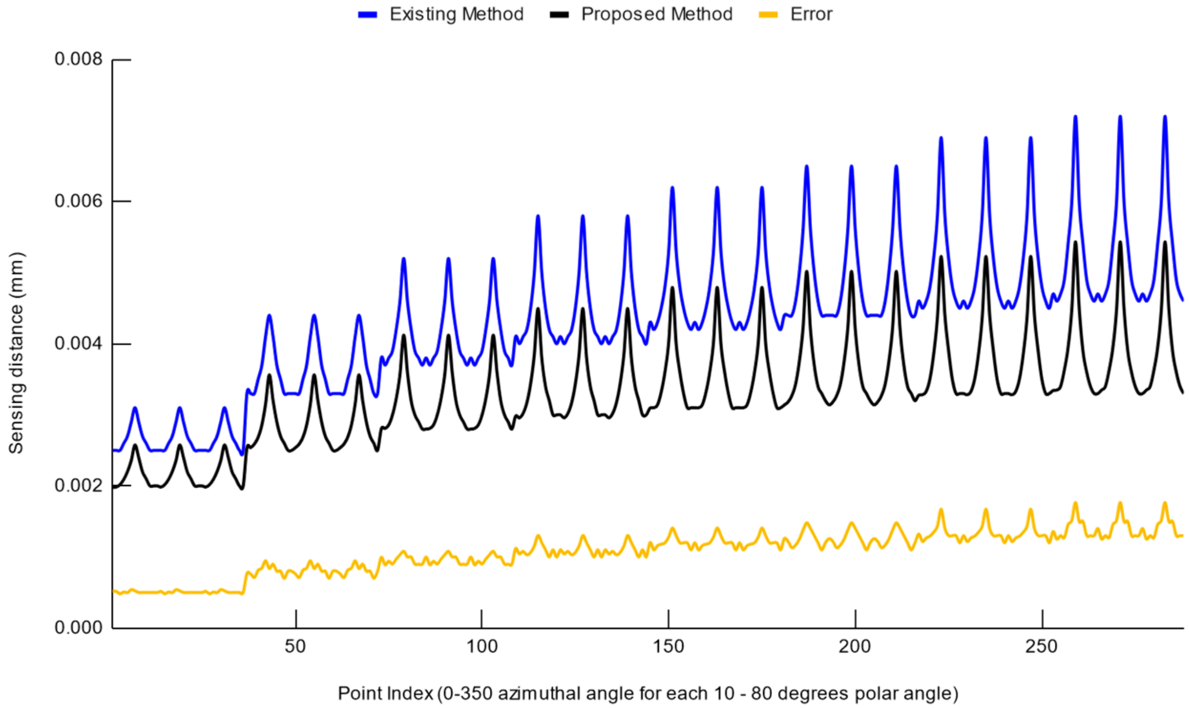

Figure 4.16: Sensing distance at each azimuthal angle for polar angles 10-80 degrees

Error between these two methods seems to be less due to the probe parameters. Modifying the probe parameters may increase the errors associated with the existing method.

4.5 Case Study II: Curved Surfaces Examples and Effects of Curvature on Sensing Distance

4.5.1 Curved Surface Example I: Convex Surface

The convex surface $\boldsymbol{S_1}$ as demonstrated in the Figure 4.17 can be parametrically defined as,

$$\boldsymbol{S_1}(u_1, v_1) = \begin{bmatrix} \mathbf{a} \cdot u_1 \\ \mathbf{b} \cdot u_1 \\ -\mathbf{b} \cdot ({u_1}^2 + {v_1}^2) \end{bmatrix}, \tag{4.1}$$

$$-1 \le u_1 \le 1,$$

$$-1 \le v_1 \le 1.$$

where, u_1 and v_1 are the parameters of convex surface $\boldsymbol{S_1}$.

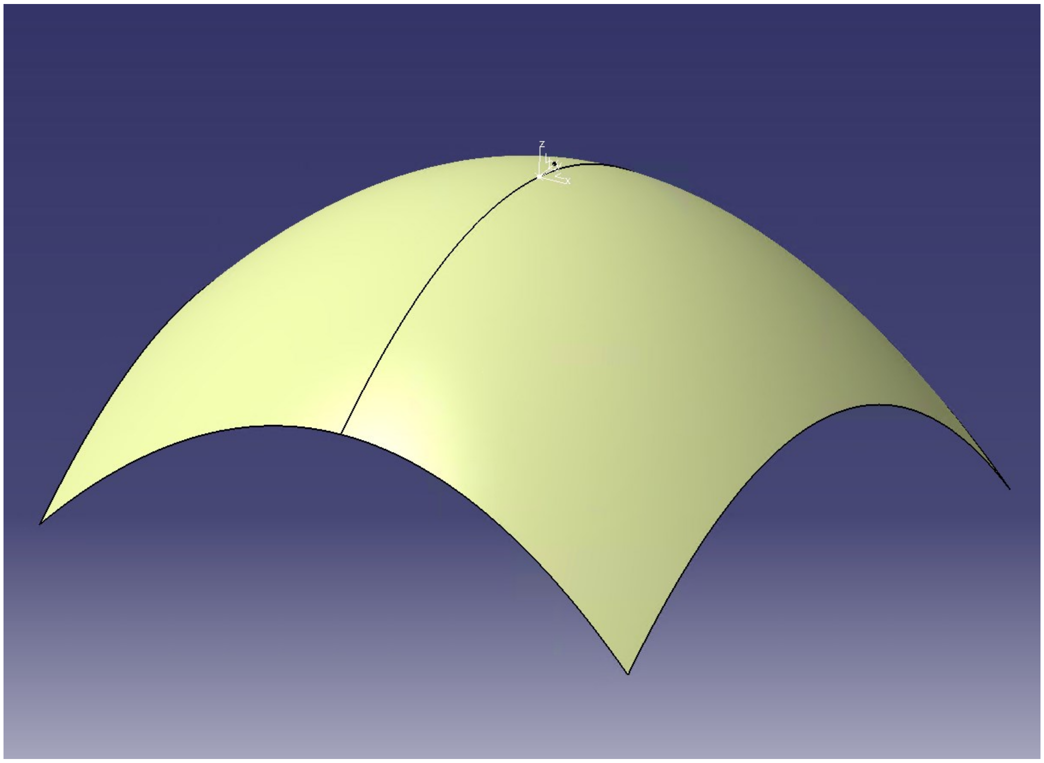

Figure 4.17: Convex surface

Although the convex surface $\boldsymbol{S_1}$ has some significant curvature than the ellipsoidal surface, the probe sphere tip on this surface tends to slide only in one plane throughout the sliding course. Thus, there is a need of modifying this convex surface such that the probe tip can slide in distinct planes simultaneously. This can be achieved by rotating the existing convex surface $\boldsymbol{S_1}$ along an arbitrary axis other than the x, y, and z axes. The arbitrary axis is chosen such that it lies in the zx plane at an angle of 45 degrees to x-axis. The surface is then rotated along this axis at an angle of 70 degrees. This transformation of the surface can be achieved by the following equation,

$$\boldsymbol{S_1}^{\mathbf{T}} = \mathbf{R_y}^{\mathbf{CCW}} \cdot \mathbf{R_z}^{\mathbf{CCW}} \cdot \mathbf{R_y}^{\mathbf{CW}} \cdot \boldsymbol{S_1} \tag{4.2}$$

where,

$$\mathbf{R_y}^{\mathbf{CCW}} = \begin{bmatrix} \cos(45^\circ) & 0 & \sin(45^\circ) & 0 \\ 0 & 1 & 0 & 0 \\ -\sin(45^\circ) & 0 & \cos(45^\circ) & 0 \\ 0 & 0 & 0 & 1 \end{bmatrix},$$

$$\mathbf{R_z}^{\mathbf{CCW}} = \begin{bmatrix} \cos(70^\circ) & -\sin(70^\circ) & 0 & 0 \\ \sin(70^\circ) & \cos(70^\circ) & 0 & 0 \\ 0 & 0 & 1 & 0 \\ 0 & 0 & 0 & 1 \end{bmatrix},$$

$$\mathbf{R_y}^{\mathbf{CW}} = \begin{bmatrix} \cos(-45^\circ) & 0 & \sin(-45^\circ) & 0 \\ 0 & 1 & 0 & 0 \\ -\sin(-45^\circ) & 0 & \cos(-45^\circ) & 0 \\ 0 & 0 & 0 & 1 \end{bmatrix}.$$

The new transformed surface as shown in Figure 4.18 can now parametrically be defined as,

$$\boldsymbol{S_1}^{\mathbf{T}} = \begin{bmatrix} 0.8535 \cdot \mathrm{a} \cdot u_1 - 0.5 \cdot \mathrm{a} \cdot v_1 - 0.464 \cdot \mathrm{b} \cdot (u_1{}^2 + v_1{}^2) \\ 0.5 \cdot \mathrm{a} \cdot u_1 + 0.7071 \cdot \mathrm{a} \cdot v_1 + 0.5 \cdot \mathrm{b} \cdot (u_1{}^2 + v_1{}^2) \\ 0.1464 \cdot \mathrm{a} \cdot u_1 + 0.5 \cdot \mathrm{a} \cdot v_1 - 0.8535 \cdot \mathrm{b} \cdot (u_1{}^2 + v_1{}^2) \end{bmatrix} \qquad (4.3)$$

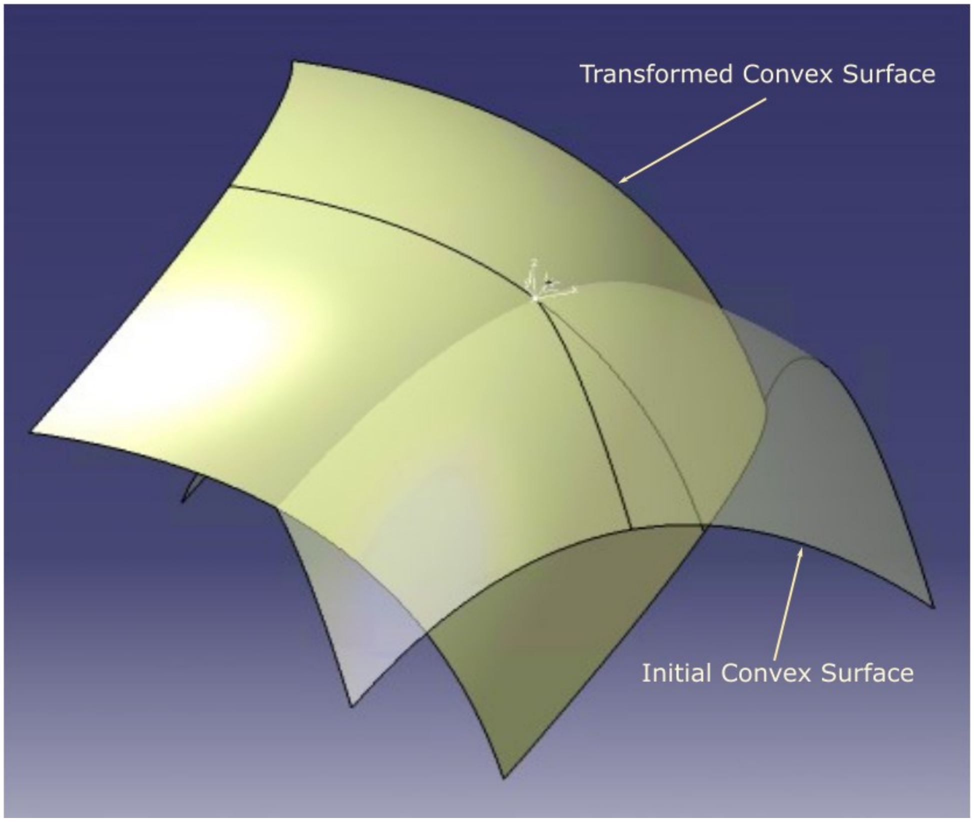

Figure 4.18: Transformed convex surface

Substituting Equation 4.3 and 3.17 in Equation 3.19, we get,

$$0.8535 \cdot \mathrm{a} \cdot u_1 - 0.5 \cdot \mathrm{a} \cdot v_1 - 0.464 \cdot \mathrm{b} \cdot ({u_1}^2 + {v_1}^2) - \mathbf{S}_{k\mathrm{x}} + \mathbf{V}_{(k-1)\mathrm{x}} \cdot t + \boldsymbol{r} \cdot \cos u_2 \cdot \sin v_2 = 0 \tag{4.4}$$

$$0.5 \cdot \mathrm{a} \cdot u_1 + 0.7071 \cdot \mathrm{a} \cdot v_1 + 0.5 \cdot \mathrm{b} \cdot ({u_1}^2 + {v_1}^2) - \mathbf{S}_{k\mathrm{y}} + \mathbf{V}_{(k-1)\mathrm{y}} \cdot t + \boldsymbol{r} \cdot \sin u_2 \cdot \sin v_2 = 0 \tag{4.5}$$

$$0.1464 \cdot \mathrm{a} \cdot u_1 + 0.5 \cdot \mathrm{a} \cdot v_1 - 0.8535 \cdot \mathrm{b} \cdot ({u_1}^2 + {v_1}^2) - (\mathbf{S}_{k\mathrm{z}} - \mathrm{L}) + \boldsymbol{r} \cdot \cos v_2 = 0 \tag{4.6}$$

The outward normal vector of the transformed convex surface ${\boldsymbol{n}_{1k(\mathrm{out})}}^{\mathbf{T}}$ can be obtained by Equation 3.25,

$${\boldsymbol{n}_{1k(\mathrm{out})}}^{\mathbf{T}} = \begin{bmatrix} (17.07 \cdot u_1 - 2.92)(10 \cdot v_1 + 14.142) - (17.07 \cdot v_1 - 10)(10 \cdot u_1 + 10) \\ (17.07 \cdot u_1 - 2.92)(2.92 \cdot v_1 + 10) - (17.07 \cdot v_1 - 10)(2.92 \cdot u_1 - 17.05) \\ (10 \cdot u_1 + 10)(2.92 \cdot v_1 + 10) - (2.92 \cdot u_1 - 17.05)(10 \cdot v_1 + 14.142) \end{bmatrix} \tag{4.7}$$

The inward normal vector of the probe sphere tip $\boldsymbol{n}_{2k(\mathrm{in})}$ can be obtained by Equation 3.29**,**

$$\boldsymbol{n}_{2k(\mathrm{in})} = \begin{bmatrix} -\mathbf{r}^{\mathbf{2}} \cdot \cos(u_2) \cdot \sin^2 v_2 \\ -\mathbf{r}^{\mathbf{2}} \cdot \sin(u_2) \cdot \sin^2 v_2 \\ -\mathbf{r}^{\mathbf{2}} \cdot \cos(v_2) \cdot \sin(v_2) \end{bmatrix} \tag{4.8}$$

Substituting Equations 4.7 and 4.8, in Equation 3.30, we get,

$${\boldsymbol{n}_{1k(\mathrm{out})}}^{\mathbf{T}}[\mathrm{x}] + \lambda \cdot \boldsymbol{r}^2 \cdot \cos u_2 \cdot \sin^2 v_2 = 0 \tag{4.9}$$

$${\boldsymbol{n}_{1k(\mathrm{out})}}^{\mathbf{T}}[\mathrm{y}] + \lambda \cdot \boldsymbol{r}^2 \cdot \sin u_2 \cdot \sin^2 v_2 = 0 \tag{4.10}$$

$${\boldsymbol{n}_{1k(\mathrm{out})}}^{\mathbf{T}}[\mathrm{z}] + \lambda \cdot \boldsymbol{r}^2 \cdot \sin v_2 \cdot \cos v_2 = 0 \tag{4.11}$$

The initial location of the spindle $\mathbf{S}_0$ can be obtained using the ${\mathbf{N}_{1k(\mathrm{out})}}^{\mathbf{T}}$, length of the stylus stem L, radius of the probe sphere *r* and initial azimuthal (u_0) and polar angles (v_0) as,

$$\mathbf{S_0} = \boldsymbol{S_1}(u_0, v_0) + r \cdot {\mathbf{N}_{1k(\mathrm{out})}}^{\mathbf{T}} + \begin{bmatrix} 0 \\ 0 \\ \mathrm{L} \end{bmatrix} \tag{4.12}$$

After the probe is fed into the part surface, the spindle will move from its initial position $\mathbf{S_0}$ to the current position $\mathbf{S}_k$, which is given by,

$$\mathbf{S}_k = \mathbf{S_0} + k \cdot \mathbf{d}_\mathrm{f} \cdot \mathbf{N}_{1k(\mathrm{in})}{}^{\mathbf{T}}, \qquad k \in [1,2,3,\ldots] \tag{4.13}$$

Equations 4.4, 4.5, 4.6 and 4.9, 4.10, 4.11 can be solved simultaneously using MATLAB by utilizing the lsqnonlin solver.

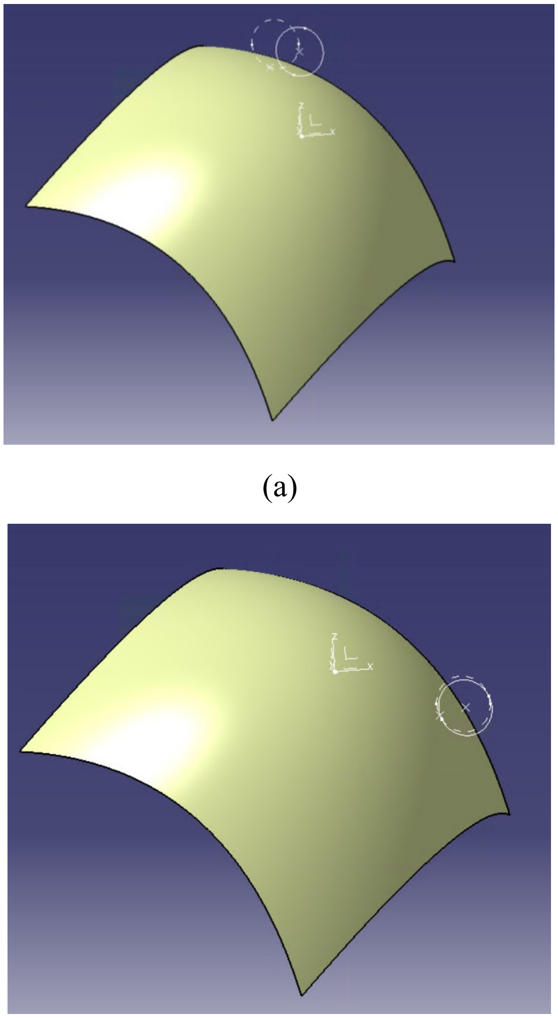

(a)

(b)

Figure 4.19: Sliding of a probe tip on convex surface at (a) u = 0.5, v = 0.5 and (b) u = 0.5, v = -0.5

Sliding of the probe tip while measuring two different points on the same surface can vary significantly as observed from above figures. For the same amount of feed, the probe sliding distance differs from point to point. From Figure 4.18 (a), the probe sliding distance is more for the same feed amount (d_f) than that in (b). Thus, the sliding effect should be considered in surface measurement. For the above two cases, the probe triggers at different positions as well. The sliding distance values (d_{sk}) for each iteration in above two cases and the sensing distance results are discussed below.

Table 4.10: d_{sk} values at two points on convex surface for 20 iterations

Iteration	**d_f (mm)**	**d_{sk} (mm) (u = 0.5, v = 0.5)**	**d_{sk} (mm) (u = 0.5, v = -0.5)**
1	0.001	0.003605	0.0012
2	0.002	0.007209	0.0024
3	0.003	0.010811	0.003599
4	0.004	0.014412	0.004799
5	0.005	**0.018011**	0.005999
6	0.006	0.021609	0.007199
7	0.007	0.025206	0.008398
8	0.008	0.028801	**0.009598**
9	0.009	0.032394	0.010798
10	0.01	0.035986	0.011997
11	0.011	0.039576	0.013197
12	0.012	0.043165	0.014397
13	0.013	0.046753	0.015596
14	0.014	0.050339	0.016796
15	0.015	0.053924	0.017995
16	0.016	0.057507	0.019195
17	0.017	0.061089	0.020394
18	0.018	0.064669	0.021594

19	0.019	0.068248	0.022794
20	0.020	0.071825	0.023993

It was observed that, for the point with parameters (0.5,0.5), the probe travel at trigger instance (d_f) was 5 microns while it was 8 microns in the other case.

4.5.2 Curved Surface Example II: Ellipsoidal Surface

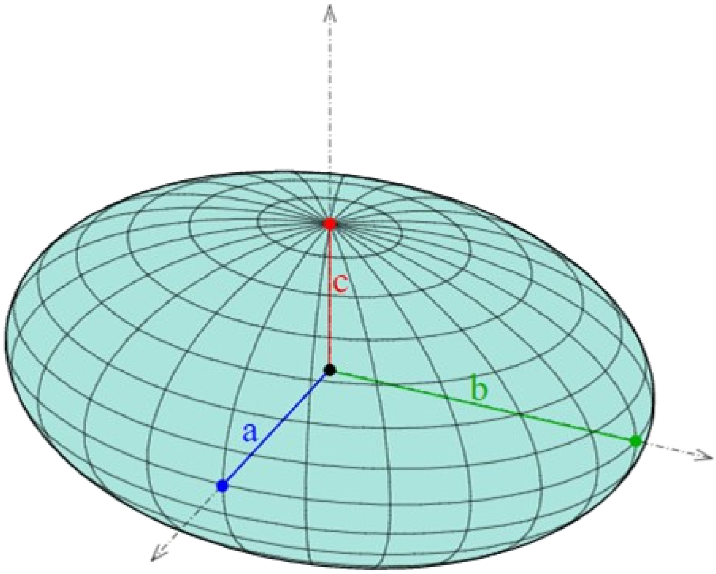

Figure 4.20: Ellipsoidal Surface

The ellipsoidal surface $\boldsymbol{S}_{\mathbf{1}}$ with its center located at origin **O** as shown in Figure 4.20 can be parametrically defined as,

$$\boldsymbol{S}_{\mathbf{1}}(u_1, v_1) = \begin{bmatrix} \mathbf{a} \cdot \cos u_1 \cdot \sin v_1 \\ \mathbf{b} \cdot \sin u_1 \cdot \sin v_1 \\ \mathbf{c} \cdot \cos v_1 \end{bmatrix}, \tag{4.14}$$

$$0 \leq u_1 \leq 2\pi$$

$$0 \leq v_1 \leq \pi.$$

where, u_1 and v_1 are the parameters of ellipsoidal surface $\boldsymbol{S_1}$.

Substituting Equation 4.14 and 3.17 in Equation 3.19, we get,

$$\mathbf{a} \cdot \cos u_1 \cdot \sin v_1 - \mathbf{S}_{k\mathrm{x}} + \mathbf{V}_{(k-1)\mathrm{x}} \cdot t + \boldsymbol{r} \cdot \cos u_2 \cdot \sin v_2 = 0 \tag{4.15}$$

$$\mathbf{b} \cdot \sin u_1 \cdot \sin v_1 - \mathbf{S}_{k\mathrm{y}} + \mathbf{V}_{(k-1)\mathrm{y}} \cdot t + \boldsymbol{r} \cdot \sin u_2 \cdot \sin v_2 = 0 \tag{4.16}$$

$$\mathbf{c} \cdot \cos v_1 - (\mathbf{S}_{k\mathrm{z}} - \mathrm{L}) + \boldsymbol{r} \cdot \cos v_2 = 0 \tag{4.17}$$

The outward normal vector of the ellipsoidal surface $\boldsymbol{n}_{1k(\mathrm{out})}$ can be obtained by the Equation 3.25,

$$\boldsymbol{n}_{1k(\mathrm{out})} = \begin{bmatrix} \mathbf{a^2} \cdot \cos(u_1) \cdot \sin^2 v_1 \\ \mathbf{b^2} \cdot \sin(u_1) \cdot \sin^2 v_1 \\ \mathbf{c^2} \cdot \cos(v_1) \cdot \sin(v_1) \end{bmatrix} \tag{4.18}$$

The inward normal vector of the probe sphere tip $\boldsymbol{n}_{2k(\mathrm{in})}$ can be obtained by the Equation 3.29**,**

$$\boldsymbol{n}_{2k(\mathrm{in})} = \begin{bmatrix} -\mathbf{r^2} \cdot \cos(u_2) \cdot \sin^2 v_2 \\ -\mathbf{r^2} \cdot \sin(u_2) \cdot \sin^2 v_2 \\ -\mathbf{r^2} \cdot \cos(v_2) \cdot \sin(v_2) \end{bmatrix} \tag{4.19}$$

Substituting Equations 4.18 and 4.19, in Equation 3.30, we get,

$$\mathbf{a}^2 \cdot \cos u_1 \cdot \sin^2 v_1 + \lambda \cdot \mathbf{r}^2 \cdot \cos u_2 \cdot \sin^2 v_2 = 0 \tag{4.20}$$

$$\mathbf{b}^2 \cdot \sin u_1 \cdot \sin^2 v_1 + \lambda \cdot \mathbf{r}^2 \cdot \sin u_2 \cdot \sin^2 v_2 = 0 \tag{4.21}$$

$$\mathbf{c}^2 \cdot \cos v_1 \cdot \sin v_1 + \lambda \cdot \mathbf{r}^2 \cdot \sin v_2 \cdot \cos v_2 = 0 \tag{4.22}$$

The initial location of the spindle $\mathbf{S}_0$ can be obtained using the $\mathbf{N}_{1k(\mathrm{out})}$, length of the stylus stem L, radius of the probe sphere **r** and initial azimuthal (u_0) and polar angles (v_0) as,

$$\mathbf{S_0} = \boldsymbol{S_1}(u_0, v_0) + \mathbf{r} \cdot \mathbf{N}_{1k(\mathrm{out})} + \begin{bmatrix} 0 \\ 0 \\ \mathrm{L} \end{bmatrix} \tag{4.23}$$

After the probe is feed into the part surface, the spindle will move from initial position $\mathbf{S_0}$ to the current position $\mathbf{S}_k$, which is given by,

$$\mathbf{S}_k = \mathbf{S_0} + k \cdot \mathbf{d}_\mathrm{f} \cdot \mathbf{N}_{1k(\mathrm{in})}, \qquad k \in [1,2,3, \dots] \tag{4.24}$$

The vector $\mathbf{v}_k$ is a component of $\boldsymbol{n}_{1k(\mathrm{out})}$ in the plane perpendicular to probe axis and can be obtained as,

$$\mathbf{v}_k = \begin{bmatrix} \mathbf{a^2} \cdot \cos(u_1) \cdot \sin^2 v_1 \\ \mathbf{b^2} \cdot \sin(u_1) \cdot \sin^2 v_1 \\ 0 \end{bmatrix} \tag{4.25}$$

Thus, the unit vector $\mathbf{V}_k$ is,

$$\mathbf{V}_k = \begin{bmatrix} \cos(u_1) \\ \sin(u_1) \\ 0 \end{bmatrix} \tag{4.26}$$

Equations 4.15, 4.16, 4.17 and 4.20, 4.21, 4.22 can be solved simultaneously using MATLAB with the lsqnonlin solver. Special note was taken to specify the initial guess point, since there are two possible outcomes,

1. The ray originating at point $\mathbf{P}_k$ and parallel to $\mathbf{V}_{k\text{-}1}$ intersects the part surface at point $\mathbf{P}_{ki}$ as shown in the Figure 4.21, point $\mathbf{P}_{ki}$ is the initial guess point.

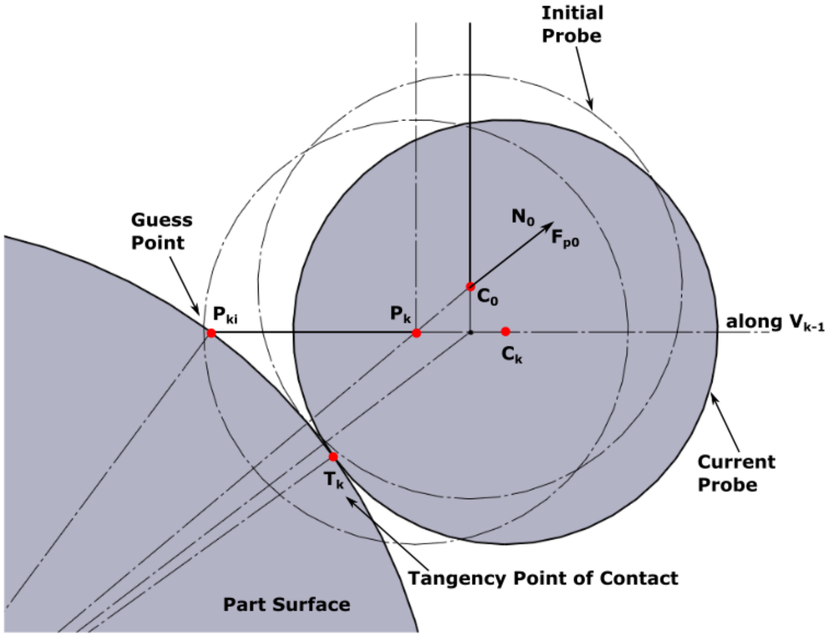

Figure 4.21: Guess point when ray intersects the part surface

2. The ray originating at point $\mathbf{P}_k$ and parallel to $\mathbf{V}_{k-1}$ does not intersect the part surface. In such cases, the point $\mathbf{P}_{kj}$ is considered as an initial guess point as shown in Figure 4.22.

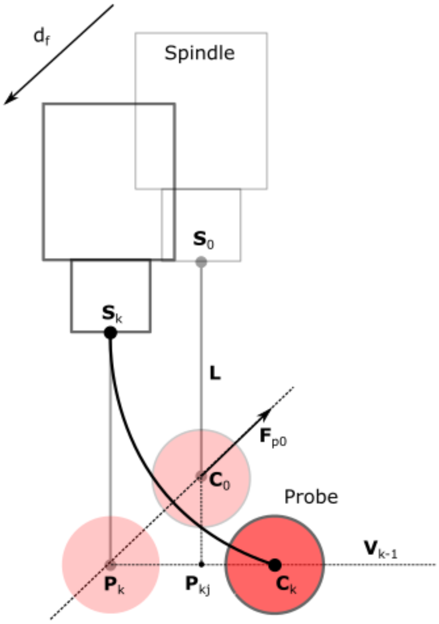

Figure 4.22: Guess point $\mathbf{P}_{kj}$ when ray does not intersect part surface

4.5.3 Effects of Surface Curvature on Sensing Distance

In this study, the effect of surface curvature on surface measurement has been established. The two surfaces, ellipsoidal and inclined surfaces have varying curvature at any given point. The target point to be measured on both surfaces is chosen such that the surface normal at this point for both the surfaces is the same. This can be done by selecting a point, preferably in the high curvature region on any one surface. The surface normal is then calculated at the selected point. By equating this surface normal to that of the other surface normal equation, we obtain the parameters of the point on the other surface. Now, since the points on both the surfaces are now known, MATLAB algorithm script can be utilized to find the values of $\mathbf{T}_k$ and d_{sk} for each subprocess. Now, the FEA method is used to determine the triggering of the probe and ultimately find the sensing distance and the spindle location at this stage to compensate for the measurement error.

4.5.4 Effects of Surface Curvature: Ellipsoidal and Inclined Surface

First, the point on the ellipsoidal surface is chosen. The parameters of the ellipsoidal surface at the chosen point are (0,40). The surface normal at this point is calculated and normalized. This normalized vector is then equated with that of inclined surface and the parameters of the point where both surface normal are equal is found. Now, since both the surface normal are known, the probe is fed along this normal direction and the sliding of the probe tip is observed for both the surfaces. Using MATLAB, the table consisting of the sliding distances for two surfaces and for 20 iterations was constructed as shown in Table 4.11. The sliding of the probe tip on the ellipsoidal surface is demonstrated using CATIA V5 as shown in the Figure 4.23 and the inclined surface is shown in the Figure 4.24.

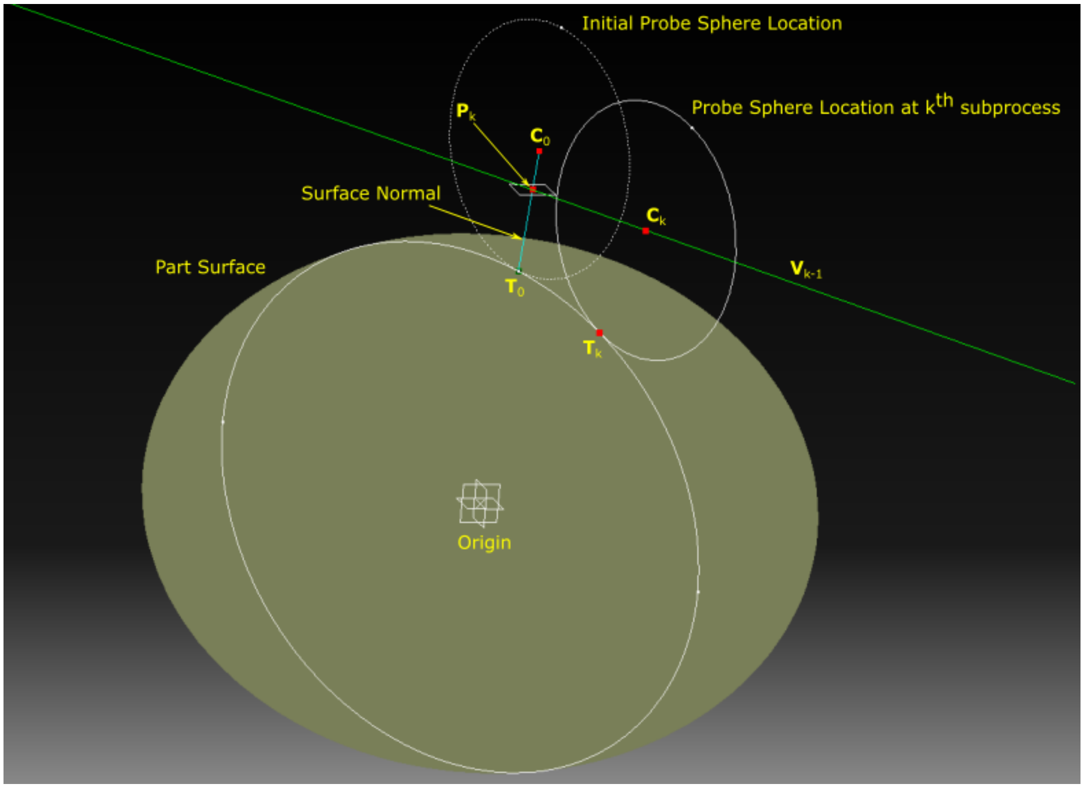

Figure 4.23: Sliding effects of probe tip on ellipsoidal surface

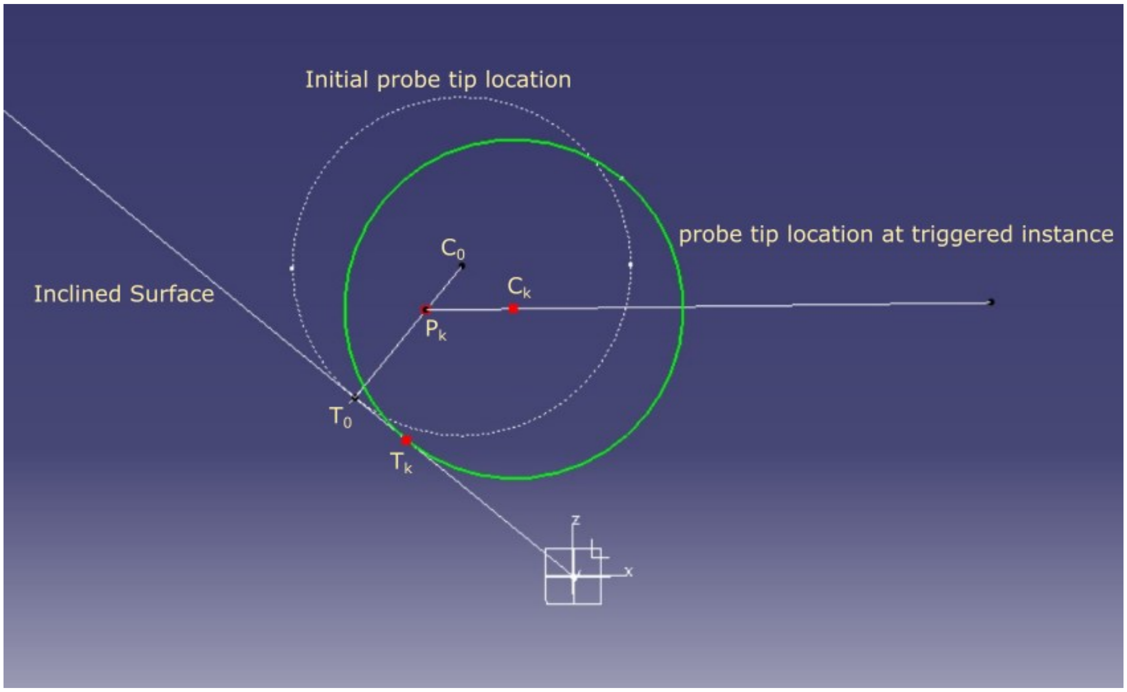

Figure 4.24: Sliding effects of probe tip on inclined surface

Table 4.11: df and ds*k* values for each iteration for both surfaces

Iteration	**d_f (mm)**	**d_{sk} (μm) (Ellipsoidal surface)**	**d_{sk} (μm) (Inclined surface)**
1	0.001	2.6732	2.000
2	0.002	4.896	3.000
3	0.003	7.117	5.000
4	0.004	9.339	6.000
5	0.005	11.560	8.000
6	0.006	13.780	9.000
7	0.007	16.000	11.000
8	0.008	18.219	12.000
9	0.009	20.437	14.000
10	0.01	22.655	16.000
11	0.011	24.872	17.000

12	0.012	27.088	19.000
13	0.013	**29.3042**	20.000
14	0.014	31.519	22.000
15	0.015	33.730	23.000
16	0.016	35.940	25.000
17	0.017	38.160	26.000
18	0.018	40.373	**28.000**
19	0.019	42.585	30.000
20	0.02	44.346	31.000

As observed from the above results, d_{sk} values in each iteration in the case of two surfaces are different. This is due to the different curvatures of the two surfaces. FEA method was utilized to find the triggering point of the probe in this normal direction. Since d_{sk} values vary for both surfaces, the probe will trigger at different locations for these surfaces. The inclined surface triggers at 18th iteration i.e., d_f at 0.018 mm, and ellipsoidal surface triggers at 13th iteration i.e., d_f at 0.013mm. Even though the probe approach direction is the same initially for both the surfaces, the effect of surface curvature affects the sensing distance. Sensing distance for polar angles from 10 to 80 degrees has been studied for both the surfaces. Figure 4.25 clearly shows the difference in the spindle travel at trigger instance for both the surfaces when probed along the same normal direction. The total spindle travel when measuring an ellipsoidal surface is less than that of an inclined surface indicating that the spindle needs to travel more to trigger the probe when measuring an inclined surface than the ellipsoidal surface when measuring in the same direction.

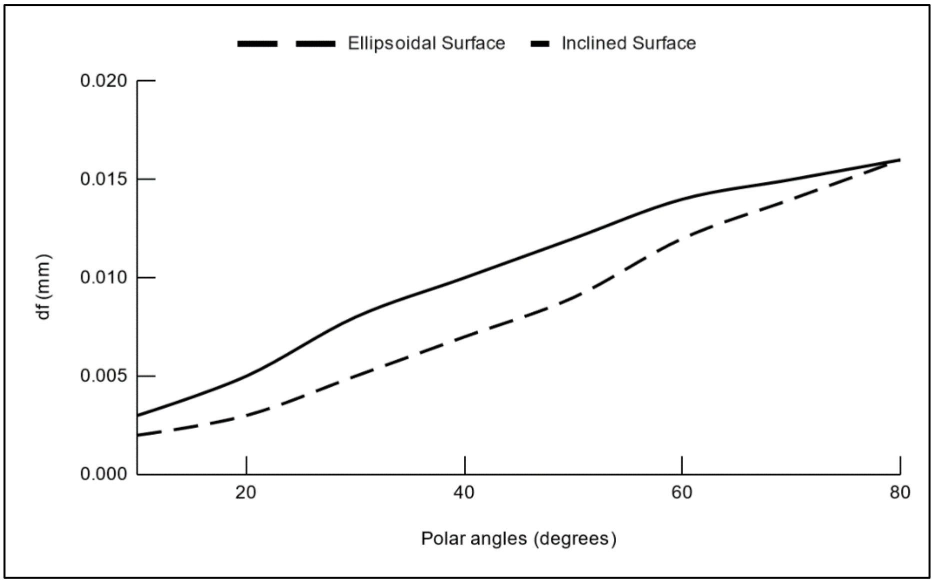

Figure 4.25: Total spindle travel (d_f) at various polar angles

4.6 Sensitivity Studies

Sensitivity studies is carried out to study the effects of varying probe parameters on the sensing distance and trigger force. The parameters length of the stylus stem, diameter of the stylus stem, material of stem and the preloaded spring force were varied. Since, the probe has symmetric structure, only 1/6th of the results needs to be analyzed. The baseline parameters model used to carry out the sensitivity study are given in Table 4.12.

Table 4.12: Baseline parameters for sensitivity studies

Parameter	Value
Preloaded spring force	5.91 N
Stylus stem length	100 mm
Stylus stem diameter	4.5 mm
Polar angle	90 degree
Azimuthal angle	0 – 60 degrees
Stylus stem material	Tungsten carbide, Stainless steel

4.6.1 Stylus Stem Length : 100 mm vs 50 mm

Figure 4.26: Stylus stem length, 50 mm (top) and 100 mm (bottom)

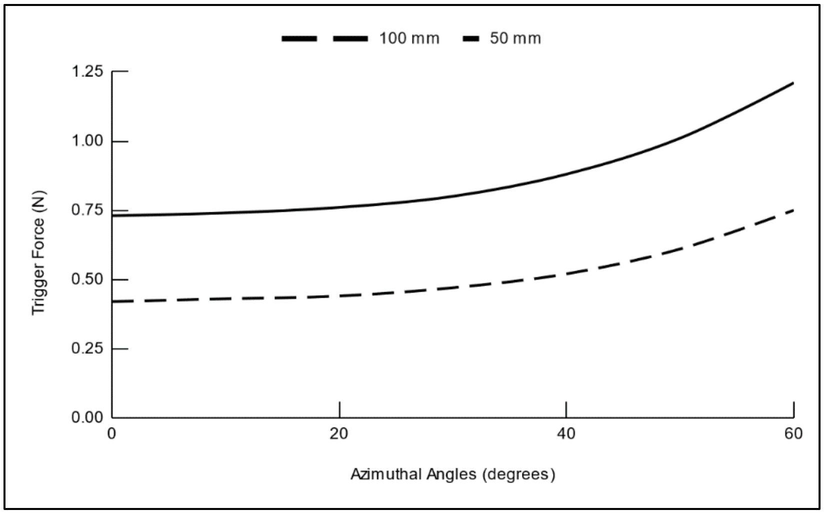

Figure 4.27: Trigger force for 100 mm and 50 mm stylus stem length

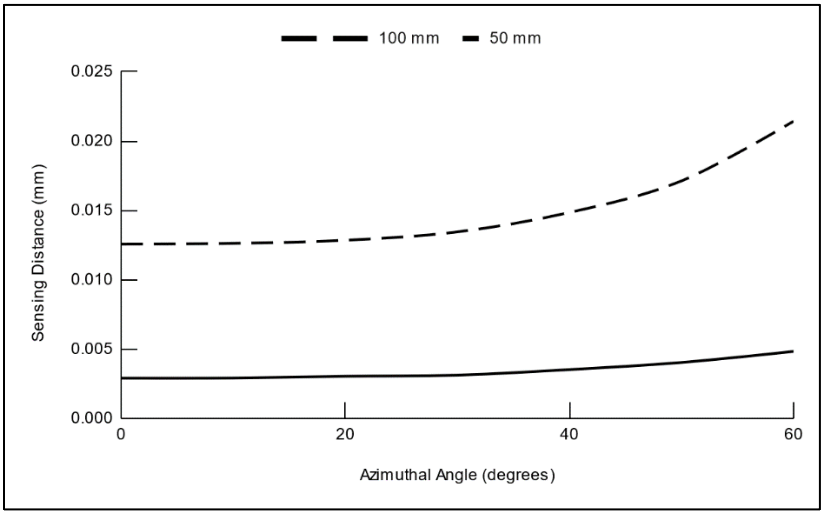

Figure 4.28: Sensing distance for 100 mm and 50 mm stylus stem length

It was observed that a longer stylus stem is triggered at a lower value of force than the shorter stem. However, since the stiffness of the stem decreases as the length increases, the longer stylus stem bends more than the shorter stem and thus is evident from Figure 4.28 that it has more sensing distance than its shorter counterpart. Although it is recommended to use the shorter stem wherever possible, some applications may require utilizing a longer stylus stem.

4.6.2 Stylus Stem Diameter : 4.5 mm vs 3.8 mm

Figure 4.29: Stylus stem diameter: 3.8 mm (top) and 4.5 mm (bottom)

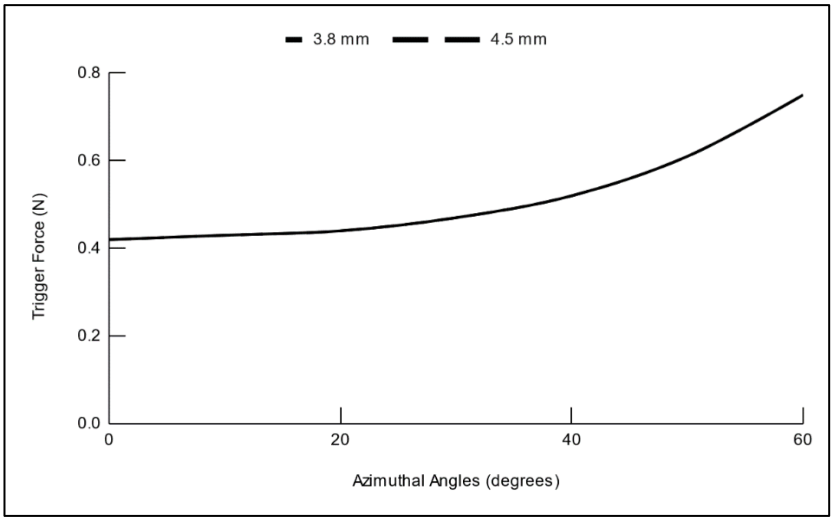

Figure 4.30: Trigger force for 4.5 mm and 3.8 mm stylus stem diameter

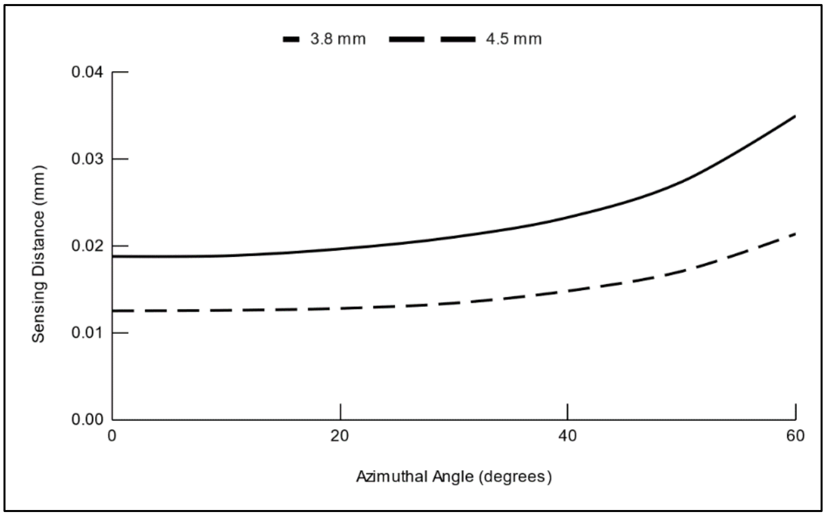

Figure 4.31: Sensing distance for 4.5 mm and 3.8 mm stylus stem diameter

The diameter of the stylus stem has no effect on the trigger force as long as other parameters are the same as evident from Figure 4.30. However, it does have an effect on the sensing distance. As the diameter decreases, the moment of inertia of the stylus stem decreases which depends on cross section, thereby increasing the bending of the stem. Thus, the sensing distance increases as the stem diameter decreases, and it is recommended to use a larger diameter stylus stem whenever possible.

4.6.3 Stylus Stem Material : Tungsten Carbide vs Ceramics

Tungsten carbide and Ceramics are among the two widely used stylus stem materials manufactured by Renishaw PLC. Trigger force and sensing distance results are discussed below.

Figure 4.32: Stylus stem materials: Tungsten carbide (top) and Ceramics (bottom)

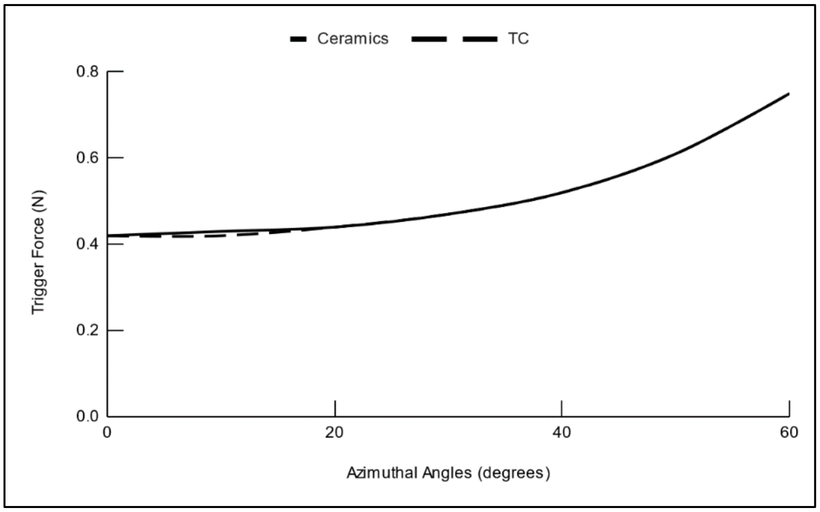

Figure 4.33: Trigger force for Tungsten carbide and Ceramics stylus stem material

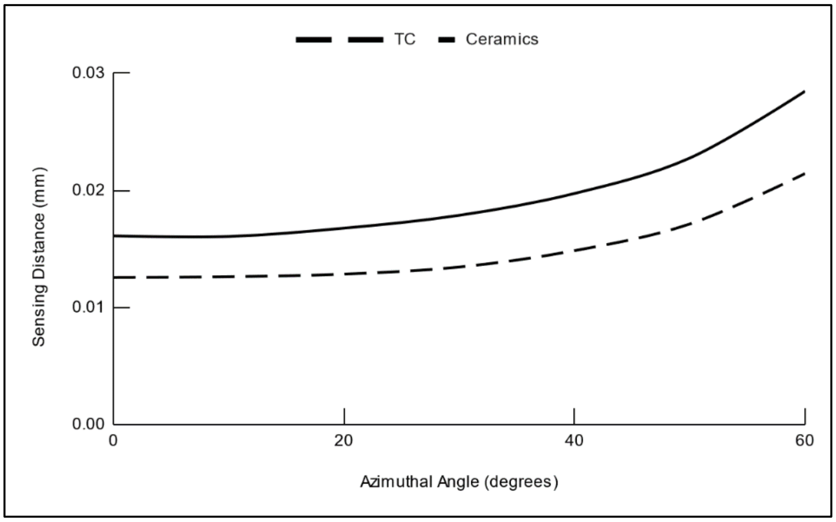

Figure 4.34: Sensing distance for Tungsten carbide and Ceramics stylus stem material

The material of the stylus stem has no effect on the trigger force. However, it does affect the sensing distance. These two materials have different young's modulus and their values are shown in the table below.

Table 4.13: Young’s Modulus for stylus stem materials

Material	**Young’s Modulus (GPa)**
Tungsten Carbide	686
Ceramics	413

Higher the young’s modulus, higher its stiffness and lower its tendency to bend. It can be seen from Figure 4.34 that, the stylus stem made of ceramics bends more and thus has a higher sensing distance than the stem made of tungsten carbide.

4.6.4 Preloaded Spring Force: 5.91 N and 4 N

The Renishaw OMP40-2 probe has a default preloaded spring force of 5.91 N. Also, since most of the experiments conducted with this probe have this default spring force, it was used as a baseline parameter in all the surface measurement results. However, in order to conduct the sensitivity study to evaluate the effect of this spring force on trigger force and sensing distance, 4 N preloaded spring force was applied.

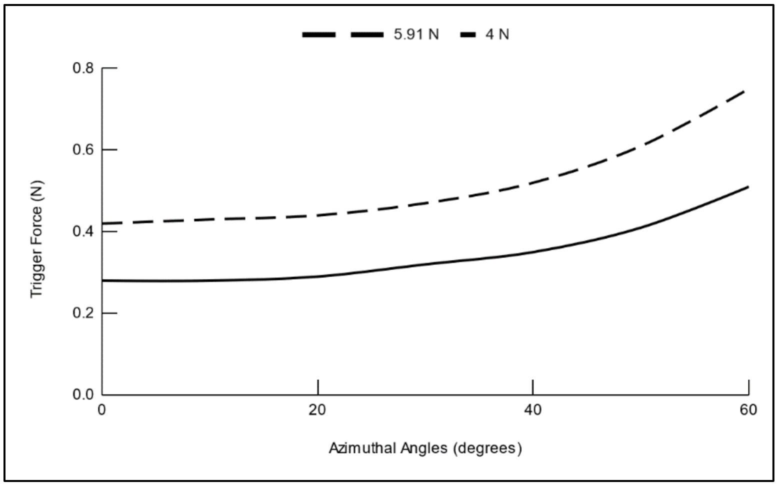

Figure 4.35: Trigger Force for 5.91 N and 4 N preloaded spring force

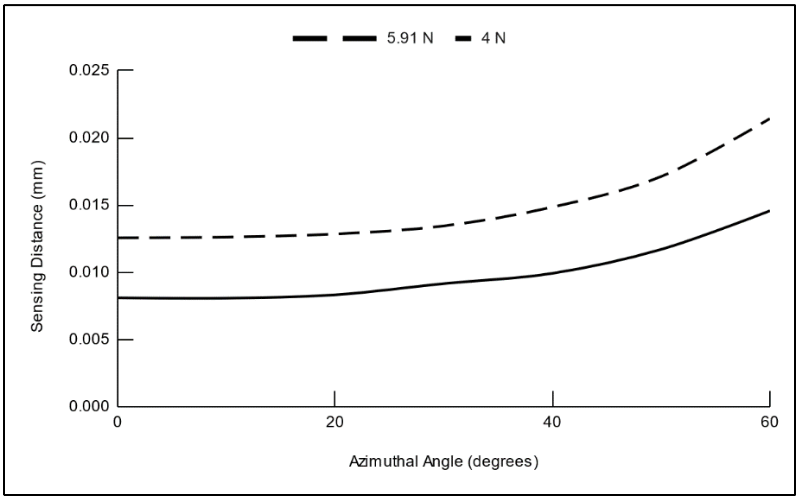

Figure 4.36: Sensing distance for 5.91 N and 4 N preloaded spring force

As the preloaded spring force decreases, the probing force required to trigger the probe reduces as well based on the mechanics of material. Reduction in the trigger force causes the sensing distance to decrease as shown in Figure 4.36. Although it may be assumed that reducing the preloaded spring force is better, this may indeed cause the touch probe to falsely trigger due to external factors such as vibration. This may have the worst effect on the measurement results. It is therefore recommended to use the factory default preloaded spring force.

Chapter 5: Conclusion and Future Work

5.1 Conclusion

In this thesis, the sensing distance modeling of the kinematic touch trigger probe in case of the vertical surface, inclined surface, and curved surfaces have been investigated. The sensing distance error is a major source of systematic error in kinematic touch trigger probes and thus needs to be calibrated before utilizing it in the measurement process. Therefore, it is necessary to predict the sensing distance accurately before calibrating the probe. As described in Chapter 2, the kinematic touch trigger probe based on Renishaw's OMP40-2 Probe was modeled and was set as a basis for predicting the sensing distance using FEA techniques. In chapter 3, the mathematical model was developed to find the sliding distance in each iteration in the case of vertical surface, inclined surface, and curved surface. FEA method is implemented to determine the trigger condition of the probe and find the corresponding sensing distance. In chapter 4, the results of several surfaces were discussed. It was observed that the existing method overestimates the sensing distance for higher polar angles and underestimates the sensing distance at lower polar angles. This is due to the oversimplification of the model and assumptions made by the authors. Two examples of the curved surface were studied. It is evident from convex surface results that the sliding of the probe at different points on the same part surface varies significantly and thus this sliding effect cannot be ignored.

The sliding of the probe tip also depends on the surface curvature of the part surface. As seen from the results of the spherical and inclined surface, the probe slides more in case of the inclined surface when it is fed along the same normal direction. The percentage difference between the sensing distance in these two cases was around 27.7%. Finally, sensitivity studies were carried out signifying the importance of the probe parameters on the surface measurement process. Various probe parameters were varied and their corresponding sensing distance and trigger force were compared and discussed. Finally, recommendation was also made to use the suitable probe parameters unless the application requires otherwise.

5.2 Future Work

There are a number of suggestions in order to broaden this research work. The following topics can be studied:

In order to obtain the sensing distance data for a particular set of measurement parameters and the part surface, the process can be automated by linking MATLAB results with the ANSYS FEA package.

In addition to the proposed novel mathematical model for surface measurement, certain curved surfaces can be machined, and experiments can be performed using a physical kinematic touch trigger probe.

Similar to the golden section search algorithm utilized for the vertical and inclined surface measurement, a similar form of search algorithm needs to be employed to speed up the FEA simulation process in case of the curved surface measurement in which the direction of the probing force changes as the probe tip slides on the part surface.

References

[1] "Quality control in the manufacture of metal parts," *Metal Cutting Corporation*. https://metalcutting.com/knowledge-center/quality-control-in-the-manufacture-of-metal-parts/ (accessed Jan. 21, 2021).

[2] "Deciding between a non-contact metrology platform and a traditional CMM," *DWFritz Automation*, Jun. 30, 2019. https://www.dwfritz.com/2019/06/30/deciding-between-a-non-contact-metrology-platform-and-a-traditional-cmm/ (accessed Jan. 21, 2021).

[3] "Probes." https://www.qualitydigest.com/jan97/probes (accessed Jan. 21, 2021).

[4] "Probing systems for CNC machine tools." Renishaw plc.

[5] "TE411_innovations_in_touch-trigger_probe_sensor_technology.pdf."

[6] Renishaw. plc, "Renishaw: OMP40-2," *Renishaw*. http://www.renishaw.com/en/omp40-2-optical-transmission-probe--7992 (accessed Jan. 21, 2021).

[7] Y.-L. Shen and X. Zhang, "Pretravel compensation for vertically oriented touch-trigger probes with straight styli," *Int. J. Mach. Tools Manuf.*, vol. 37, no. 3, pp. 249–262, Mar. 1997, Doi: 10.1016/S0890-6955(96)00060-0.

[8] R. P. Johnson, Q. Yang, and C. Butler, "Dynamic error characteristics of touch trigger probes fitted to Coordinate Measuring Machines," *IEEE Trans. Instrum. Meas.*, vol. 47, no. 5, p. 5, 1998.

[9] A. Wozniak, M. Byszewski, and M. Jankowski, "Setup for triggering force testing of touch probes for CNC machine tools and CMMs," *Meas. Sci. Rev.*, vol. 13, no. 1, Jan. 2013, Doi: 10.2478/msr-2013-0004.

[10] Z. Bohan, G. Feng, and L. Yan, “Study on pre-travel behaviour of touch trigger probe under actual measuring conditions,” *Procedia CIRP*, vol. 27, pp. 53–58, 2015, Doi: 10.1016/j.procir.2015.04.043.

[11] X. M. Qian, W. H. Ye, and X. M. Chen, “On-Machine Measurement for touch trigger probes and its error compensation,” *Key Eng. Mater.*, vol. 375–376, pp. 558–563, Mar. 2008, Doi: 10.4028/www.scientific.net/KEM.375-376.558.

[12] C. Achelker, N. S. Rao, R. Rajendra, and A. Krishaniah, “Performance evaluation of machine tool probe for in-process inspection of 2D and 3D geometries,” *Procedia Technol.*, vol. 14, pp. 244–251, 2014, Doi: 10.1016/j.protcy.2014.08.032.

[13] J. R. RenéMayer, A. Ghazzar, and O. Rossy, “3D characterisation, modeling and compensation of the pre-travel of a kinematic touch trigger probe,” *Measurement*, vol. 19, no. 2, pp. 83–94, Oct. 1996, Doi: 10.1016/S0263-2241(96)00068-1.

[14] P. A. Cauchick-Miguel and T. G. King, “Factors which influence CMM touch trigger probe performance,” *Int. J. Mach. Tools Manuf.*, vol. 38, no. 4, pp. 363–374, Mar. 1998, Doi: 10.1016/S0890-6955(97)00054-0.

[15] C. Butler, “An investigation into the performance of probes on coordinate measuring machines,” *Ind. Metrol.*, vol. 2, no. 1, pp. 59–70, Dec. 1991, Doi: 10.1016/0921-5956(91)80025-B.

[16] “What Is FEM & FEA Explained | Finite Element Method,” *SimScale*, Oct. 24, 2016. https://www.simscale.com/blog/2016/10/what-is-finite-element-method/ (accessed Jan. 23, 2021).

[17] Ozgün, “Contact types and behaviours in Ansys,” *Mechead.com*, Jul. 28, 2018. http://www.mechead.com/contact-types-and-behaviours-in-ansys/ (accessed Jan. 23, 2021).

[18] "A Simple adjustment to fix a contact convergence problem in Ansys Mechanical," *PADT, Inc. - The Blog*, Jun. 04, 2020. https://www.padtinc.com/blog/a-simple-adjustment-to-fix-a-contact-convergence-problem-in-ansys-mechanical/ (accessed Jan. 25, 2021).

[19] "ANSYS Contact Technology Guide," p. 105.

[20] D. Madier, Practical Finite Element Analysis for Mechanical Engineers, 2020, p. 129.

[21] Y. Shen and M. E. Springer, "A Robust pretravel model for touch trigger probes in Coordinate metrology," *J. Manuf. Sci. Eng.*, vol. 120, no. 3, p. 532, 1998, Doi: 10.1115/1.2830156.

[22] ANSYS, Inc., "ANSYS Workbench documentation,", August 2005, p. 972.

[23] Caendkoelsch, "Direct vs. iterative solvers in FEM," *caendkölsch*, Nov. 29, 2018. https://caendkoelsch.wordpress.com/2018/11/29/direct-vs-iterative-solvers-in-fem/ (accessed Jan. 25, 2021).

[24] M. Jankowski and A. Wozniak, "Testing of the delay time of wireless communication of CNC machine tool's probes and controller," *Metrol Meas Syst*, vol. 25, no. 2, p. 10, 2018.

[25] M. Jankowski and A. Woźniak, "Master artifacts for testing the performance of probes for CNC machine tools," in *Advanced Mechatronics Solutions*, vol. 393, R. Jabłoński and T. Brezina, Eds. Cham: Springer International Publishing, 2016, pp. 323–328. Doi: 10.1007/978-3-319-23923-1_49.

[26] "Golden section search." http://fourier.eng.hmc.edu/e176/lectures/ch3/node3 (accessed Jan. 26, 2021).